From Self-Assembly To Communications Via Machine Washable Fibers

by

Michael Rein

B.Sc., Materials Science and Engineering; B.A., Physics
Technion - Israel Institute of Science, 2007
M.Sc., Chemistry
Weizmann Institute of Science, 2010

Submitted to the Department of Materials Science and Engineering
in partial fulfillment of the requirements for the degree of

Doctor of Philosophy in Materials Science and Engineering

at the

MASSACHUSETTS INSTITUTE OF TECHNOLOGY

February 2018

Author ..... Signature redacted
Department of Materials Science and Engineering
December 31, 2017

Certified by .. Signature redacted .....
Yoel Fink
Professor of Materials Science
Professor of Electrical Engineering and Computer Science
Thesis Supervisor

Accepted by ....
Donald R. Sadoway
Chairman, Department Committee on Graduate Students

From Self-Assembly To Communications Via Machine Washable Fibers

by

Michael Rein

Submitted to the Department of Materials Science and Engineering
on December 31, 2017, in partial fulfillment of the
requirements for the degree of
Doctor of Philosophy in Materials Science and Engineering

Abstract

Fibers and fabrics are among the earliest forms of human expression, and yet they have not progressed much from a functional standpoint over the course of history. Recently, a new family of fibers composed of conductors, semiconductors and insulators has emerged. These fibers can achieve device attributes, yet are fabricated using scalable preform-based fiber-processing methods, yielding kilometers of functional fiber devices. Co-draw of different materials is possible for numerous material combinations and sizes, where one of the limiting factors to a continuous feature size in fibers is the Rayleigh-Plateau capillary instability.
In my thesis I have shown that it is possible to utilize this adverse fluid instability phenomenon to fabricate uniformly sized and uniformly structured spherical particles internal to the fibers. Judicial choice of the materials and control over the kinetics of this process allowed to integrate the spherical particles into an active fiber device. We have introduced additional ability to control the structure of the fiber by making this process selective, forming high density array of self-assembled spherical photodetectors, connected to continuous electrodes. This fiber structure shows enhanced photoconductivity and sensitivity to wavelength variation, due to spherical geometry of the photoresistive domains. Additionally, an alternative strategy for integrating active devices into fibers was demonstrated. Rather than addressing all the challenges of thermal drawing, we have developed a method to directly integrate commercial functional devices (light emitting diodes, photodetectors etc.) into fibers through thermal drawing. We package these devices internal to the fibers in high density and integrate them with conductive buses, during the thermal draw. This approach enables to combine the benefits of several technologies - high-efficiency devices integrated into kilometer long fibers, which could be weaved into highly functional fabrics. Endowing fibers with active devices will potentially establish a new generation of multifunctional fibers, with highly desired electronic properties. For example, flexible and resilient light emitting fibers could be integrated into textiles to enable covert, optical signal transmission from the soldier uniform to the external world, or high bandwidth photodetectors could be embedded into garments to allow high

volume information reception via LiFi (WiFi through light).

Thesis Supervisor: Yoel Fink
Title: Professor of Materials Science
Professor of Electrical Engineering and Computer Science

Acknowledgments

Science and engineering were always a big part of my life. From making experiments with sugar and salt in the kitchen of my childhood home in Israel, when my parents were away, to mixing carbon particles or light emitting devices with polymers, one common thread is distinguished. This thread is the catalysis to these experiences - the great teachers and mentors that influenced me throughout my life. I would like to thank my high school teachers and especially Yevgeni Lilevman, who challenged and simultaneously encouraged my love to physics. I was blessed to be educated by world class teachers in the Technion, which introduced me to the field of materials science and encouraged me to pursue a career in this field. I am especially indebted to Dr. Orna Breuer that provided enormous support and mentoring during my army service at Rafael. I also would like to thank Prof. Daniel Hanoch Wagner that has supported me throughout my master studies and provided a great amount of advice and guidance in research and in my academic endeavors.

I was blessed to be advised, mentored and guided by Prof. Yoel Fink. Thank you for sharing with me your inspiration and enthusiasm for research in the field of multimaterial fibers and fabrics. I am indebted for Yoel's critical thinking, challenging, yet invigorating, ideas and for providing tremendous flexibility and opportunities throughout my PhD. I am very grateful for having such a great asset in my professional path. I am also extremely grateful for the advice and support I have received from the professors on my PhD committee - Prof. Eugene Fitzgerald, Prof. Polina Anikeeva and Prof. John Joannopoulos. Thank you for your tremendous help with my research and publications, you were always there for me, available to help.

I was very fortunate to meet amazing people at MIT and was excited to work and collaborate with the great men and women in my group. Thank you for teaching me new things, helping me troubleshoot all the equipment in the lab, brainstorming and providing feedback. I won't make it without all your help and discussions. I am deeply grateful to Dr. Etgar Levy for providing invaluable scientific insights in critical times through my journey here. Dr. Alexander Stolyarov, you are an inspiration and

a role model to me. I would like to thank Dr. Lei Wei for providing guidance in the beginning of my journey here at MIT, to Dr. Chong Hou, Dr. Guillaume Lestoquoy, Dr. Benjamin Grena, Dr. Xiaoting Jia, Dr. Alexander Gumennik, Juliette Alain, Valentine Farvod, Rodger Yuan, Gabriel Loke, Dr. JungTae Lee, Dr. Tural Khudiev, Tara Sarathi and Jeff Clayton for all your help in the lab, and just for being there to talk with me about personal and professional life. I would like to also thank Dr. Polina Pinkhasova Swift for helping me cope with my occasional PhD blues. Additional source of inspiration to me are the great people I met in AFFOA. Towards the end of my studies here, you made my day, every day. Dr. Jason Cox and Chhea Chhav, you made my work so much better, and thank you for providing such a great motivation and joy. Last but not least, I would like to thank Tina Gilman, for her endless support and help with anything I needed.

I would also like to thank all the awesome people I have met here in Boston, and friends that I left back in Israel. Special gratitude reserved to future Dr. Gal Shulkind, Dr. Johanna Karouby, Dr. Anna Tarakanova, Eduardo Sverdlin, Iddo Haklai, Tammy Cohn, Shulamit Livshin and many more, who helped me distract from the MIT intensity.

I am infinitely indebted to my family - my parents and my brother Benny. I won't be able to get to this point without your unquestionable love, support and encouragement. And finally, a huge kudos and gratitude to the person that made it through the tirade of my complaints, my love and husband Eran. Thank you for making this journey come true, for supporting me and making me laugh. I feel blessed to be surrounded by such great people and excited for what lies ahead.

Contents

THIS PAGE INTENTIONALLY LEFT BLANK

List of Figures

THIS PAGE INTENTIONALLY LEFT BLANK

List of Tables

THIS PAGE INTENTIONALLY LEFT BLANK

Chapter 1

Introduction

My thesis will focus on advances involving multimaterial and multifunctional fibers. To understand these, an introduction to fibers and to the process of thermal drawing of fibers is necessary.

1.1 Fibers and fabrics

Fibers and textiles are one of the most basic implementation of human technology since the dawn of our civilization. The discovery of dyed flax fibers in a cave in the country of Georgia in the Near East dated to 34,000 BCE suggests textile-like materials were made even in prehistoric times [1]. Other archaeological findings reveal that fibers and clothes were used throughout the world and by different cultures, from the people of Mesopotamia to the Incas in Peru [2]. Textiles are traditionally used for clothing. In the household domain, these are used for carpeting, upholstered furnishings, window shades, in art, and for both use cases, cosmetic and heat insulating properties are usually important. In other domains fibers and textiles are used for liquid filtration, reinforcement of composite materials and more, where mechanical or chemical properties of the materials become important. Although textile manufacturing techniques evolved considerably with time, fibers were used for similar purposes for many years. Only recently, considerable advances were made to introduce novel fibers to common use. The first artificial, semi-synthetic fibers were invented in 1894

by Charles Frederick Cross, and his collaborators Edward John Bevan and Clayton Beadle. These fibers were named viscose or Rayon [3]. The first fully synthetic fibers were developed in the 1930s, by DuPont, and were given a brand name of Nylon [4]. This invention transformed the textile industry - these fibers replaced some of the conventional fibers such as silk, in consumer and military products, from stockings to parachutes. Polyester fibers were invented in 1941, also known as Dacron, and used extensively in the textile industry [5]. The field of synthetic fibers continued to flourish in the late 1950 to the 1970s, with the discovery of Kevlar, by Stephanie Kwolek, working in DuPont corporation [6], which is now used in numerous applications such as ballistic and cut resistance to high performance boating. The potential of high performance carbon fibers was realized in 1958 in a process developed by Roger Bacon at the Parma Technical Center in the US, which based his technology on Rayon precursors, while Akio Shindo of the Government Industrial Research Institute in Osaka, Japan, made the first fibers based on polyacrylonitrile precursors [7], which are used in the aerospace and sport industries. Ultrahigh molecular weight polyethylene fibers were developed in the late 1970s by the Dutch chemical company DSM, and are widely used in ballistic protection and medical applications [8]. These fibers allowed many manufacturers to deliver fabrics with enhanced mechanical strength and elasticity, as well as desirable aesthetic appearance and resistance to insect infestations. In spite of these advances, even today, these fibers have stayed mainly passive materials. This feature stems from the non-complex microstructure and composition of the fibers. Since these fibers are made from a single material and have a simple structure, the properties of the fibers stem from the intrinsic properties of the constituent material. To endow fibers with more advanced or active properties more than one material has to be embedded into a single fiber, in a well controlled structure. Rapid development of such composite fibers occurred in a different domain during the 1950s - for long distance optical light transmission. The first, core - clad optical fiber was demonstrated by Lawrence Curtiss in 1956, via the thermal draw process. The first working fiber-optical data transmission system was demonstrated by German physicist Manfred Borner at Telefunken Research Labs in Ulm in 1965

and Charles K. Kao and George A. Hockham of the British company Standard Telephones and Cables were the first, in 1965, to promote the idea that the attenuation in optical fibers could be reduced below 20 decibels per kilometer, making fibers a practical communication medium [9]. They have perfected the use of high purity silica, for which they won the Nobel Prize in Physics in 2009. The use of optical fibers has increased exponentially with time, as the amount of information transferred has risen considerably. This enabling technology of thermal fiber drawing has satisfied the world's communication needs, and is currently the leading medium for long distance information transfer. Recently, more complex optical fibers were produced using a similar method - micro-structured fibers, also known as photonic crystal fibers, which comprise a periodic array of microscopic air holes in a silica or polymer matrix [10]. This microstructure allows to control and guide light in ways not obtainable using conventional step-index fibers, and these fibers have been used for high-power laser transmission and supercontinuum light generation.

Our group has been perfecting and further developing the thermal drawing technique, while taking a completely different approach for introducing new functionality to thermally drawn fibers. This is done by introducing materials that are not traditionally thermally drawn, and arranged in unique fiber architectures. This approach enabled new fiber functionality both in the optical transmission domain and in others, including photodetection, emission and reception of sound waves or energy storage [11]. Producing fibers with the thermal draw technique will potentially allow to deliver highly sought after capabilities in the textile and wearable domains. Delivering active performance within every single fiber or filament, will potentially enable active textiles and garments.

1.2 Thermal fiber draw

The process of thermal draw consists of two main steps - preform preparation and fiber draw.

1.2.1 The preform

We begin from preparing a macroscopic structure, also known as *preform*. The preform is a macroscopic structure of the eventual fiber we would like to obtain. The preform could have any desired external shape (usually cylindrical or rectangular), and is much larger than the fiber in the cross section, and shorter in length. The outermost material, also called the preform or fiber *cladding* is usually made of an amorphous material, such as silica, silicate glass, or thermoplastic polymer. The cladding material sets the temperature at which the materials flow at the drawing process. Since the cladding is the major material in the fiber structure, it will dominate the flow regime, and set the temperature at which the fiber could be drawn. Amorphous material ensures that the viscosity will not change abruptly during the heating in the draw furnace, which will allow the user to stabilize the flow of the materials, a.k.a the drawing process. The cladding will also define which other materials could be co-drawn with the cladding material. These materials are assembled into a precise geometry in polymeric - clad preforms using various machining techniques such as milling or lathing, or by rolling thin films into a cylindrical structure. Some materials could be evaporated on films and these rolled into the preform [11, 12]. The materials are then consolidated into a solid preform by application of heat in a hydraulic press or in a heated vacuum furnace, to remove trapped air and fuse all layers. For silica clad preforms it is impossible to use mechanical material processing techniques such as milling or lathing since the silica or silicate glasses are extremely brittle. In this case, the multimaterial preforms are assembled from arrangment of tubes. Small tubes are inserted into a larger one, which is the outer cladding of the preform. Various materials (i.e Si, Ge, Cu) in solid or powder form factor are placed inside the smaller tubes. In this way a multi-core preform is formed. The preform is then sealed in a vacuum, to remove any air or moisture present internal to the preform. Silica brittleness induces a constraint on the processing tools, which limits the possible fiber architectures [13, 14]. 3D printing of preforms is an emerging technique to produce multimaterial preforms with high complexity both with polymeric or silica

cladding [15, 16].

1.2.2 Draw process

Once the preform is ready to be drawn, it is placed in a vertical draw furnace and heated. Figure 1-1 illustrates the draw process. The preform is placed in a vertical draw furnace. The furnace is heated to an elevated temperature. A complex thermal profile is sometimes established to facilitate with the fiber draw, by having several heating zones. In our lab, three zone furnace is used to draw polymeric clad fibers, and just one zone is used to draw silica fibers. The preform is lowered in the furnace with a speed of v_{feed}. The hot zone of the furnace heats the preform and at this region, the materials start to flow. A neck forms, at which the cross section of the preform grows smaller in size, while the length grows into a fiber. The capstan pulls on the fiber, with a speed of v_{draw}. The fiber is then collected by a spool. From the principle of conservation of mass or volume it is possible to derive a measure of the scale down from preform to fiber, which is also called the draw down ratio - β. The draw down ratio could be related to the ratio of the feed and draw speeds and the dimensions of the fiber and preform cross section, as shown by equation 1.1. $d_{preform}$ and d_{fiber} are the preform diameter or a characteristic dimension of the cross section of the preform, and the diameter of the fiber, respectively. The length of the fiber is also related to the draw down ratio, as shown by equation 1.2. Here $L_{preform}$ is the section length of the preform which is transformed to a fiber of length L_{fiber}. The parameters that are controlled during the draw process are the feed and draw speeds and the temperature of the furnace. Some fiber parameters could be measured during the fiber draw process - tension of the fiber and the dimensions of the fiber. These measurements could be used to alter or tune the draw parameters.

$$\beta = \frac{d_{preform}}{d_{fiber}} = \sqrt{\frac{v_{draw}}{v_{feed}}} \tag{1.1}$$

$$L_{fiber} = \beta^2 \cdot L_{preform} \tag{1.2}$$

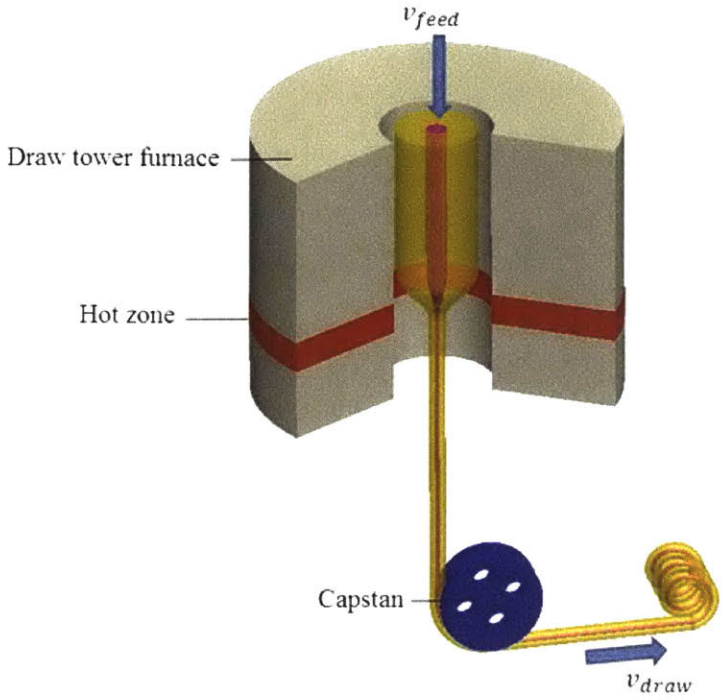

Figure 1-1: **Illustration of the fiber draw process**. The preform is placed in the vertical draw furnace and is lowered in the furnace with a speed of v_{feed}. The fiber / preform clad is represented by yellow color, and the fiber / preform core is red. The hot zone of the furnace denoted by red section, heats the preform and at this region, the materials start to flow. A neck forms, at which the cross section of the preform grows smaller in size, while the length grows into a fiber. The capstan pulls on the fiber, with a speed of v_{draw}. The fiber is then collected by a spool

1.3 Current state of art - multimaterial fibers

Perfecting the fiber draw technique has enabled new fiber functionality. Combining materials with disparate optical properties, for example a low refractive index thermoplastic with a high refractive index chalcogenide glass, has enabled the creation of photonic bandgap fibers which are omnidirectional waveguiding mirrors that are able to guide light of any desired wavelength [17, 18]. Some work of our group has demon-

strated the strengths of the fiber draw technique - ability to incorporate multiple materials into fibers, and the scalable production of fiber devices with submicron features extending kilometers in length. Incorporating materials with disparate electrical properties such as metals, amorphous semiconductors, and insulators allowed to realize electronic and optoelectronic functionalities in fibers - achieving photodetection and thermal detection [19, 20]. The set of fiber capabilities was further developed, producing fibers with piezoelectric materials that are able to emit and record sounds [21, 22]. Electronic devices were formed in fibers by building field effect domains made of glassy chalcogenide materials [23], or by draw of conventional semiconducting materials such as Si and Ge [14, 24, 25]. By introducing fluids in fibers, further functionality is made possible, such as radially-emitting fiber lasers [26], laser modulators based on liquid crystals [12] to energy storage fiber devices, which are currently developed in our group. Not just the internal structure of the fiber could be engineered, but the external surface could be designed as well, as shown in [27], where optical and superhydrophobic phenomena come into play. Thermally drawn fibers could be used in the bio-engineering domain, to interact with cells, and specifically with neurons [28]. The thermal draw of fibers technique has its limitations. A few physical principles limit the materials that could be drawn together and set a limit to the minimal achievable feature size. These limitation will be discussed in the next section.

1.4 Thermal draw limitations

The fiber thermal draw method puts some constraints on the materials that could be drawn together.

1. The first constraint is placed on the materials selection to be incorporated in fibers. As already mentioned previously, the outer fiber cladding is usually limited to glassy or amorphous materials that are able to flow when heated to a temperature above its glass transition point. Until now, silica, silicate glasses, and thermoplastic polymers, such as polycarbonate, polysulfone, polyetherim-

ide, acrylics and cyclic olefin copolymers were successfully drawn as cladding materials. The materials that could be codrawn with the cladding have to be selected according to the following guiding principles:

(a) The materials have to stay stable and not decompose, evaporate or degas at the draw temperature.

(b) The materials composing the preform have to co-flow at the draw temperature. This means that all the materials need to be viscous, and as a rule of thumb, the viscosity of the cladding should be in the range of $10^3 - 10^7$ Pa $\cdot$ sec. The viscosity of the cladding cannot decrease to very low values, since it should be the load bearing component, to ensure continuity of the fiber. Inner fiber components can be amorphous or crystalline. Any crystalline polymers, metals or semiconductors, have to be in liquid state, with melting temperature below the draw temperature. If the inner materials are amorphous, their glass transition temperature (T_g) has to be lower of the cladding material. A good review of this constraint and guide to material selection is given in [29].

(c) The materials have to be compatible with each other, both in liquid and solid states. The adhesion between components and thermal expansion of the materials have to be taken into account when selecting materials for draw. To establish and maintain contact between the materials in the fiber, these features have to be addressed. For example, polyethylene will not have good adhesion to other fiber components. Moreover, since the fibers are made at elevated temperatures, mismatch in thermal expansion coefficients between the materials might cause delaminations between the fiber components. Elevated temperatures also can lead to undesired consequences - reaction, diffusion and mixing between fiber components. These phenomena become dominant as the temperature increases, and may destroy chemically distinct interfaces in silica clad fibers.

2. Fibers are intrinsically transversially symmetric entities. This means that the

structure of the fiber will not change as we move along the fiber length or axis. The fiber structure will have the same cross section, similar to the structure in the preform. This fabrication limitation has direct consequences on the fiber functionality. It is a challenge to obtain a fiber that will have abrupt structural variations in the axial direction.

3. Another limitation imposed on features that could be achieved in fibers is the presence of fluid capillary instabilities. Fibers in the draw furnace are basically long liquid cylinders, and these are not thermodynamically stable features, as was experimentally discovered for water jets, more than 100 years ago [30, 31, 32]. This phenomenon places a constraint on the smallest achievable continuous feature size in the fiber. As the features decrease in size, they will tend to disintegrate into discontinuous domains, changing the fiber geometry and eventually the functionality. This phenomenon places a physical limit on minimal feature size in the fiber, or the fiber size itself, produced by thermal draw.

1.5 Beyond thermal draw limitations

Our and other groups have recently focused their efforts on finding ways to circumvent the limitations mentioned in the previous section, or even harness them for some beneficial purpose. To overcome the material limitation problem, several approaches were developed. First, composite materials were drawn into fibers. These materials contain particles with various sizes in the range of $100nm - 10\mu m$. Some particles that we use are electrically conductive, opening the possibility to include polymeric conductive domains in our fibers. When drawing these materials the conductive particles do not melt, but redistribute in the fiber, keeping the drawn composite materials with the desired property, such as electrical conductivity. Incorporation of composites was first demonstrated by [21]. Compound or material synthesis and reaction during thermal draw is additional viable approach to incorporate materials that do not melt or able to be drawn in their final composition or state [13, 33, 34]. Fluid

instabilities preclude obtaining some desired fiber features such as very small domains in fibers. A substantial work [35, 36, 37] has shown that this phenomenon could be harnessed to produce submicrometer wires internal to the fiber. Particles internal to fibers were produced by post process heat treating the drawn fibers to induce fluid instabilities in the inner core of the fiber [38]. Maintaining multimaterial interfaces is challenging in silica clad fibers, since the processing is done at elevated temperatures, where diffusion is fast and reactions are readily occurring between chemically dissimilar materials. It was recently shown [24] how induction of thermal instabilities post fiber draw, paves the way to establishing contact between two chemically dissimilar materials, unattainable through a single step thermal draw process. Controlling and directing fluid instabilities in fibers opens a route to pattern the fiber structure in the axial direction. This process yields a periodic structure of spheres, breaking the transversial symmetry of the fiber. Another example for establishing control over the axial fiber structure is induction of porosity in the fibers, as was recently demonstrated in the thesis of Benjamin Grena [39]. This approach allows to alter the structure of the fiber in three dimensions by inducing phase separation internal to the fiber cladding, enabling to attain porous structure in the fiber. A third example to this control is shown by Sorin et. al. [40]. Here, an ability to resolve an optical illumination distribution along an axially symmetric photodetecting fiber was demonstrated. Usually the signal is averaged along the fiber length, but in this case a capability to detect the location the light impinged the fiber was discovered.

1.6 Thesis outline

This thesis will focus on two main approaches to circumvent the above mentioned fiber thermal draw limitations.

In Chapter 2 we present an approach to control and direct fluid instability in thermally drawn fibers in a selective manner. We draw, from a macroscopic preform, fibers that have three parallel internal non-contacting continuous domains; a semiconducting glass between two conductors. We then heat the fiber and generate a

capillary fluid instability, resulting in the selective transformation of the cylindrical semiconducting domain into discrete spheres while keeping the conductive domains unchanged. The cylindrical-to-spherical expansion bridges the continuous conducting domains to create 10^4 self-assembled, electrically contacted and entirely packaged discrete spherical devices per meter of fiber. The photodetection and Mie resonance dependent response are measured by illuminating the fiber while connecting its ends to an electrical readout.

Chapter 3 demonstrates the first thermally drawn light emitting fibers, which incorporate high efficiency semiconducting light emitting diodes, packaged with high conductivity metallic electrodes internal to the fiber. Approach to control the size of the fiber and the linear density of the devices is developed as well. Since all components are internal - machine washability is naturally achieved. Moreover, similar strategy was employed to incorporate micron-sized crystalline semiconducting photodetectors, that allows to register optic signals with high bandwidth. These fibers were weaved into fabrics which demonstrated light emitting and photodetecting capabilities. Intrafiber optic communication was demonstrated by placing light emitting fibers in front of photodetecting fibers. Additionally, information transfer from a light source to fabric was demonstrated through light source modulation.

Chapter 4 is a short summary of a work conducted in collaboration with FLIR corporation to develop a new fiber for optical explosive detection. This fiber leverages on a fiber archetecture developed previously in our group [12]. This fiber generation contains major structural improvements such a medium for light propagation in silica capillary, high bandwidth photodetectors, as reported in the previous chapter and heating wires for explosive detecting material heating for increased detection.

This thesis is concluded with future work and directions that could be further developed based on the achievements described here.

THIS PAGE INTENTIONALLY LEFT BLANK

Chapter 2

Self-assembled fiber optoelectronics with discrete translational symmetry

Some results displayed in this section were published [41]. Display of the text, verbatim, and figures is done under compliance with Nature Research author license policy.

2.1 Introduction and motivations

In recent years, multimaterial fiber devices with capabilities ranging from acoustic sensing to transduction [11, 18, 21, 22] to multimodal neural interfaces [28] have emerged. These devices typically contain continuous conductive domains spanned by a material that responds to a stimulus or excitation. Drawn from a fluid state, the interfaces between the disparate fiber materials define a surface tension that renders the continuous internal domains thermodynamically unstable with respect to their discrete counterparts [35, 38]. In general, any liquid cylinder, including a fiber in the liquid state, is not thermodynamically stable, and will break into a series of periodic spheres, if we wait long enough as discovered and explained by Plateau and Lord Rayleigh [30, 31, 32]. The breakup of a fluid thread into droplets is a pervasive effect that has been appreciated since ancient times, for example as shown in Figure 2-1.

Similar phenomenon happens during the thermal draw process, especially when

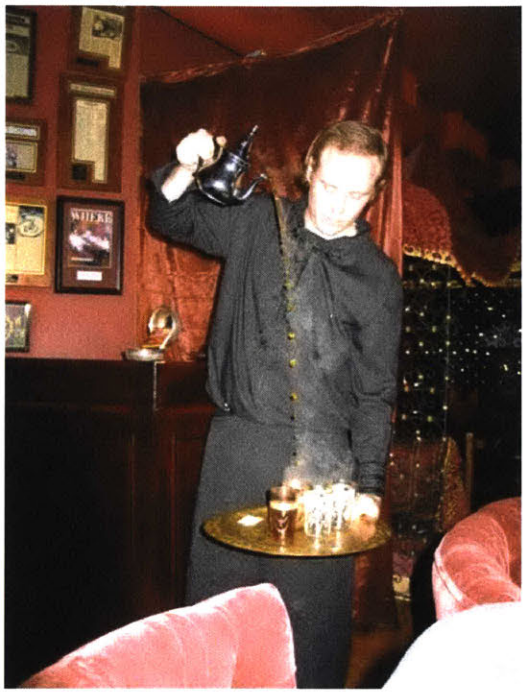

Figure 2-1: **Example to liquid cylinder break up**. The continuous liquid thread disintegrates into periodic array of spheres.

small domains or cores are present in the fiber. This phenomenon usually imposes a limit on the minimal size of a continuous domain in the fiber, and is mostly a function of the size, surface tension and the viscosity of the fiber core and clad, as will be discussed in the next sections. Until recently this phenomenon has been seen as a nuisance, and not reduced to practical utilization. Kaufman et al. [38] and Gumennik et. al. [24] have shown a way to produce a series of spheres in the fiber, by post draw heating of polymeric and silica clad fibers, respectively. This approach allows to obtain perfectly spherical particles made of chalcogenide glass, silicon or any other material that is able to be thermally drawn. Since these particles are formed internal to the fiber, it was not clear how to use them in a fiber device, since these need to be interfaced with other components in the fiber. Until recently, for any application, these spheres had to be extracted from the fiber for characterization or use in other devices. Here, the objective was to find a viable way to make fiber

devices that could leverage on these particles which are produced internal to the fiber, without extracting them out of the fiber cladding. To do so, the spheres need to be interfaced with other domains or cores in the fiber which will not necessarily break up into spheres. A fiber with multiple continuous internal fluid domains of disparate sizes and composition will, in principle, undergo breakup and form parallel arrays of spheres, each with its own periodicity, as illustrated by Figure 2-2(a). An experimental demonstration of such process is shown in Figure 2-2(b), where two copper cores in silica clad fiber were heated post draw and show how these cores break into spheres, both loosing continuity.

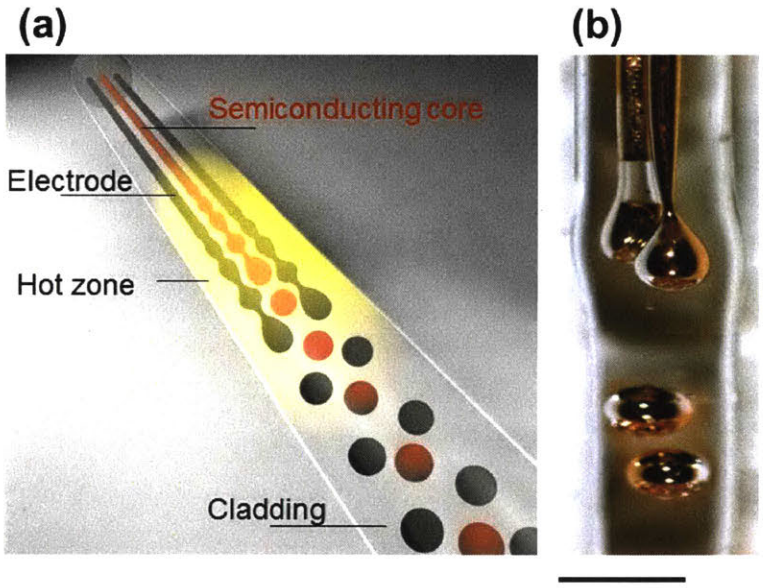

Figure 2-2: **Illustration of a typical multimaterial multicore fiber undergoing fluid instability**. (a) Illustration of the break-up process - a fiber that contains three cores. In this case no consideration made on the materials selection and design of the fiber for selective breakup. The top region of the fiber corresponds to continuous cores, the middle of the fiber is heated to induce fluid instabilities, and the bottom part of the fiber shows all cores disintegrate into periodic structure of spheres with no correlations between sphere location in each fiber cores. (b) Optical micrograph of two copper cores in silica clad fiber, which undergo break up when the fiber is heated. Scale bar is $400\mu m$.

However, since the kinetics of fluid instabilities are dictated not only by surface

tension, but also by the dimensions of the domain and its viscosity, one can consider the possibility of designing a fiber where a selective break-up occurs targeting only specific domains, while keeping others continuous as illustrated in Figure 2-3. By doing so, one could maintain the electrical transport benefits of the continuous domains while taking advantage of discrete geometries that offer differentiated device attributes.

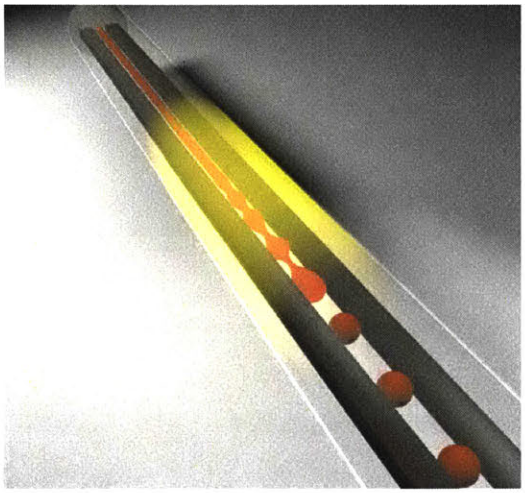

Figure 2-3: **Illustration of the desired fiber structure - selective breakup**. The top region of the fiber corresponds to continuous cores, the middle of the fiber is heated to induce fluid instabilities, and the bottom part of the fiber shows the central core that disintegrates into periodic structure of spheres while the other cores stay continuous

In the following sections, we report on thermal draw of a macroscopic preform, which results in a fiber that has three parallel internal non-contacting continuous domains; a semiconducting glass between two conductive polymers. We then heat the fiber and generate a capillary fluid instability, which results in the selective transformation of the cylindrical semiconducting domain into discrete spheres while keeping the conductive domains unchanged. The cylindrical-to-spherical lateral expansion bridges the continuous conducting buses to create $\sim 10^4$ self-assembled, electrically contacted and entirely packaged discrete spherical devices per meter of fiber. This results in photodetecting fiber devices with spherical active components, whose Mie

resonance dependent wavelength responsivity is measured.

2.2 Principles of selective break-up

Fluid instability in fibers can be described by an instability model for a cylindrical thread of viscous liquid (core of the fiber) that is surrounded by another viscous liquid (the cladding of the fiber) as developed by Tomotika [42]. According to this model, a sinusoidal perturbation of a wavelength λ grows exponentially with a time constant τ given by equation 2.1.

$$\tau = \frac{\tau_0}{(1-x^2)\,\Phi\,(x, \mu_{inner}/\mu_{clad})} \tag{2.1}$$

Where $x \equiv 2\pi a/\lambda$, a is the radius of the inner fluid, either the semiconducting core or the electrodes; $\tau_0 \equiv 2a\mu_{clad}/\gamma$, μ_{clad} and μ_{inner} are the viscosity of the cladding and the inner fiber component, respectively; γ is the interfacial surface tension between the two liquids. τ or $1/\tau$ are the perturbation growth time and rate respectively, and λ is the periodicity of the spheres that are present in the fiber after break up. The function Φ has the following form [42]:

$$\Phi\left(x, \frac{\mu_{inner}}{\mu_{clad}}\right) = \frac{N\left(x, \frac{\mu_{inner}}{\mu_{clad}}\right)}{D\left(x, \frac{\mu_{inner}}{\mu_{clad}}\right)} \tag{2.2}$$

Where

$$N\left(x, \frac{\mu_{inner}}{\mu_{clad}}\right) \equiv I_1(x)\Delta_1 - [xI_0(x) - I_1(x)]\Delta_2 \tag{2.3}$$

$$D\left(x, \frac{\mu_{inner}}{\mu_{clad}}\right) \equiv \left(\frac{\mu_{inner}}{\mu_{clad}}\right)[xI_0(x) - I_1(x)]\Delta_1 - \left(\frac{\mu_{inner}}{\mu_{clad}}\right)[(x^2+1)I_1(x) - xI_0(x)]\Delta_2 - [xK_0(x) + K_1(x)]\Delta_3 - [(x^2+1)K_1(x) + xK_0(x)]\Delta_4 \tag{2.4}$$

In these expressions Δ_1 - Δ_4 are all functions of x expressed in determinantal form as follows:

$$\Delta_1 = \begin{vmatrix} xI_0(x) - I_1(x) & K_1(x) & -xK_0(x) - K_1(x) \\ I_0(x) + xI_1(x) & -K_0(x) & -K_0(x) + xK_1(x) \\ \frac{\mu_{inner}}{\mu_{clad}} xI_0(x) & K_1(x) & -xK_0(x) \end{vmatrix} \tag{2.5}$$

$$\Delta_2 = \begin{vmatrix} I_1(x) & K_1(x) & -xK_0(x) - K_1(x) \\ I_0(x) & -K_0(x) & -K_0(x) + xK_1(x) \\ \frac{\mu_{inner}}{\mu_{clad}} I_1(x) & K_1(x) & -xK_0(x) \end{vmatrix} \tag{2.6}$$

$$\Delta_3 = \begin{vmatrix} I_1(x) & xI_0(x) - I_1(x) & -xK_0(x) - K_1(x) \\ I_0(x) & I_0(x) + xI_1(x) & -K_0(x) + xK_1(x) \\ \frac{\mu_{inner}}{\mu_{clad}} I_1(x) & \frac{\mu_{inner}}{\mu_{clad}} xI_0(x) & -xK_0(x) \end{vmatrix} \tag{2.7}$$

$$\Delta_4 = \begin{vmatrix} I_1(x) & xI_0(x) - I_1(x) & K_1(x) \\ I_0(x) & I_0(x) + xI_1(x) & -K_0(x) \\ \frac{\mu_{inner}}{\mu_{clad}} I_1(x) & \frac{\mu_{inner}}{\mu_{clad}} xI_0(x) & K_1(x) \end{vmatrix} \tag{2.8}$$

Where I_n and K_n are the modified Bessel functions of the first and second kind, respectively.

This timescale parameter shown by equation 2.1 is the main parameter which will enable selective break up in fibers. To hinder break up (make a domain with large value of τ), this core should have a large dimension a, and / or small interfacial energy γ. To facilitate break up, the domain should be small and have a large surface energy.

2.3 Materials selection and characterization

To demonstrate the principle of selective break up and explore its enabling properties, we have set our sight to obtain a structure with photodetecting properties. To do so, we need to integrate both conductors and semiconducting materials. The semiconductor core should disintegrate into a series of spheres, while the conductors must remain continuous after the fluid instability induction step. The fiber was designed

Table 2.1: **Fiber constituent properties**

Property	Expression	As_2Se_5	CPE	PC
Cross sectional radius (μm)	a	50	72*	
Surface tension with PC (mJ) [43, 44]	γ	114	30	
Viscosity at 230^oC (Pa·s)	η	$7 \cdot 10^4$	$1.2 \cdot 10^3$	$2 \cdot 10^4$
Activation energy (eV)	E_a	2.02		2.31

such that at a temperature range of $200 - 300^oC$, the capillary break-up timescale of the semiconducting core would occur over several minutes - an order of magnitude shorter than that of the conducting domains. With the above design criteria in mind, the inner core was chosen based on equation 2.1 to be an amorphous semiconducting material - As_2Se_5. The electrodes were chosen to be a carbon black filled polyethylene matrix (CPE), with lateral dimensions twofold greater than the semiconducting core. Polycarbonate (PC) was chosen as the cladding material as it is perfectly transparent in the visible and near-infrared wavelength domain, and allows for *in-situ* optical observation of the break-up process.

As to the selective break up problem, we used Tomotika model [42] to evaluate the timescales for break up, as a function of temperature, for the different components in the fiber structure. This calculation was carried out to demonstrate presence of conditions that allow to achieve selective break up. To perform the calculation we need to obtain the viscosity, surface energy, and size of the fiber components, as a function of temperature. The cross sectional radius and the surface tension were assumed to be constant with regards to the temperature. The values of the cross sectional radius and the surface tension with PC that were used for the calculations are summarized in Table* 2.1.

The viscosity of the fiber constituents were measured under varying temperature by rheometry, and fit to exponential functions, as the viscosity depends exponentially on the temperature. The results are shown in Figure 2-4.

The viscosity of PC and As_2Se_5 has been fitted to Arrhenius function: $\eta = \eta_0 \exp(E_a/kT)$,

*Effective cross sectional radius calculated from square cross section area.

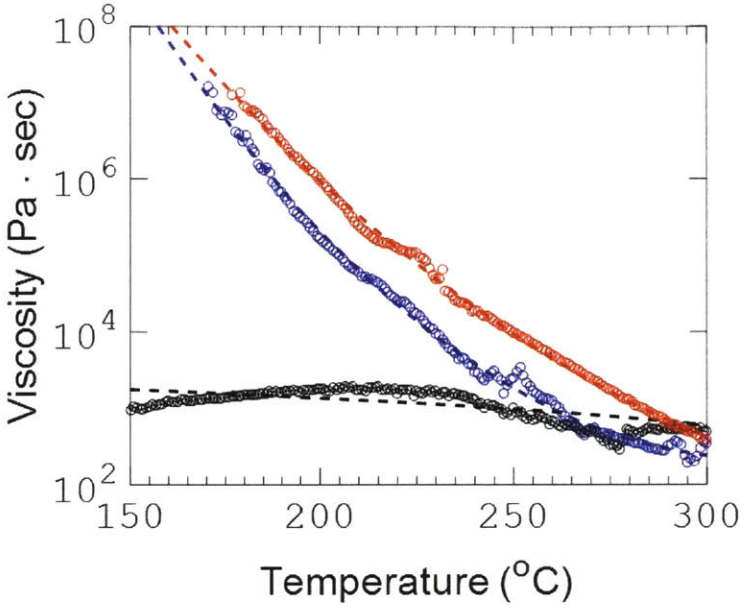

Figure 2-4: **Viscosity of fiber components** (PC cladding - blue; As_2Se_5 - red; CPE - black) as a function of temperature and fit to exponential functions (dashed lines)

where E_a is often referred to as the activation energy, such that $\eta_0 = 1.29 \cdot 10^{-19} \pm 4.9 \cdot 10^{-20}$ Pa·s and $E_a = 2.31 \pm 0.02$ eV for PC; $\eta_0 = 3.9 \cdot 10^{-16} \pm 5 \cdot 10^{-}17$ Pa·s and $E_a = 2.02 \pm 0.01$ eV for As_2Se_5. The viscosity of CPE weakly depends on the temperature, and was taken as a constant.

According to Plateau - Rayleigh and Tomotika theory, a characteristic rate for break up exists, and it is unique for every component in the fiber. The characteristic rate corresponds to the maximal perturbation growth rate possible, for a given set of parameters. The maximal rate (or minimal τ) is obtained for a characteristic wavelength - λ, which is a frequency referred to as the Tomotika wavelength. This characteristic wavelength, λ, is therefore set by the maximum of the function f:

$$f\left(\frac{\lambda}{a}\right) = \left[1 - \left(\frac{2\pi a}{\lambda}\right)^2\right] \Phi\left(\frac{2\pi a}{\lambda}, \frac{\mu_{core}}{\mu_{clad}}\right) \propto \frac{1}{\tau} \tag{2.9}$$

We can calculate the function f for a given temperature, and plot it as a function

of λ/a, to determine the maximum of this function that corresponds to the maximal disintegration rate, which will eventually determine the fiber structure, since it will disrupt the structure the fastest. A plot of f versus the paremter λ/a at a temperature of 230^oC, for the semiconducting core is shown in Figure 2-5.

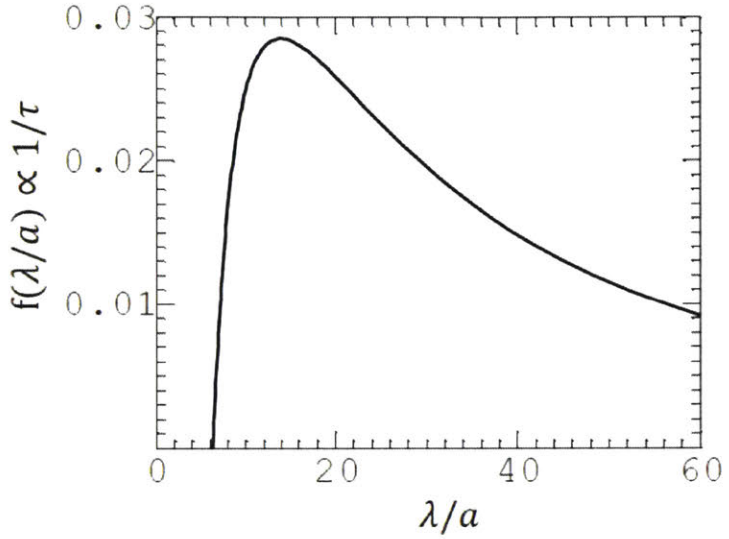

Figure 2-5: **Perturbation growth rate maximum visualization**. f - a function proportional to the perturbation growth rate $1/\tau$ as a function of the parameter λ/a at 230^oC, for the semiconducting core As_2Se_5

Accordingly, we are able to locate the maximum point of the function f which is at $\lambda = 13.66a$, where a is the radius of the initial core. Similarly, we have calculated the values of the maximal $(1/\tau)_{max}$ or minimal τ_{min}, for the electrodes and the core for temperature in the range of $150 - 300^oC$. These results are summarized in Figure 2-6. At a given temperature, whenever the fiber is heated for a time that exceeds this timescale ($t > \tau$), we expect this component to break up. The figure shows a fiber inner component "phase" diagram for both the semiconducting As_2Se_5 core and electrodes. The shaded green area denotes the conditions which will allow to achieve selective break up in the fiber. Presence of such area is a direct consequence of the materials used, and will change if the materials are altered.

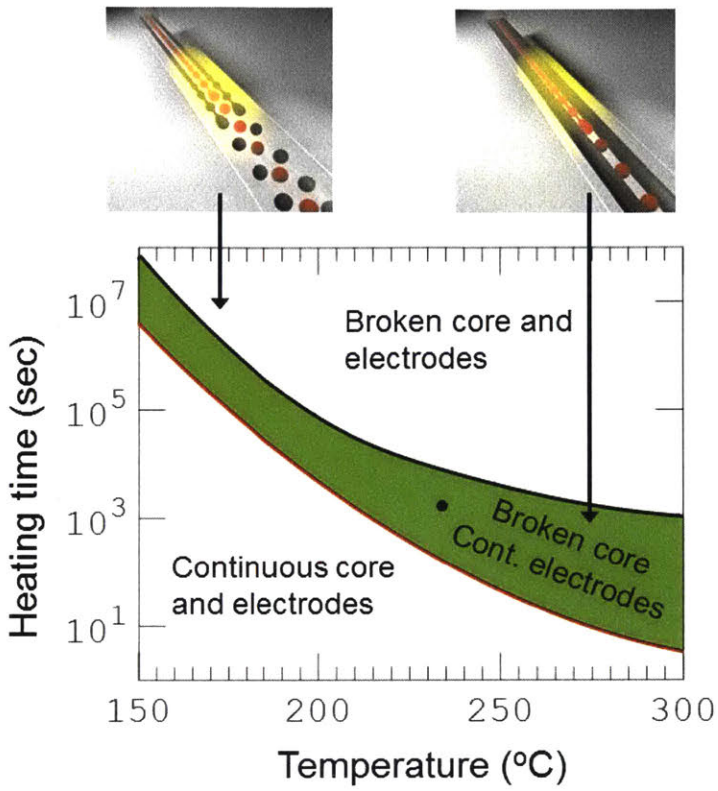

Figure 2-6: **Fiber inner component "phase" diagram**. Calculated for the semiconducting core (red) and electrodes (black). Long heating time of the fiber (post draw), at high temperature leads to electrode and core break-up, as demonstrated in top left inset figure. Lines correspond to the timescale of break-up. Selective break-up is achieved in the domain between the red and black curves (shaded green area), as demonstrated by the top right inset illustration. The conditions that were used in our case are denoted by a black circle

2.4 Preform preparation method

The fibers were produced starting with a macroscopic preform, such that when scaled down through a thermal drawing method, results in a fiber of the desired cross sectional structure. The structure of the preform is shown in Figure 2-7. In the preform, three main components are present - the cladding made of PC, two diametrically opposed square electrodes made of CPE, and an amorphous chalcogenide semiconducing core, made of As_2Se_5. It is important to note the varying depth of the electrodes in

the preform. This was intentionally introduced to the preform to accommodate the growth in radius when the inner core transforms from a cylinder to spheres. This later resulted in fibers with varying distance between the cylindrical core and the electrodes. Following the break up process, this feature allowed to select the fibers where a complete contact forms between the core and the electrodes, without the need for controlling the distances between the different domains in the preform and resulting fibers with high precision. Additionally, this allowed to obtain some fibers with the electrodes touching the semiconducting core, for reference measurements.

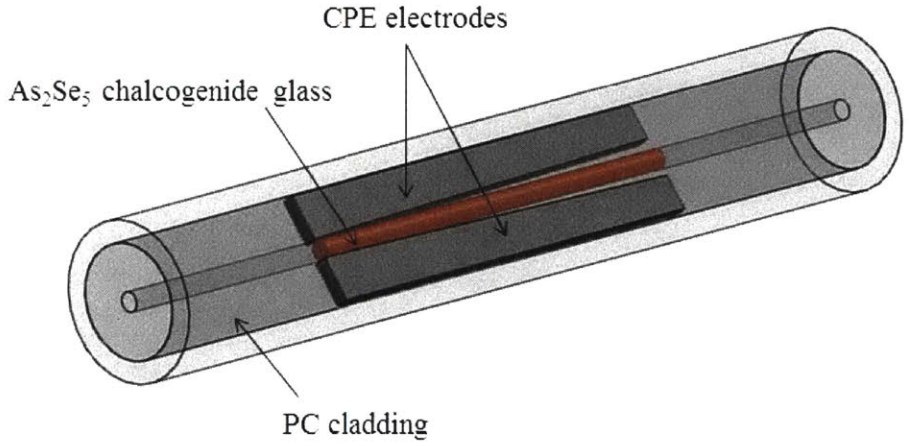

Figure 2-7: **Preform structure**

- The following protocol was followed when preparing the preform:

    1. The preform is made by rolling thin sheets of PC on a mandrel. The mandrel used was made of a metallic rod (McMaster Carr #88915K11) inserted into a Teflon (PTFE) tube with an external diameter of $\sim$ 4mm (McMaster Carr #5239K25).
    2. PC films with a 25μm thickness were rolled on the mandrel, followed by 75μm thick layers, until a preform of a diameter of 19mm was achieved. (Lexan 104, Laminated Plastics)

3. Thin Teflon film (McMaster Carr #4591K14) was then rolled on the prepared preform and was placed in a preheated vacuum furnace. The preform was heated at 190^oC for 15 minutes, under vacuum, while rotating the preform once, in the middle of the heating cycle. This process ensured consolidation between the layers.

4. Two pockets were milled at two diametrically opposed sides of the preform, approximately centered at the center of the preform. The pockets had a size of about 3mm in width, 90mm in length and their depth was varied along the length of the pocket. This depth linearly ranged from 5.5mm to 7.5mm.

5. Two CPE electrodes with similar dimensions as the milled pockets were inserted to these pockets. Description of electrode preparation procedure will be described shortly.

6. The mandrel was removed from the central core of the preform and an amorphous chalcogenide semiconductor rod was inserted to the core and aligned with the electrodes. Description of the semiconducting core preparation procedure will be described shortly.

7. Additional PC layers of 75μm thickness were further rolled on the preform, until a diameter of 36mm was reached. Additionally, PC rods (McMaster Carr #8571K42) were inserted to the central core of the preform, on both ends, to prevent the movement of the semiconducting core.

8. Again, some Teflon film was applied to the preform surface, and it was again consolidated in a vacuum furnace, heated to 190^oC. The preform was held for 40 minutes, under vacuum.

- The following describes the procedure to create polymeric conductive electrodes:

1. The CPE electrodes were prepared by stacking thin conductive polyethylene sheets (Hillas Packaging, #LAD5709) of a thickness of 100μm. 30 sheets were stacked to get the desired thickness of 3mm.

2. The stack was placed in a hot press between two metallic plates and pressed at the lowest possible pressure, at a temperature of 125^oC for about 20 minutes.

3. The pressed sheet was then milled to obtain the desired dimensions - electrodes of 3mm width, 90mm length and a linearly varying depth ranging between 5.5mm to 7.5mm.

- The following describes the procedure to make the amorphous chalcogenide semiconducting rod:

1. The chalcogenide material (As_2Se_5, AMTIR4, Amorphous Materials) was crushed to a powder form and inserted into a silica ampule with an inner diameter of 4 mm, which was prepared from a silica tube (Technical Glass Products, fused quartz tube 4x10mm), sealed at one end.

2. The ampule was evacuated in vacuum, sealed and placed in a rocking furnace. It was then heated at 650^oC for 10 hours and then quenched in air, by taking the ampule out of the heated furnace, and waiting for it to cool down in ambient air.

3. The solid rod is then extracted from the ampule and etched in 1M KOH (Sigma Aldrich) solution, to reduce the diameter of the rod, and match the preform inner diameter.

2.5 Fiber draw

The preforms were placed in the three zone draw tower to be drawn. The bate-off temperature set point was set to top zone - 150^oC, middle zone - 270^oC and bottom zone - 300^oC. The middle zone temperature of the furnace was slowly changed after a fiber emerged, usually increased up to 300^oC to maintain a low stress draw. (Stress under 100 gr/mm^2). The fibers were drawn down with a feed speed of 1 mm/min, and drawn at a speed of 1.6 m/min, which yielded a draw down ratio of $\beta = 40$. Figure 2-8 demonstrates the process of fiber draw - a fiber that contains a central

semiconducting core radius of 50μm, flanked by two electrodes placed in the proximity of the core with a gap to be bridged by the spheres in the break-up process.

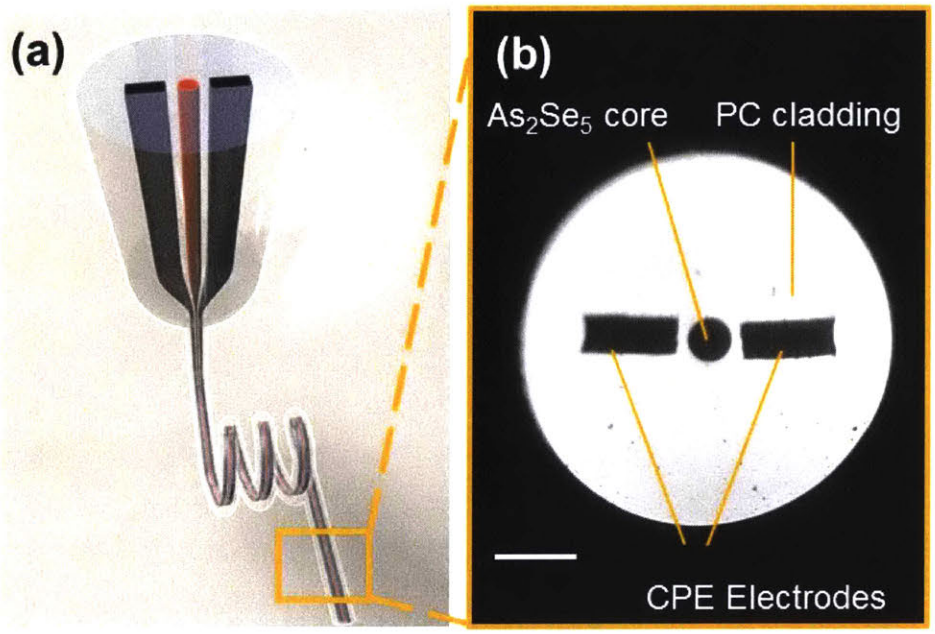

Figure 2-8: **Fiber structure and draw**. (a) Illustration of the fiber preform structure - chalcogenide glass (As_2Se_5) (red core) and two carbon black polyethylene composite (CPE) electrodes (black cores) are inserted into a polycarbonate (PC) cladding. The preform is scaled down in the drawing tower furnace into a fiber. (b) Optical micrograph of the cross section of the fiber shown in (a). The semiconducting core has a radius of 50 μm. (Scale bar, 200 μm)

It is worthwhile to note that the drawn structures do not undergo break-up during the draw process itself as the time the fiber spends in the hot zone of the furnace is much shorter than the timescale required for break up.

2.5.1 Obtaining smaller cores

To further reduce the radius of the semiconducting cores from 50 to 5 μm and 2.5 μm, the 50 μm core fiber was inserted into a core of subsequent preform made of PC and was redrawn. Extensions to the electrodes were added to the encapsulating preform at the redraw step to facilitate electrical interfacing to the redrawn fiber. The

following protocol describes the process of the redraw fiber and preform preparation:

1. A preform is made as described in the previous section and shown in Figure 2-7. This time, the size of the electrodes was altered. The distance between the core and the electrodes was kept constant at about 2.3mm. The other edge of the electrode was extended all the way until the outer surface of the preform. A thin layer of PC was wrapped around the preform to prevent CPE leakage from the preform during consolidation and draw. The final diameter of the preform was 40mm.

2. This preform was drawn to a fiber at a smaller draw ratio of $\beta = 20$, which resulted in a thick fiber of a diameter of about 2mm.

3. More PC layers were wrapped around the drawn fiber, which was used instead of a mandrel. The films were wrapped until a thickness of 19mm was achieved.

4. Two diametrically opposed pockets were milled in the preform, exposing the electrodes in the fiber. Additional electrodes were inserted in these pockets, such that these touch the electrodes of the fiber inserted into the preform.

5. Additional PC layers were wrapped around the preform to reach a final outer diameter of 30mm.

6. Two different draws were made with the stack and draw preform, each with a different draw down ratio. To obtain an inner core of radius of $5\mu m$, a draw down ratio of $\beta = 20$ was used, and to obtain a fiber with an inner core radius of $2.5\mu m$, the draw was made with a draw down ratio of $\beta = 40$.

The process of the draw and the resulting fibers are shown in Figure 2-9. This allowed to reduce the sphere diameter and hence to achieve spectrally resolvable resonant light interaction with the spheres. Generally, this approach allows forming electrical connection to a wide range of component sizes, demonstrating a hierarchical structure for electrical connection that produces a macroscopic electrical connection to microsphere array spanning three orders of magnitude of size difference.

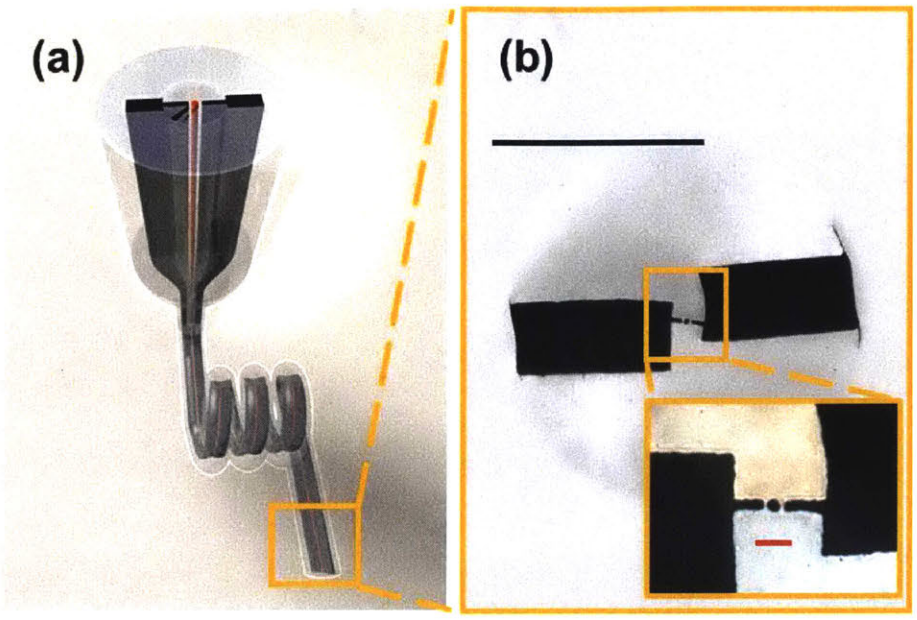

Figure 2-9: **Illustration of redraw process and redrawn fibers**. (a) The fiber illustrated in Figure 2-8(a) is inserted into another preform with extended electrodes to facilitate connection to the fiber after draw. This preform is drawn again in order to reduce the size of the chalcogenide core. (b) Optical micrograph of a redrawn fiber with extended electrodes and a chalcogenide core of 5μm radius; Inset - optical micrograph of the active region of the redrawn fiber. (Top black scale bar, 100μm; Bottom red scale bar, 20μm).

2.6 Inducing selective break up

After the fibers drawn step, these were placed on a hot plate and heated isothermally at 230^oC, a temperature at which both the semiconducting core and the polymeric cladding are in liquid / soft state with a low enough viscosity such that the break-up happens reasonably fast. Several fibers obtained at different stages of the draw were heated, to find the distance that will ensure a well established electric contact between the spheres and the electrodes, and without hindering the break up process, as shown in Figure 2-10(a).

Figures 2-10(b)-(d) show the evolution of the fiber structure during the break up of a 50μm radius central core fiber. The chalcogenide core breaks into spheres with periodic pitch, while the electrodes remain intact. A self-assembled fiber structure is

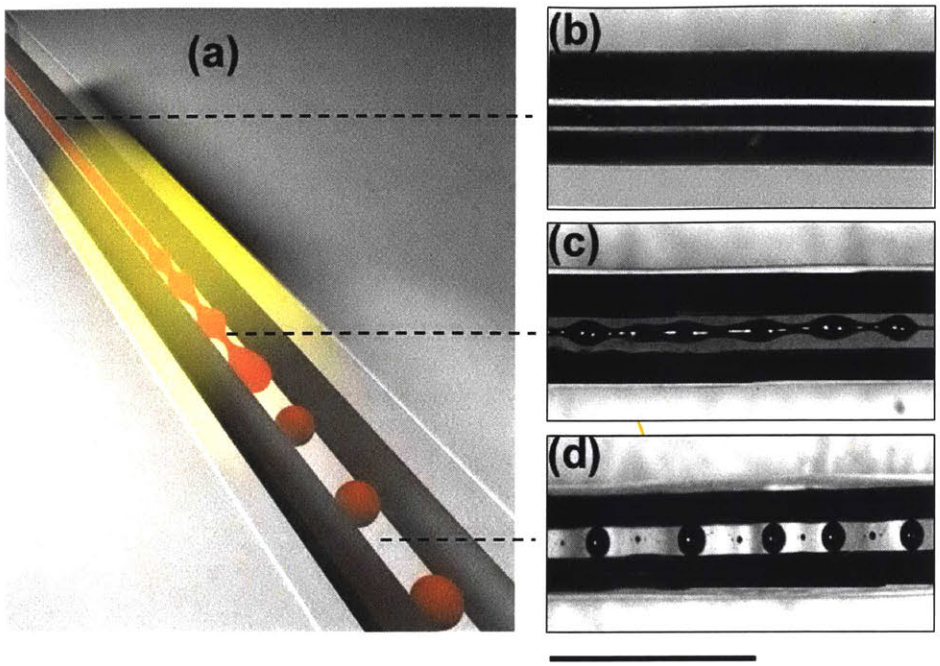

Figure 2-10: **Evolution of selective break-up in fibers**. (a) Illustration of the selective break-up process in the fiber. (b) Optical micrograph of a fiber with a semiconducting core radius of 50μm designed to undergo selective break up, before break up. (c) Optical micrograph of a fiber during the onset of break up process - the inner core develops instability, while the electrodes are kept continuous. (d) Optical micrograph of a fiber after break up with chalcogenide glass spheres with a radius of 107μm, connected to continuous electrodes. (Scale bar, 1 mm).

achieved with a broken translational symmetry along the fiber axis. This approach is universal, scalable in size and can be used over a wide set of materials, paving the way for a new set of hitherto unachievable fiber devices.

The ratio between the sphere radius, R, and the core radius, a, can be derived from volume conservation as shown in equation 2.10, where λ is the period spacing between the spheres along the fiber axis.

$$\frac{R}{a} = \sqrt[3]{\frac{3\lambda}{4a}} \tag{2.10}$$

Along with the Rayleigh condition - $\lambda \geq 2\pi a$ [31, 32] the resulting sphere radius is

larger than the initial core radius. As the capillary break-up starts from an arbitrary perturbation in the core radius, it is expected that the distance between two adjacent spheres should correspond to the perturbation wavelength with the minimal time constant (or the maximal growth rate). The perturbation wavelength that is associated with the shortest growth time constant in our case, according to equation 2.1 is $\lambda \cong 13.66a$. Assuming volume conservation, we get that $R = 2.17a$. These relations, which are derived from Tomotika model [42], were found to be in a good agreement with our experimental results obtained for the current core radius. We note that the distance between the electrodes and the semiconducting core in the preform was subsequently designed such that it is approximately equal to $(R - a)\beta$.

2.6.1 Sphere size and size distribution

The sphere size is relatively uniform, but should be considered polydisperse, with a standard deviation to mean ratio of 9%. The sphere radius and subsequent pitch period distribution could be attributed to distribution of initial perturbation amplitudes, which would result in a dispersion in sphere radii. Figures 2-11, 2-12 and 2-13 show the fiber structure for different fiber core sizes, which result in spheres radius of 107μm, 11μm and 5μm respectively. We have found that a normal distribution fits well the distribution of sphere radii, where the stated error is the standard deviation of the distribution. As can be seen in Figures 2-11 and 2-12, there are contacts between the vast majority of the spheres and the electrodes for spheres of radius of 107μm and 11μm. Some of the 5μm spheres are not connected to the electrodes, as seen in Figure 2-13, due to a shape fluctuation of the electrodes during the break up process. This causes the fiber structure to have a lower conductivity and responsivity as will be shown further in the next section. Additionally, as can be seen in Figures 2-11(b), 2-12(d) and 2-13(c), the semiconducting particles are very close to spherical. By measuring their diameter in two perpendicular directions allows us to estimate the ellipticity of these particles. The ratio between the minor and major axes yields in a maximum ratio of $\frac{d_{minor}}{d_{major}} = 0.95$. Thus, we assume that the particles are very close to spherical.

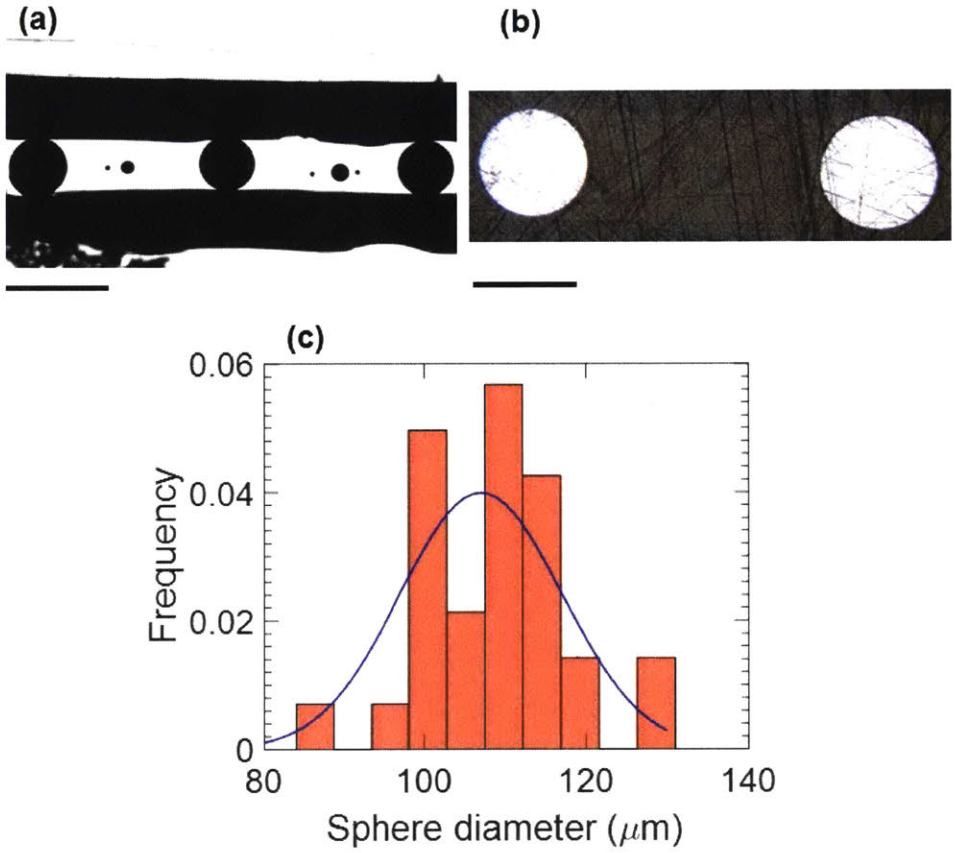

Figure 2-11: **Sphere shape and distribution, average sphere radius of** $107\mu m$. (a) Transmission optical micrograph of a fiber after break up, which contains semiconducting spheres with an average radius of 107μm and CPE electrodes. Scale bar - 400μm (b) Reflection optical micrograph of the fiber shown in (a). Scale bar - 200μm. (c) Sphere radius distribution estimation, from a sample of 30 spheres - average radius - 107μm , standard deviation - 10μm

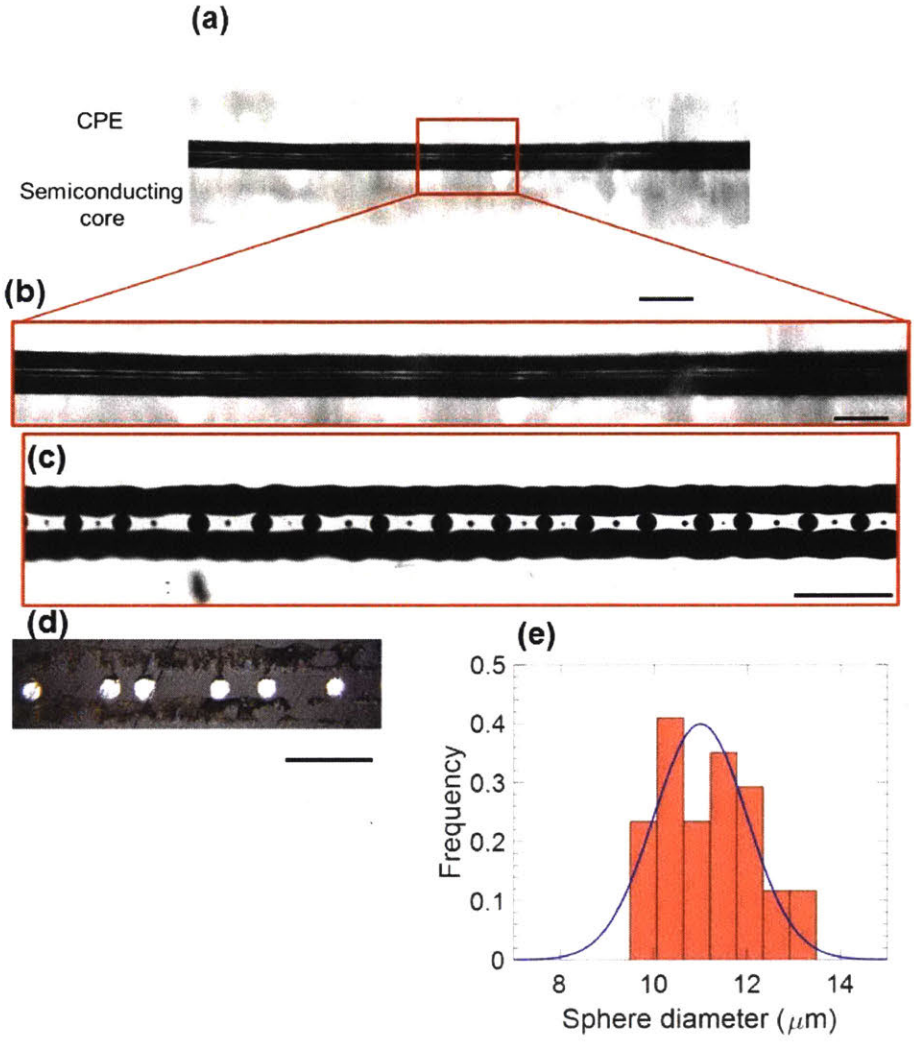

Figure 2-12: **Sphere shape and distribution, average sphere radius of** $11\mu m$. (a) Transmission optical micrograph of a fiber with a semiconducting core radius of 5μm designed to undergo selective break up - prior to break up. Scale bar - 200μm. (b) Transmission optical micrograph of the active region in the fiber, shown by the red square in (a), with a greater magnification. Scale bar - 100μm. (c) Transmission optical micrograph of a fiber after break up with chalcogenide glass spheres with an average radius of 11μm, connected to continuous electrodes. Scale bar - 100μm. (d) Reflection optical micrograph of a fiber shown in (c). Scale bar - 100μm. (e) Sphere radius distribution estimation, from a sample of 30 spheres - average radius - 11μm , standard deviation - 1μm .

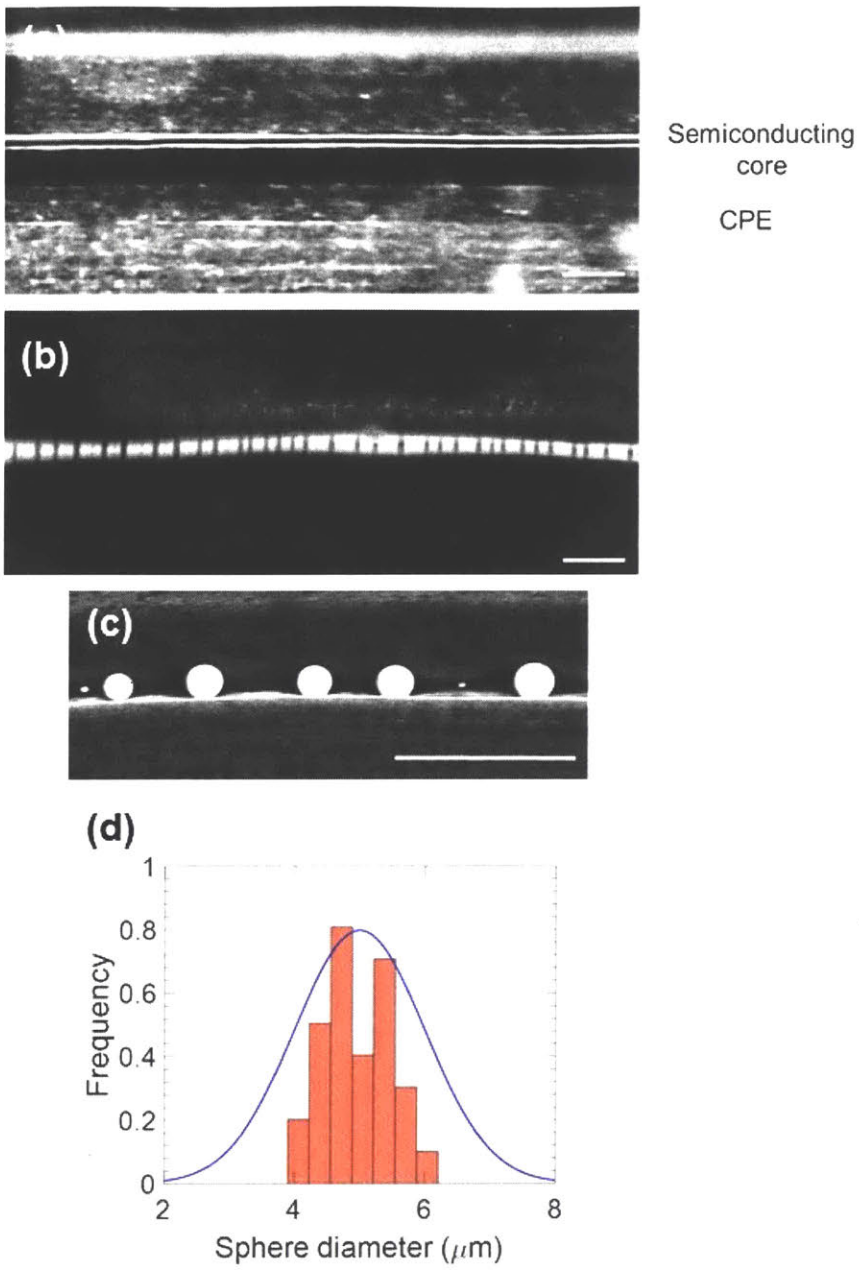

Figure 2-13: **Sphere shape and distribution, average sphere radius of** $5\mu m$. (a) Transmission optical micrograph of a fiber with a semiconducting core radius of 2.5μm designed to undergo selective break up - prior to break up. Scale bar - 60μm. (b) Transmission optical micrograph of a fiber after break up with chalcogenide glass spheres with an average radius of 5μm, connected to continuous electrodes. Scale bar - 60μm. (c) Scanning electron microscopy micrograph of a fiber with average sphere radius of 5μm, after chemical removal of the fiber cladding. Scale bar - 50μm. (d) Sphere radius distribution estimation, from a sample of 30 spheres - average radius - 5μm , standard deviation - 0.5μm .

Table 2.2: **Summary of the initial core and sphere radii and period wavelength of the sphere separation after the break up**. Errors shown correspond to standard deviations.

Continuous core radius a (μm)	Sphere radius R (μm)	Period Wavelength λ (μm)
50±1	107±110	660±90
5±0.1	11±1	68±12
2.5±0.7	5±0.5	35±5

Additionally, the relationship between the core and sphere radii and the sphere appearance wavelength are summarized in Table 2.2 and were compared to the expected values from Tomotika model. These were found to be in a good agreement with our experimental results obtained for different core radii.

2.7 Photoresponse characterization

The electro-optical behavior of the fibers post break-up was characterized by illuminating the fiber structure with a continuous wave Ti:Sapphire laser source (Coherent Mira900) with a wavelength of 760±1 nm (measured by optical spectrum analyzer Ando AQ6317B), power of 55mW (measured by Newport 2936-R), through a spherical lens that resulted in a spot full width half maximum (FWHM) radius of 22 μm. The light was incident with an angle of 90^o with regards to the fiber axis, as shown in Figure 2-14(a). The electric current was recorded for various forward and reverse voltages, under dark and with laser illumination conditions (Kiethley 6487/6517A). Figure 2-14(b) shows the IV curve of a fiber that contained spheres with a radius of 11μm. The current at a given voltage is considerably higher when it is illuminated - exhibiting a noticeable photoresistive effect. The theoretical dependence of the current on the applied voltage is described in Appendix A.

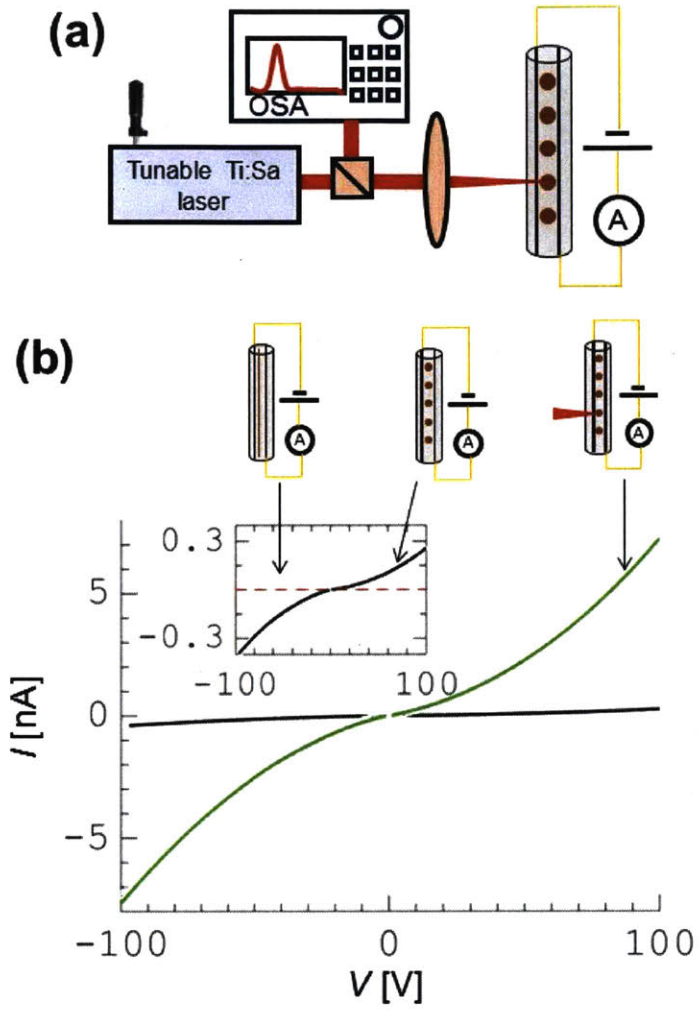

Figure 2-14: **Photodetection measurement set-up and photoresistance characterization**. (a) Schematic representation of the experimental set-up used to characterize photodetection and resonative photoresponse of selectively broken fibers. The fibers are illuminated with a Ti:Sapphire laser (operated at a wavelength of 760 ± 1 nm, and power of 55 mW), while the laser power, spectrum and fiber photoresponse is being recorded simultaneously. (b) Main figure - measured current versus voltage curve of the photodetecting fiber with spheres with an average radius of 11μm under laser illumination (green), compared with the dark current (black). The setup shown in (a) was used, while illuminating a single sphere; Inset - IV curve obtained in the dark (black), the dark current of the fibers prior to break up (dashed red line) - shows no measurable current due to lack of contact between the semiconducting core and the electrodes.

Further experimental results made with 5μm radius spheres are shown in Figure 2-15.

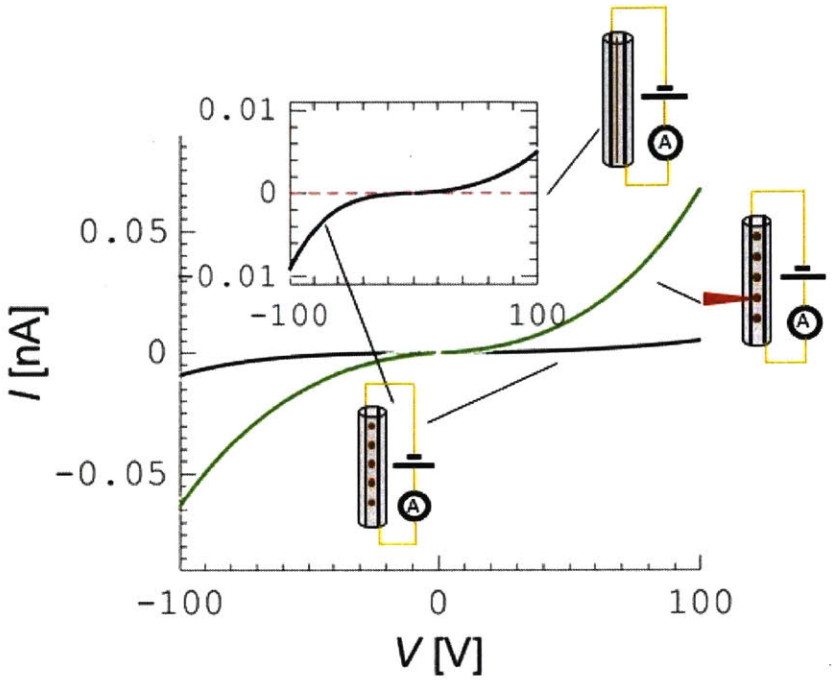

Figure 2-15: **Photoresistance characterization for a fiber that contains spheres with a radius of 5μm.** Main figure - Measured current versus voltage curve of the photodetecting fiber with spheres with an average radius of 5μm under laser illumination (green), compared to the dark current (black). The setup shown in Figure 2-14(a) was used, while illuminating a single sphere; Inset - IV curve obtained in the dark (black), the dark current of the fibers prior to break up (red) - shows no measurable current due to lack of contact between the semiconducting core and the electrodes.

The self-assembled structure has photodetecting properties, and it is the first photodetecting structure obtained through selective break-up in fibers. This result demonstrates the ability to integrate electronic devices in two steps - fiber draw and subsequent heat treatment. The photoresistive behavior of these fibers is similar, in principle, to previously demonstrated fibers [19, 45, 46], that contained continuous semiconducting core and conductors in contact, although a different semiconducting material was used. The measured dark and photo-currents in the spherical semicon-

ducting fibers depend on the geometrical dimensions of the devices, such as the small contact area between the electrodes and the core, which influence the absolute value of both currents, together with the excitation wavelength and the laser power. This was taken into account and further discussed in Appendix A.

2.8 Resonative photoresponse characterization

Spherically shaped structures are perfect candidates for resonant light coupling, and are extensively used as optical filters or gain media [47, 48]. Chalcogenide glass resonators were fabricated previously using a multitude of approaches [49, 50, 51]. The majority characterization attempts of the resulting devices have focused on the optical properties of a single sphere, manipulated individually and evanescently coupled to a tapered fiber or a waveguide. Using the approach mentioned above, we were able to obtain a large amount of in-fiber integrated chalcogenide spheres contacted by continuous electrodes in parallel. Optical resonances in this configuration can be directly coupled to photodetection, which results in increased photoconduction, that is directly registered by electronics interfaced to the device electrodes. This modality was not previously achievable with photodetecting fibers [19, 45, 46] as the core shape was cylindrical, whereas, with spherical semiconducting core, photoelectric resonances become available. Such photoelectric resonances in a single sphere were recently reported [52]. Mie's theory [53, 54] is used here to explain the resulting resonant behavior of our fiber devices. Prior to displaying the results obtained in this work, an overview of Mie scattering theory will be discussed.

2.8.1 Mie resonances theory

Mie theory [55] describes the interaction of electromagnetic radiation with spherical particles. The ultimate result of the theory is given by the scattering, extinction and absorption factors. We focus on the absorption as it will directly affect the absorption of the light in the semiconductor which could be measured through the response of the photodetecting spheres in the fibers. We have measured the refractive index

and the extinction coefficient of As_2Se_5 by spectrophotometry using an evaporated film (thickness of $18\mu m$) of this material, and employing Swanepoel method [56] to calculate the refractive index of the material. The results are shown in Figure 2-16.

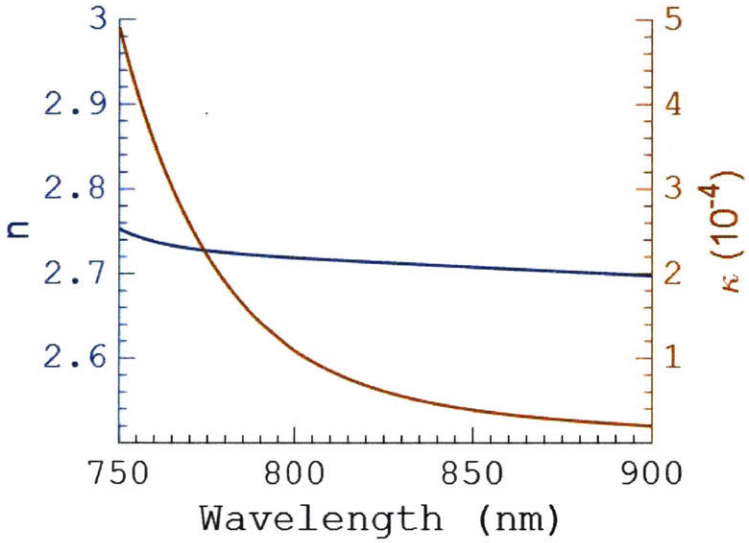

Figure 2-16: **Index of refraction and extinction coefficient of** As_2Se_5.

Using the values of the refractive index and extinction coefficient we obtain Q_{abs} - the normalized absorption cross section of a sphere, as defined in the following reference [53]. This value describes the interaction of electromagnetic radiation with the sphere and is the ratio between the absorbed photo-energy versus the incident energy, when the sphere is illuminated. The Q_{abs} was calculated for different sphere radii of 5μm, 11μm and 107μm as shown Figure 2-17.

From this figure we can notice that for smaller spheres there are resonant peaks present and the free spectral range (FSR) between these peaks get larger, as the sphere diameter is reduced, as expected from theory. These features are then measured through the photoresistive response of the fiber that contains spheres with the aforementioned radii.

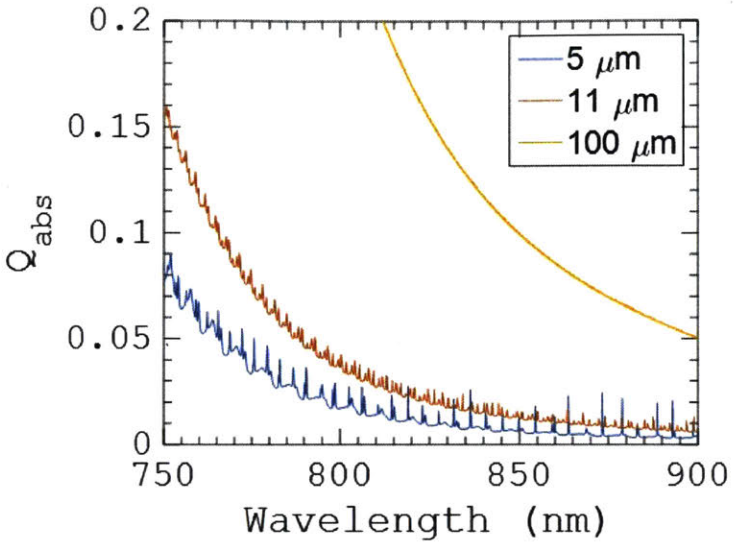

Figure 2-17: Q_{abs} **calculated by Mie theory vs. wavelength for different sphere diameters.**

2.8.2 Experimental results

The resonances were characterized using an experimental set-up illustrated in Figure 2-14(a). The fiber was illuminated with a continuous wave radiation of a Ti:Sapphire laser with a spectral width (FWHM) below 1 nm. This laser source was chosen since it delivers up to 100mW narrow band radiation at the desired wavelength range of 750 to 900 nm - near the absorption edge of As_2Se_5. Two different modes of illumination were investigated: a single sphere excitation - by focusing the light through a spherical lens as shown in Figure 2-18(a)(FWHM of 22μm), and a multi-sphere excitation - by illumination through a cylindrical lens, as shown in Figure 2-18(b) (two-dimensional Gaussian beam with a FWHM of $462 \times 180\mu m$), to produce an elliptical light spot.

For a given sphere radius, the photocurrent was mapped as a function of wavelength while the laser wavelength and the power were concurrently monitored. The photoelectric responsivity, ρ_m, as defined in Appendix A, and specifically by equation A.16, was measured as a function of wavelength, and is shown in Figure 2-19(a) for a 5μm sphere radius in the case of single - sphere excitation, Figure 2-19(b) shows

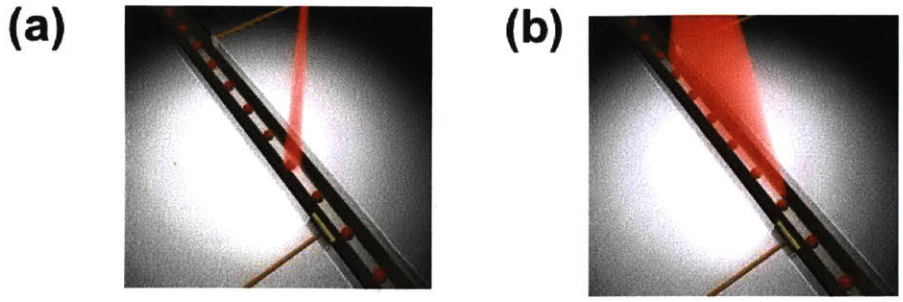

Figure 2-18: **Resonative photodetection characterization setup**. (a) Illustration of the fiber characterization area where only one sphere is excited by the laser (through a spherical lens). The laser wavelength was tuned continuously. The measurements of the current, wavelength and the laser power were recorded, as shown in Figure 2-14(a). (b) Illustration of the fiber characterization area where several spheres are excited by the laser (through a cylindrical lens).

results for a 5μm sphere radius in the case of multi - sphere excitation. Similar results were obtained for spheres with a radius of 11μm and the results are shown by Figures 2-19(c)-(d) for single and multi - sphere excitation, respectively.

The theoretical prediction based on Mie theory, both for single and multi-sphere excitation was calculated and is expressed in terms of the calculated responsivity, which was shown to be proportional to the normalized absorption cross section Q_{abs} and is denoted by a red curve in the plots. The results in Figure 2-19 suggest that both the measured and the theoretically calculated responsivity contain resonant, periodic features. Due to sphere polydispersity, Mie resonances are less pronounced in the case of multiple sphere excitation, consistent with previous findings [57, 58]. The polydispersity was taken into account when estimating the theoretical responsivity for multi - sphere excitation. This was performed by randomly drawing a finite number of sphere radii out of a normal distribution with the measured radius mean and corresponding standard deviation. The number of samples was chosen according to equation 2.11, where N_{sample} is the number of samples selected, l_a is the FWHM size of the spot size used to excite multiple spheres and λ is the wavelength at which

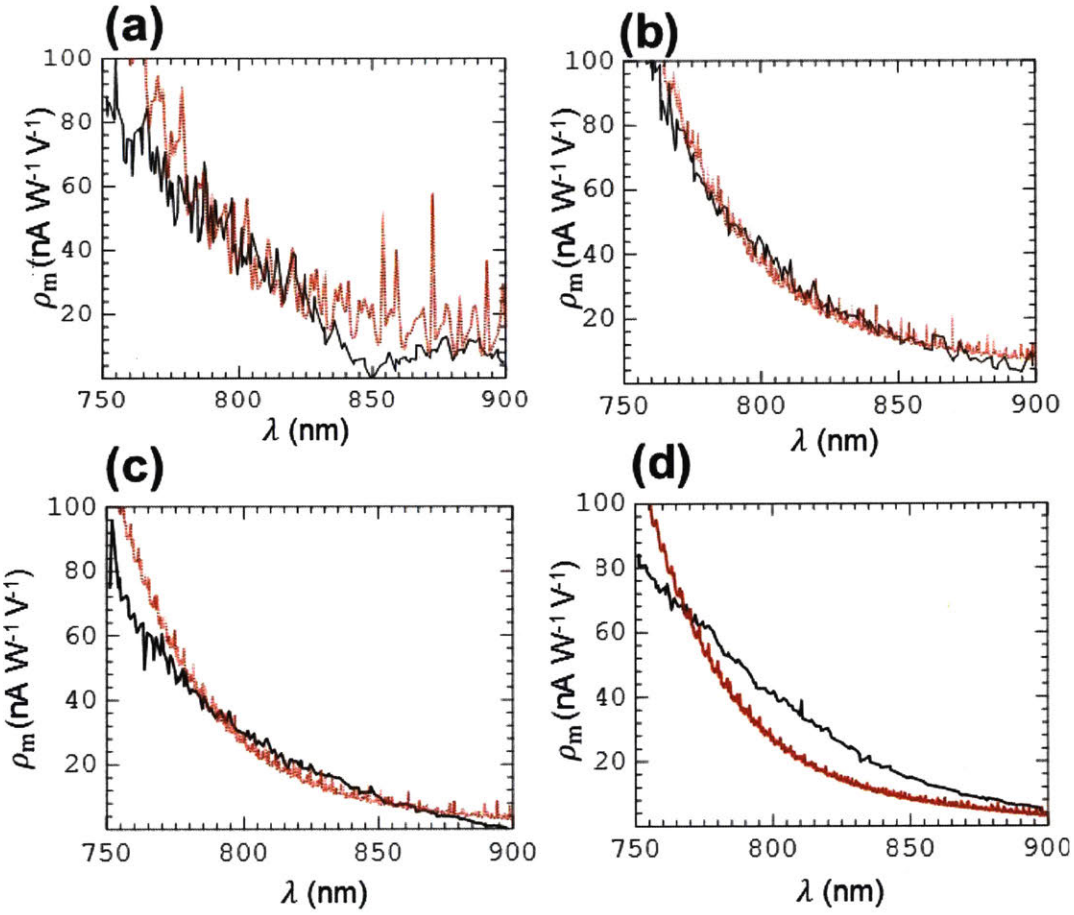

Figure 2-19: **Resonative photodetection characterization results.** (a)Experimentally measured responsivity (black) compared with theoretically calculated responsivity (red) as a function of wavelength for a fiber with a sphere radius of 5μm. The fiber was illuminated by a spherical lens in a single sphere excitation as described in Figure 2-18(a). (b) Experimentally measured responsivity (black) compared with theoretically calculated responsivity (dashed red) as a function of wavelength for a fiber with a sphere radius of 5μm. The fiber was illuminated by a cylindrical lens in a multiple sphere excitation as described in Figure 2-18(b). Here the polydispersity of the spheres was taken into account. The resonant peaks are less pronounced due to the polydispersity of the spheres. (c) Similar setup as shown in (a), for a fiber containing spheres of a radius of 11μm. (d) Similar setup as shown in (b), for a fiber containing spheres of a radius of 11μm.

the spheres appear in the fiber (Tomotika wavelength). For fibers with spheres with a radius of 5μm, we have included 13 spheres in the calculation, and for fiber with

spheres with a radius of 11μm, we have included 7 spheres in the averaging calculation of the responsivity. This averaging leads to "smoothing" of the sharp Mie peaks, but since we are interacting with a relatively small amount of spheres, Mie peaks are still present, as can be seen in Figures 2-19(b) and (d).

$$N_{sample} = \frac{l_a}{\lambda} \tag{2.11}$$

Mie resonances are expected to be periodic in the k-space (or the frequency domain) [53, 59], thus to quantitatively characterize the periodic features recorded in the measurements and obtained in the calculations, we performed a fast Fourier transform (FFT) analysis. We first transform the measurements in to an optical frequency domain (or k-space), we then obtain the FFT and finally rescale the horizontal axis to wavelength units to highlight the Mie scattering FSR. Figure 2-20 and 2-21 describe the FFT analysis of the measured responsivity and the calculated theoretical responsivity for a single and multiple sphere excitation setup of fibers containing spheres with radii of 5μm and 11μm, respectively.

Since the sphere size is much larger than the wavelength used for characterization, multiple resonant modes are allowed to exist. Thus, we have focused our efforts on finding the primary mode which has the largest FSR. A resonance frequency at 8.5 $\pm$ 0.5nm is present for the measured responsivity of single sphere excitation and is 8.8nm for the calculated responsivity (marked by arrows), supporting the claim that resonances were present in the responsivity of the photodetectors due to the spherical shape of the detecting elements. This FFT peak is broader for multi-sphere excitation due to the polydispersity of the spheres. The experimental and theoretical dependence of the resonant peak on the sphere size and excitation regime is summarized in Figure 2-22. A good agreement is achieved between theory and experiment. In particular, the experimental results confirm the theoretically derived inverse proportionality dependence of the FSR on the sphere radius, and expected based on the conventional Fabry Perot resonator theory. Both single sphere and multi-sphere excitations showed very similar FSRs, supporting the prediction that

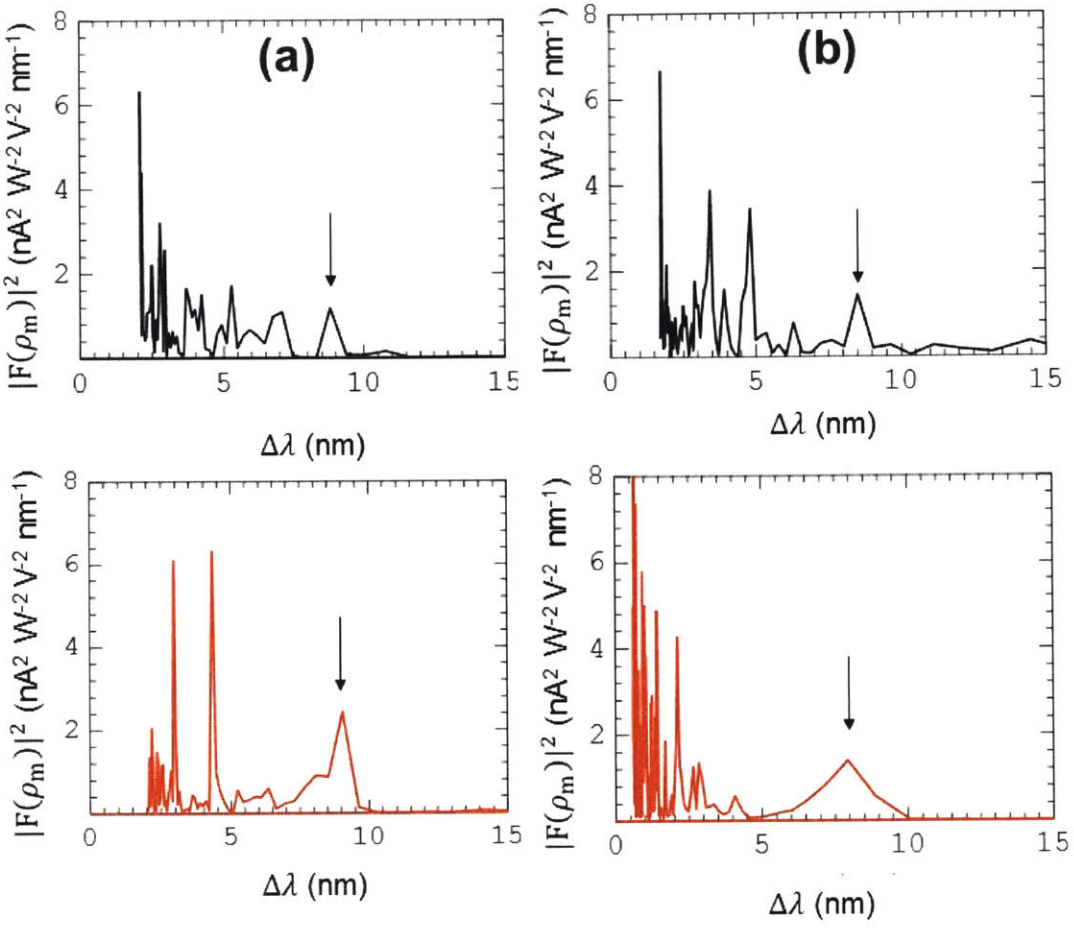

Figure 2-20: **FFT analysis of resonative photodetection - 5μm spheres.** (a)The FFT density of the experimental responsivity (black) and the theoretical responsivity (red) as a function of wavelength between two adjacent resonant peaks are described in the upper and the lower graphs, respectively, calculated for a single sphere excitation. The location of the first order peak in the experimental and the theoretical results is $\Delta\lambda = 8.5 \pm 0.5$nm and $\Delta\lambda = 8.8$nm, respectively (marked by an arrow). (b) Similar FFT analysis, calculated for multiple spheres excitation.

the resonances are due to intra-sphere light interferences (which are dominant in our case) as opposed to inter-sphere interactions. Intra-sphere interactions are most likely dominant due to the regime of excitation - perpendicular to the fiber axis.

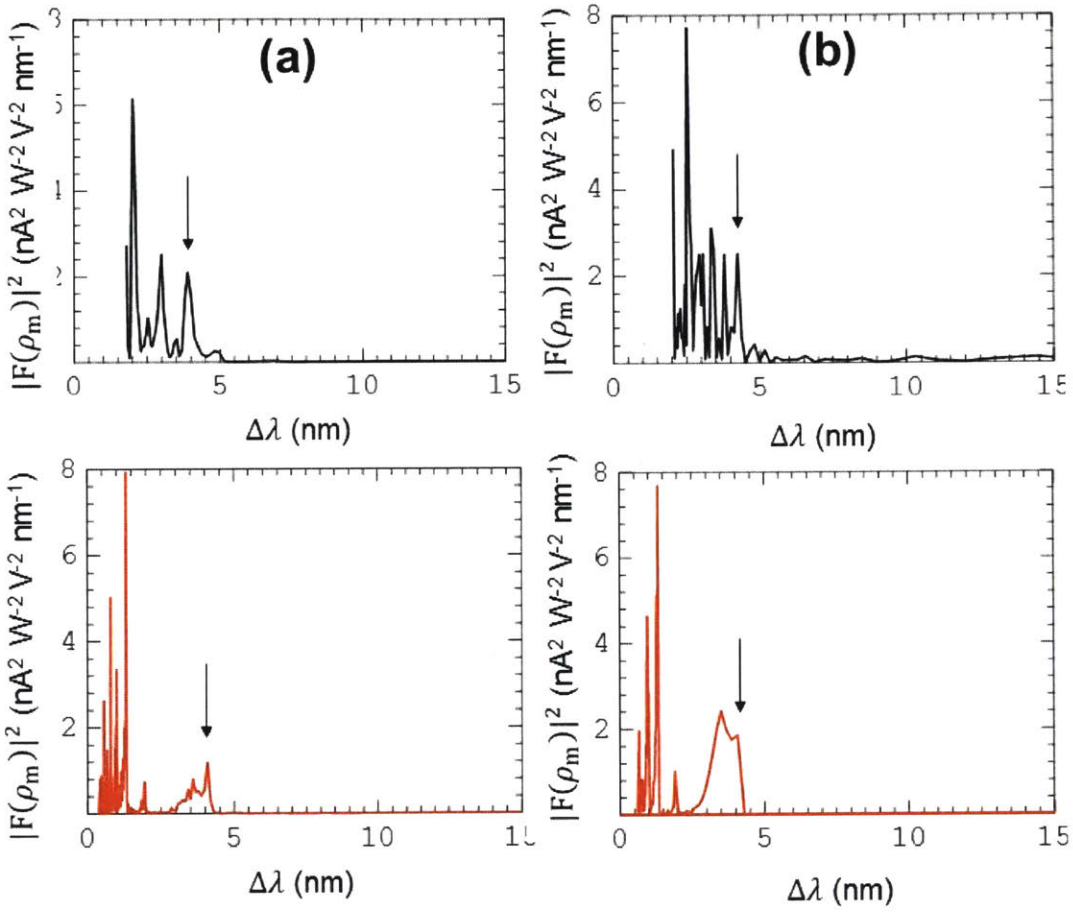

Figure 2-21: **FFT analysis of resonative photodetection - 11μm spheres**. (a)The FFT density of the experimental responsivity (black) and the theoretical responsivity (red) as a function of wavelength between two adjacent resonant peaks are described in the upper and the lower graphs, respectively, calculated for a single sphere excitation. The location of the first order peak in the experimental and the theoretical results is $\Delta\lambda = 4.15 \pm 0.3$nm and $\Delta\lambda = 4.2$nm, respectively (marked by an arrow). (b) Similar FFT analysis, calculated for multiple spheres excitation.

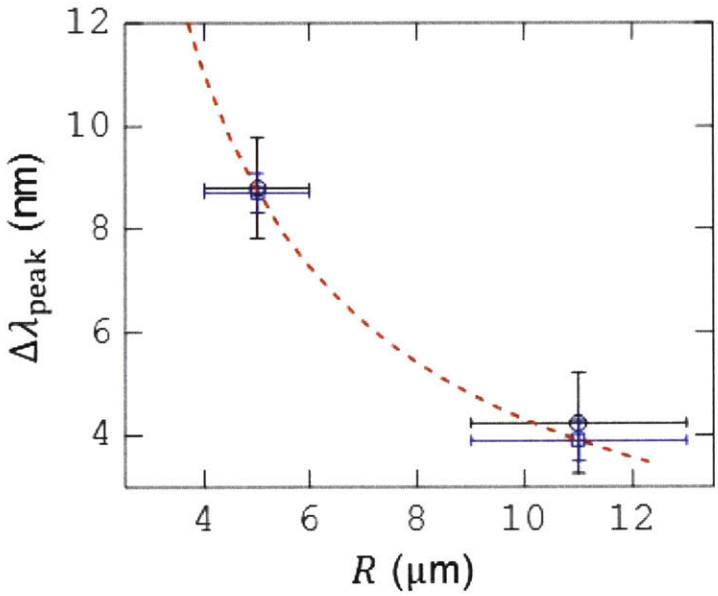

Figure 2-22: **Experimental and theoretical dependence of the resonant peak on the sphere size and excitation regime**. Comparison between the theoretical peak location of the FFT density as a function of sphere radius (red dashed-line), for the case of single sphere and the experimental results for single - (black circle) and multiple-sphere excitation (blue square) is presented. Error bars correspond to 95% confidence interval, both for the wavelength peak location and the sphere radii.

2.9 Discussion and conclusions

The results mentioned above, demonstrate in-fiber self-assembly of discrete semiconducting micro-spheres with axially continuous electrodes that form electrical contacts and produce fully packaged devices along meters of fiber. A fiber containing a semiconducting core and two conductive domains that are electrically insulated from each other. Subjected to heating, the Plateau - Rayleigh effect [31, 32] results in the formation of linear array of spheres having a larger radius than that of the initial semiconducting cylinder, establishing an electrical connection with the adjacent conductive buses. This approach provides a pathway to avoid semiconducting material contamination during prolonged contact at high temperature between conductors and semiconductors at the fiber draw step [19, 45, 46] enabling new fiber architectures and functionalities that were previously unattainable, all electrically connected and fully packaged. These results pave the way to numerous possible fiber based devices such as a fully packaged p-n or p-i-n photodetectors with a "spherical-molecules" configuration-internal to the fiber, addressable through the continuous buses. This approach demonstrated how to achieve novel fiber structures in which components are brought into contact post draw, through the aforementioned selective break-up process.

In the next chapter we will describe a novel approach towards embedding semiconductor devices in thermally drawn fibers. This approach allows to both control the fiber structure axially, as well as to enable previously unattainable functionality in fibers such as light emission or high bandwidth photodetection.

Chapter 3

Communication through machine washable fibers and fabrics

Fibers are a central building block of modern communication systems [60], mostly used as a passive optic conduits for light transmission at high bandwidths. Emergence of multimaterial fibers have enabled some complimentary functionalities such as omnidirectional dielectric mirror fibers [17] to photodetecting fibers [19]. However, to establish an efficient textile communication platform two main cornerstone components are required - light emitting fibers and fibers with high bandwidth photodetection capabilities. Here, we demonstrate the first thermally drawn light emitting fibers, which incorporate high efficiency semiconducting light emitting diodes, packaged with high conductivity metallic electrodes internal to the fiber. The size of the fiber and the linear density of the devices could be easily controlled. Since all components are internal - machine washability is naturally achieved. Moreover, similar strategy was employed to incorporate micron - sized crystalline semiconducting photodetectors, that allows to register optic signals with high bandwidth. These fibers were weaved into fabrics which demonstrated light emitting and photodetecting capabilities. *Intra*fiber optic communication was demonstrated by placing light emitting fibers in front of photodetecting fibers. Additionally, information transfer from a light source to fabric was demonstrated through light source modulation. This technique allows also to form a cladding shape which can both collimate the light emitted

from the fibers and focus an external light signal impingement on the surface of the photodetecting fiber, increasing the communication range. Employing this new technology will potentially bring significant contributions to the electronic textiles field, and transform the way we can communicate by the means of our clothes.

3.1 Introduction and motivation

Fibers are used extensively in several, mostly mutually exclusive fields such as textile and apparel industry or as a central component in telecommunication systems. In both cases, fibers are mostly passive components, with a single desired functionality, whether it is structural, aesthetic or optical. Recently, some great progress has been achieved in convergining textiles, electronics and electrooptics [61, 62]. To build a textile based optical communication system two main components are necessary - textile light emitters and textile photodetectors. To be able to control these properties with high precision and resolution, we desire to enable light emission and photodetection of each fiber separately. Light transmission and emission from a cleaved end or the outer surface of the fiber are both well established technologies, but it requires two separate components - medium for light generation and a medium for light delivery, which are most of the time separate, thus precludes miniaturization required to embed these into textiles [63, 64, 65]. Fiber laser technology suffers from the same drawback - external optical pumping has to be applied for light gain and emission [66]. Recently, several approaches were developed to establish fibers that convert electrical power to light emission. Many of these approaches are based on coating the outer surface of textile fibers with organic, inorganic or electroluminescent light emitting layers by conventional deposition techniques [67, 68, 69, 70, 71]. These techniques focus on applying the active layer on the outer surface of the fiber, thus unfortunately, everyday handling or machine washing will detrimentally affect the fiber performance. Additionally, these devices are limited to small length of the fiber or require an outer, transparent electrode which is by itself not capable to withstand mechanical handling. Some other work has focused on embedding single light emitting devices and separate

conducting layers to an existing fabric or fibers, but this approach is very time and effort consuming, and by itself is not mechanically stable [72, 73, 74]. Regarding the complimentary part of the communication system - fiber based photodetectors - these were developed by several groups [12, 19, 20, 24, 41]. Although these fibers have versatile capabilities such as recording light at various wavelengths or intensity, these are based on amorphous semiconductors which limit the amount or information we are able to transmit using these fibers (i.e. low bandwidth).

In this work we develop and demonstrate a new approach to allow high efficiency light emission and high bandwidth photodetection via thermally drawn fibers. This development allows to achieve novel fiber capabilities such as:

- Enabling light technology in clothes and textiles - new tool for fashion design.
- Building optical *inter* and *intra*-textile light based communication systems, such as LiFi communication system, or clothes that can send and receive data.
- Enable health monitoring of bodily functions such as pulse and blood oxygenation through textiles.

These capabilities become available through embedding electronic and opto-electronic devices internal to the fiber, ensuring that these could be weaved into fabrics and washed - or in other words, withstand everyday use.

3.2 Challenges and approach to resolution

It is extremely challenging to obtain a crystalline light emitting structure in thermally drawn fibers due to fundamental processing problems - we are simultaneously required to draw a large set of materials with disparate thermal properties in close proximity to each other. An illustration of typical structure of blue light emitting diode (LED) is shown in Figure 3-1. Here we can see that the device consists of many thin layers made of thermally dissimilar materials such as $AlGaN$, GaN, SiO_2 and sometimes SiC substrates. These materials are refractory ceramics, i.e. have

very high melting temperature, not suitable to be drawn in silica cladding, since its softening temperature is lower than of the crystalline semiconductors of the LEDs.

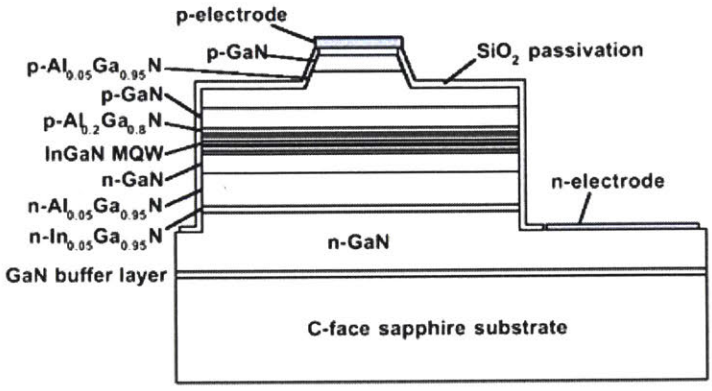

Figure 3-1: **Illustration of typical structure of blue light emitting diode** [75].

An example to a scenario where high melting temperature materials are drawn in a cladding with lower softening point is shown in Figure 3-2(a). Here, a draw of a fiber containing SnPb metal alloy in PC cladding has not been successful, and the results are shown in Figure 3-2(a), where the metal does not melt and is embedded in the deformed cladding. Similar results are obtained for any materials that have dissimilar melting and glass transition temperatures. A possible solution could be raising the temperature at which the draw is performed. Unfortunately, raising the temperature brings into play new problems which prevent achieving the desired structures. Both diffusion and chemical reactions have an exponential dependence on temperature, thus, any draw that is performed at elevated temperature will be subject to these limitations. An example to the fast diffusion and compound formation is shown in Figure 3-2(b), where initially separated materials - Si and Cu, end up totally mixed in the fiber core.

A new approach to achieve such functionality is required. We have realized that there are exceptions to the assumption that all materials have to flow during the draw. For instance, conductive composite materials were shown to be drawn successfully,

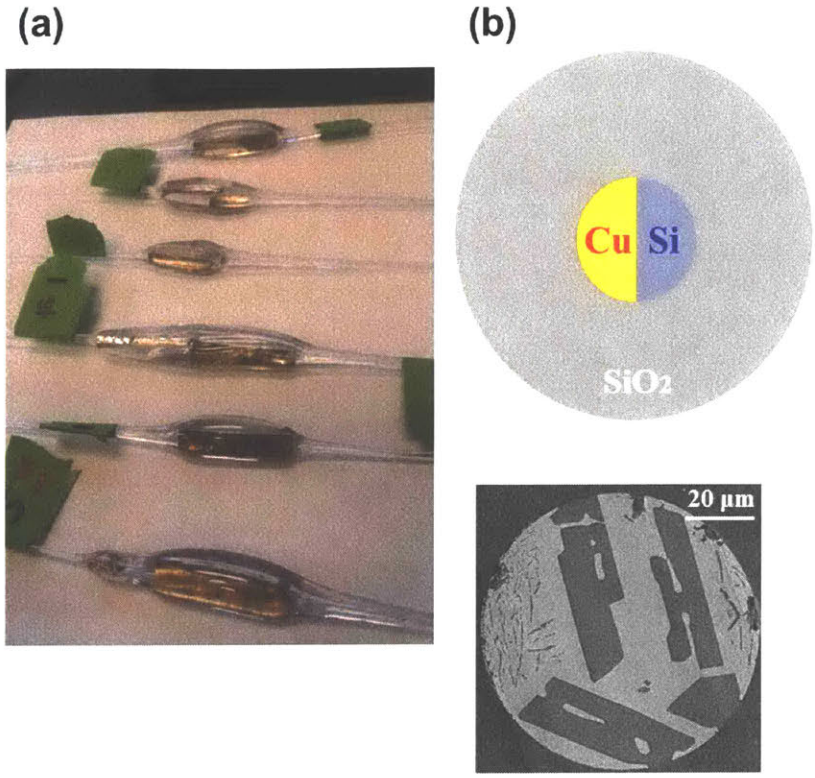

Figure 3-2: **Examples of challenges in thermal draw of multimaterial fibers**. (a) Optical photography of PC clad fibers containing SnPb alloy metal that did not melt during fiber draw and was integrated to the fiber structure without flowing. (b) Example of Cu and Si diffusion that occurs during the draw of multimaterial fibers at elevated temperatures. The top illustration shows the preform structure, prior to draw. The silica preform contains a core made of Si and Cu, with sharp interface between these materials. The bottom electron microscopy micrograph shows the structure of the fiber, post draw. The inner cores are totally mixed, and some phase separation is present, with regions rich in Si or Cu. No sharp interface between Si and Cu exist.

where the conductive components (carbon black particles) do not melt during the draw, but just redistributed during the draw [21, 41]. Similarly, we are interested in designing a system where micron-sized electronic devices are integrated into the preform and drawn into fibers. These devices are very similar to the carbon black particles in polymeric composites we draw, since these do not melt or scaled. The

particles are located in the preform at some desired location in the width of the fiber and are electrically connected to the conductive wires in the fibers. Unlike the carbon black conductive composites, we would like to have a full control of the particle location and orientation in the fiber.

The objectives of this work were:

1. Integrate devices into fibers - the devices do not melt nor extend along the fiber length.
2. Place the diodes in controlled location.
3. Orient the devices in the fibers.
4. Connect to the diode terminals with continuous conductors for current supply.

The main challenges we had to overcome were:

1. The devices do not scale during the draw, but other components do, thus, the contact has to be formed during the draw (not in the preform).
2. High currents are needed - high axial conductivity - continuous, low conductivity, metals are required.

3.3 Preform preparation methods, materials selection and fiber draw

We started with locating miniaturized electronic devices available commercially. The smallest available commercial LEDs found were Cree UT170 SiC substrate GaN / InGaN devices, as shown in Figure 3-3. These devices have a square shape, with a dimensions of 170μm $\times$ 170μm and a thickness of 50μm. The device size will potentially provide a limit to the minimal external size of the fiber.

The benefits of using these devices are their perfected and optimized characteristics, relatively inexpensive price ($\sim$ \$0.1 per device). Embedding of these devices is made possible by use of a thin layer, that we call the "orientation layer", where the

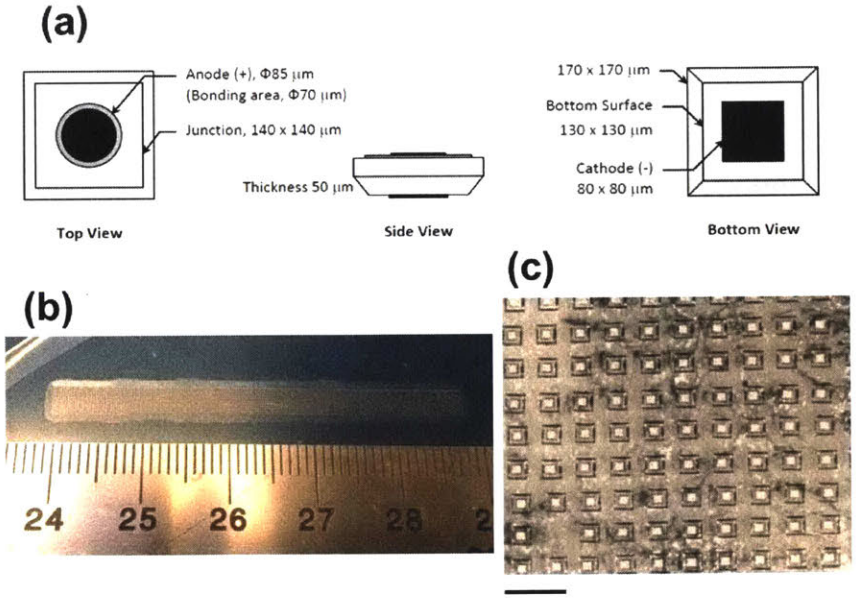

Figure 3-3: **Cree light emitting diodes**. (a) Schematics of the light emitting devices, their main structure and dimensions [76]. (b) Optical photography of the diodes supplied between two carrier films. (c) Optical micrograph of the devices adhered to carrier films, showing the rectangular cathode of the devices. Scale bar - 400μm.

devices are placed and oriented with a desired position. Since the electronic particles do not melt nor extend during the draw, they will deform the soft polymer around them, and possibly cut through some PC layers in the preform / fiber. Thus, the electrical contact between the conductors and the devices cannot form in the preform, but has to be formed during the fiber draw.

3.3.1 Embedding devices in fibers

First, we have developed a process to embed the devices in the preform. We introduce an orientation layer in the middle of the preform, in which we mill pockets that should hold the devices in the preform, as shown in Figure 3-4(a). This figure shows the inner layer with the milled pockets which contain the devices (denoted with blue color in

the figure). Prior to introduction of metals to the preform, this layer was sandwiched between two thick PC slabs, to investigate the location of the devices in the fibers. The resulting fibers are shown in Figures 3-4(b)-(c), where we can locate the devices internal to fibers.

Figure 3-4: **Structure of orientation layer and localization of devices in the fibers**. (a) Illustration of the orientation layer structure. On the surface of the orientation layer some pockets were milled and the devices (blue) placed into these pockets. (b) Optical micrograph that shows the location of the devices in the fiber, top view. Scale bar - 600μm. (c) Optical micrograph of the devices in the fiber, side view. Scale bar - 400μm.

It is apparent that the devices keep their original orientation in the fiber, although some slight planar tilt is present. This tilt most probably occurs during the draw process of the fibers, since these devices were placed in other orientation in the preform.

Since we need to make the connection to the terminals at the top and the bottom of the devices, such a tilt should not preclude formation of the contacts between the wires and the devices. Additionally, we can see that there is a void present at the vicinity of the electronic device. This occurs due to the flow of the particles in the high viscosity PC cladding, which cannot fill all small voids around the devices. These voids are to be closed if liquid metals should be used, although these do not constitute a substantial problem if high melting temperature metals are used in a convergence setting.

3.3.2 Introducing metals - two alternatives

Two main preform structures were considered as potential candidates to obtain the fiber structure - preform with liquid metal as electrodes, and a preform with high melting temperature metals, at a finite wire size - we called the latter process "convergence".

Low melting temperature metals

We have started with embedding low melting temperature metallic alloys that melt during the draw. A process for preparation of such preform is shown in Figure 3-5(a). The process consists of several steps, which are detailed in the figure. The preform with the low melting temperature metal was drawn at different draw temperature and conditions, and some representative results are shown in Figure 3-5(b)-(d). Figure 3-5(b) shows a cross section of a fiber, away from a device, where the two metallic electrodes are clearly seen. These electrodes are separated by a thin PC layer, which prevents formation of shorts between the two electrodes. Figure 3-5(c) shows a top view of a fiber that contains both the diode and the metallic wires. Figure 3-5(d) shows a side view of a fiber with the device and the wires. Unfortunately, the metals do not touch the device contacts. Due to the very low viscosity of the metal, its flow is disturbed in the vicinity of the device. Since the viscosity of the PC is much higher than of the metal, the metal stops flowing in the process of device flow from

the preform to the fiber. The devices push and cut through the PC orientation layer, and the pressure applied to in the process distort the flow of the metal, preventing the metal to reach the contact pads of the devices.

To solve the problem of non existing contact between the metal electrodes and devices, the viscosity of the components had to be altered. Since we have used devices that do not melt or scale down during the draw, we have chose to use wires that do not melt nor scale down during the draw. This allows to use electrodes with infinitely high viscosity. This property of the wires will facilitate incision of the orientation layer to form a contact between the wires and the devices.

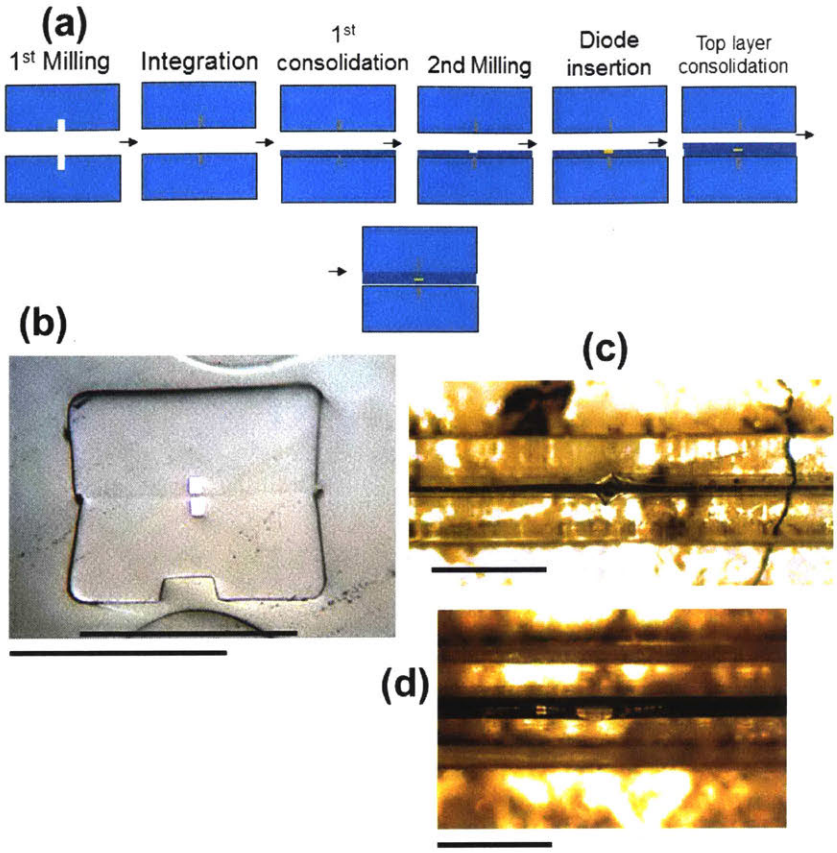

Figure 3-5: **Embedding low melting temperature metals in the preform.** (a) Illustration of the preform preparation method that contains low melting temperature metals. The preform is composed of two main slabs, with a groove milled on its surface to accommodate the metallic pieces which were precut to the desired dimensions. During the second step, the metal bars are inserted to the pockets milled in the PC bars; In the third step, a thin PC layer is consolidated on top of the PC bar with the metal; In the fourth step, the small pockets for the devices are milled in the consolidated thin layer; In the fifth step the diodes are placed into the milled pockets; In the sixth step another thin layer is placed on the devices and consolidated on top of the other thin milled layer; At the last step the top part of the preform is consolidated with the other half to form the final structure. (b) Optical micrograph of the cross section of the drawn fiber that shows the metallic electrodes. No shorts are present away from the devices. Scale bar - 600μm.(c) Optical micrograph of the fiber, top view, that shows both the presence of the metallic electrodes and the LED device. Scale bar - 600μm. (d)Optical micrograph of the fiber, side view, shows both the presence of the metallic electrodes and the LED device. No contact is formed between the devices and the wires. Scale bar - 600μm.

High melting temperature metals

High temperature melting metals are available with long continuous lengths and various, small diameters. To integrate these into the fibers, a modified preform has to be prepared: a preform that could accommodate the wires, integrate them into the fibers and connect the wires to the devices. Figure 3-6(a) shows the structure of the modified preform, where the diodes are still embedded into the orientation layer, but the two main slabs that the preform is made of contain two trenches where the wires are placed during the draw. Figure 3-6(b) shows the placement of the diodes in the milled pockets of the orientation layer. The following is a description of the preform preparation method:

1. Two slabs of dried PC (McMaster Carr #1749K149), width - 1", length - 8" and thickness of 1/2", were milled to introduce a pocket, all preform long with the following dimensions - width - 1.25mm and depth of 1.6mm. The size of the pockets was chosen such that its size is approximately equal to $D = \frac{3\beta d}{4}$, where D is the effective diameter of the pocket in the preform, β is the draw down ratio and d is the diameter of the wires to be embedded in the fibers.

2. Two Teflon bars were inserted into the milled pockets with similar size to prevent pocket collapse during the consolidation.

3. A thin 500μm thickness PC layer was consolidated on one of the PC slabs. The consolidation was done in a hydraulic press, heated to a temperature of 175^oC for 5 minutes and then water cooled.

4. Small pockets were drilled in the thin PC layer. The pockets were round with a diameter of 0.01" and depth of 0.1mm. The distance between the pockets was varied according to the desired density of the devices in the fiber.

5. The diodes were transferred manually to the milled pockets by use of fine tip tweezers. The diodes were oriented in the fiber with a consistent orientation.

6. Another thin layer of 0.5mm thickness was consolidated on top of the diodes and

the other thin film, to hold the diodes in place in the preform. The consolidation process is similar to the previous step.

7. The top PC slab was consolidated on top of the layers to form the full preform. The consolidation was performed in the hot press at a temperature of 175^oC for an hour, and then slowly cooled to room temperature, in air.

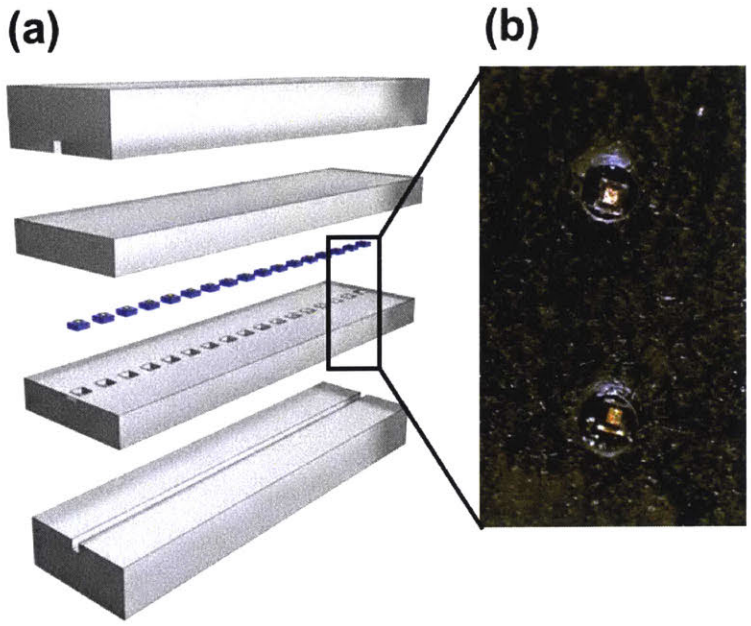

Figure 3-6: **Preform structure**. (a) Illustration of the preform structure. The preform is composed of two main slabs, with a groove milled on its surface to accommodate the wires that will be interfaced with the devices in the fiber, all preform long. The inner layer is the orientation layer, where some pockets were milled and the devices placed into these pockets. A top polymeric layer is placed on top of the orientation layer containing the devices. (b) Optical micrograph that shows the devices placed in the milled pockets of the orientation layer.

The preform with the embedded diodes was placed in the draw tower, the wires were fed into the preform, as shown in Figure 3-7(a).

The wires are embedded into the fiber structure and are continuously fed into the fibers, while the cladding is applying friction on the wires and pulling them during

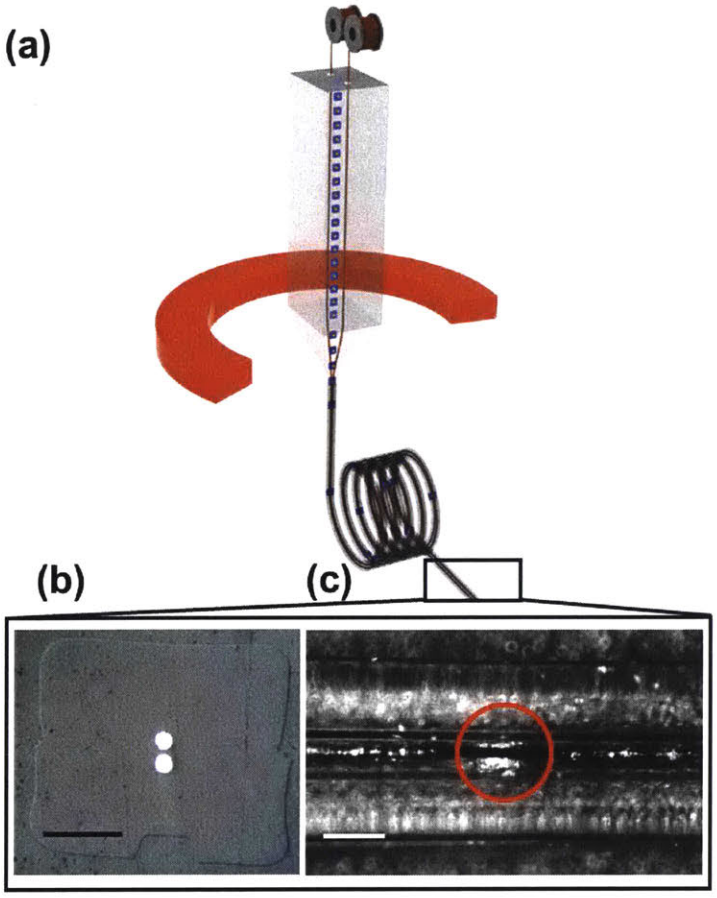

Figure 3-7: **Fiber draw results**. (a) Illustration of the preform draw process. The metallic wires are fed through the preform which is fed through the heated draw tower. These wires are then embedded in the fibers. (b) Optical micrograph of the fiber cross section that shows two W wires well embedded in the fiber cladding, without any gaps and without electrical shorts. Scale bar - 200μm. (c) Optical micrograph of the fiber containing LED device and the wires in contact. Scale bar - 200μm.

the process of the draw. The PC cladding is viscous at the draw temperature, while the devices and the wires are solid. Since the pocket where the devices are placed and the pocket which contain the fed wires are smaller in the fiber than the size of

the devices and the wires, both the wires and the devices cut through the viscous cladding and touch each other to form a intimate contact between the wires and the device. The connection is formed between the device and the wire, nonetheless no contact is formed between the two wires in the fiber. The main parameters that affect the structure in the fiber are the device size, wire size, pocket dimensions and the thickness of the orientation layer. Control over the dimension of each parameters ensures electrical contact to devices, but no electrical short formation between the wires. Multiple wires were able to be embedded into the fibers, among them 50μm diameter tungsten (W) wires (Goodfellow $\#343-809-07$), and 50μm copper (Cu) wires (Goodfellow $\#271-974-11$). The fibers were continuously drawn and spooled. The process of the initial feeding of the wires was achieved by a two step process. First, thicker (34 awg) copper wires were fed through the pockets. Then the preform was mounted on the tower feeder and the small tungsten or copper wires were tied to the to guide the wires and pulled through the pockets and attached to the bate off weight. The furnace was then heated, such that the top zone temperature was set to 150^oC, the middle zone temperature was 270^oC and the bottom zone temperature - 110^oC. Necking of the preform causes these channels to constrict and apply friction on the small wires. When pulling on the fiber with the capstan, the small wires are pulled with the fiber and are eventually embedded in the fiber. The feeding speed was 1mm/min, the draw speed - 1.6mm/min to achieve a draw down ratio of 40. Here, the fiber dimension does not necessarily obey the relationship described by equation 1.1, since we embed solid particles and wires. Naturally, the law of mass conservation is still valid, but the ratio of speeds needs to be corrected to take into account the diameter of the wires which is usually larger than the dimension of the void that accommodates it in the fiber. The temperature of the furnace was not changed during the draw to keep the PC viscosity low enough, to close any voids or gaps in the fiber, by a polymer reflow.

3.4 Results

3.4.1 Light emitting fibers

Operation of fibers with embedded light emitting devices is straightforward. A voltage is applied between the embedded wires, and the LEDs in the fibers light up, as long as the applied voltage is higher than the rated threshold voltage of the device, as shown in Figure 3-8(a)(i). Here we can notice that each diode lights, when the current is supplied. The electric contact is achieved and maintained with time. Increase in the supplied current, increases the intensity of the illumination. The diodes were operated with a current up to 30mA for a single diode, continuously for at least two hours without performance deterioration or thermal damage to the device or the fiber. The device density in the fibers could be controlled by controlling the linear density of the devices in the preform, as demonstrated in Figure 3-8(a) and (b). For a given draw ratio of 40, the fibers contain diodes every $2000 \pm 110mm$ if placed at a linear separation of 1mm in the preform. To increase the device density, it is possible to place them adjacent to each other in the preform as shown in Figure 3-8(b)(ii), which yields a fiber with diodes with a distance of 370 ± 110 from each other. This distance sets a limit on the largest device density of devices in the fiber for a given device size and draw down ratio. To further increase the device density, several approaches could be undertaken. Reduction of the draw down ratio, will yield closer spaced devices, although the fiber dimensions will increase, and this is usually undesirable. Decreasing the size of the devices, will potentially increase their density in the fiber, but this is not easily achievable, since smaller devices are currently commercially unavailable and interfacing these with wires is challenging, since smaller wires need to be used. An alternative approach exists - the devices could be placed in several layers in the preform, as shown in Figure 3-8(c)(i). In this particular case the diodes are placed one on top of the other, requiring to introduce a third wire in the fiber. The device density could also be increased by placing the devices horizontally to each other, but in this case, a fourth wire has to be added. The fiber shown in Figure 3-8(c)(i) was drawn similarly to previous fibers, but now could accommodate two device layers and a third

metallic wire, with the same draw ratio of 40. The resulting fiber is shown in Figure 3-8(c)(ii) and (iii). The distance between the devices was found to be 173 ± 93mm. The devices in the fiber were not perfectly placed on top of each other, and were dispersed homogeneously along the fiber length with a relatively large distribution. The reason the particles do not appear parallel to each other in the fiber could be explained by the nature of fiber draw - small distances in the preform extend considerably during the draw. Placing the diodes with slight mismatch between the layers, or even a slight tilt of the preform during the draw will amplify these mismatches, extending the distances between the devices and effectively homogenizing the distances between the devices in the fiber, thus increasing the density of the devices by a factor of 2 relative to a single layer of devices.

This technique is not necessarily limited to blue color (460nm) InGaN LEDs, as other light emitting devices were successfully embedded in the fibers and similar results were obtained for green color (520nm) InGaN LEDs and red color (625nm) AlGaInP devices, as shown in Figure 3-8(d)(i) and (ii) respectively.

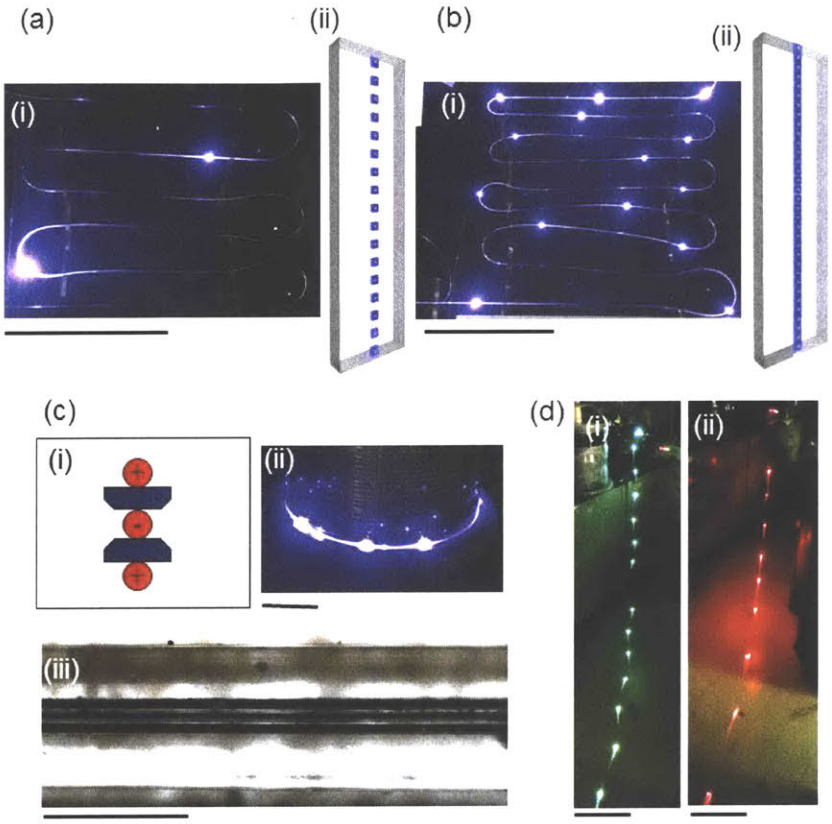

Figure 3-8: **Light emitting fiber results**. (a) Low density of devices in the fiber. (i)Photograph of the light emitting fibers containing blue color light emitting diodes, where the devices appear every 2000 ± 110mm. Scale bar - 50cm. (ii) Illustration of the density of the devices in the orientation layer, placed with a separation of 1mm in the preform. (b) Higher density of devices in the fiber. (i) Photograph of the light emitting fibers containing blue color light emitting diodes, where the devices appear every 370 ± 110mm. This is the maximum linear density available with the given draw down ratio (40), preform structure and device size. Scale bar - 50cm. (ii) Illustration of the maximal linear density of devices in the preform - the devices are placed side by side to each other. (c) Approach to increase the device density in the fibers - the devices could be placed in several layers. (i) The device layers are placed vertically to each other with a common electrode to reduce the number of wires in the fiber. (ii) Photography of the fibers that are made with the structure presented in (i). The devices appear at a distance of 173 ± 93mm in the fibers, approximately half of the distance in a single layer structure. Scale bar - 15cm.(iii) Optical micrograph of the fiber containing three W wires. Scale bar - 600μm.(d) Fibers containing diodes of multiple color. (i) Green color LEDs InGaN diode fibers. Scale bar - 40cm. (ii) Red color InGaAs LEDs integrated to fibers. Scale bar - 40cm.

3.4.2 High bandwidth photodetection

This newly developed technique to embed microelectronic devices in fubers is not limited to just light emission - other electronic devices could be embedded into thermally drawn fibers in a similar fashion. We have embedded P-I-N photodetectors in to the fibers to enable high bandwidth photodetection, in contrast to amorphous chalcogenide materials [12, 19, 20, 24, 41], which have much lower responsivity and bandwidth compared to crystalline semiconductors such as Si, Ge or GaAs. These chalcogenide materials, have high response times, which limit the ability to transmit large amount of information in a given period of time. Introduction of crystalline GaAs semiconducting P-I-N photodiodes is demonstrated in Figure 3-9.

Here the contact to the devices is established on the same side of the detectors, keeping the aperture of the devices uncovered by the the wires, while a third wire is placed behind the devices to prevent them from tilting during the fiber draw. The preform is prepared similarly to previously described LED preform, with a few slight modifications as described in the following steps:

- Step 1 - Two pockets were milled in one of the PC slabs. The dimensions of the pockets were kept the same, while the distance between the pocket centers was 5mm.

- Step 3 and Step 6 - The layer thickness was changed to 1.5mm.

- Step 4 - The size of the pockets was changed to $400 \times 400\mu$m to accommodate the larger device dimensions. The pocket thickness was changed to 200μm to accommodate larger thickness of the devices.

- Step 5 - The orientation of the devices was in both the vertical and the horizontal directions, to ensure that the two contact pads of the devices are facing the two wires and the anode of each device is connected to the same wire.

Characterization of the GaAs photodetecting fibers was carried out by using fibers that contained red LEDs. The fibers were placed in front of each other, and the voltage along the photodetecting fiber was sweeped, while measuring the resulting

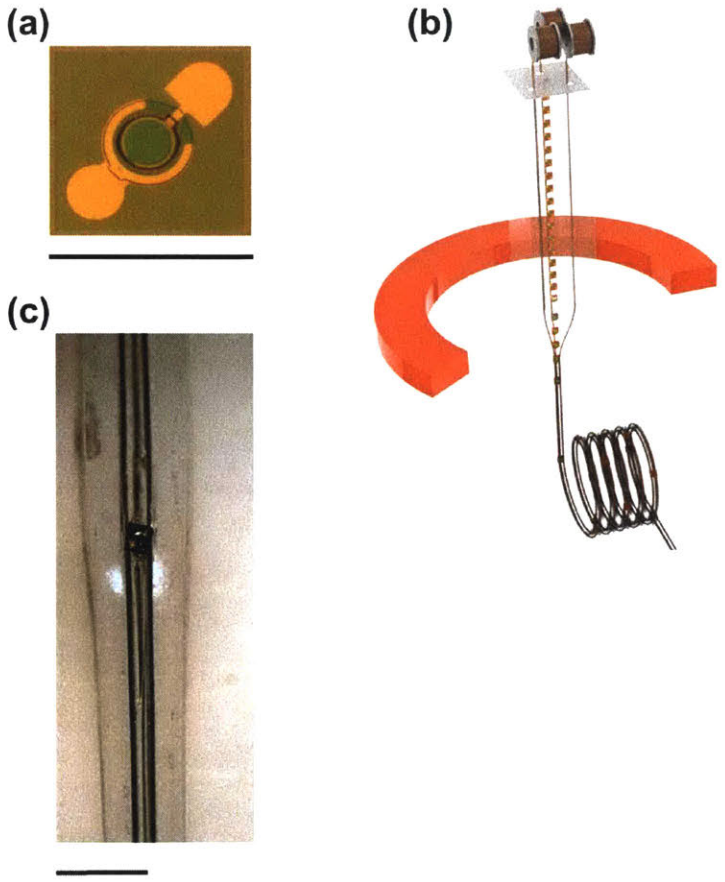

Figure 3-9: **High bandwidth photodetecting fiber draw**. (a) GaAs photodetecting device element. The central part is the device aperture, surrounded by two metallic contacts. Scale bar - 275μm. (b) Illustration of the preform draw process, and the location of the wires in the preform and the fibers. (c) Optical micrography of the photodetecting fibers, showing the device embedded in the fiber. Scale bar - 600μm.

current, to obtain the IV response of the fiber device. Figure 3-10(a) show a clear rectifying behavior.

When a reverse bias was applied on the devices, it was possible to record a substantial increase (4 orders of magnitude) in the the current when the photodetecting fiber was illuminated by the red LED fiber, relative to the dark current. The bandwidth of the photodetecting fibers was measured by illuminating a 30cm long fiber that contained a single device, with a red fiber coupled LED laser (Throlabs LPM-660-SMA)

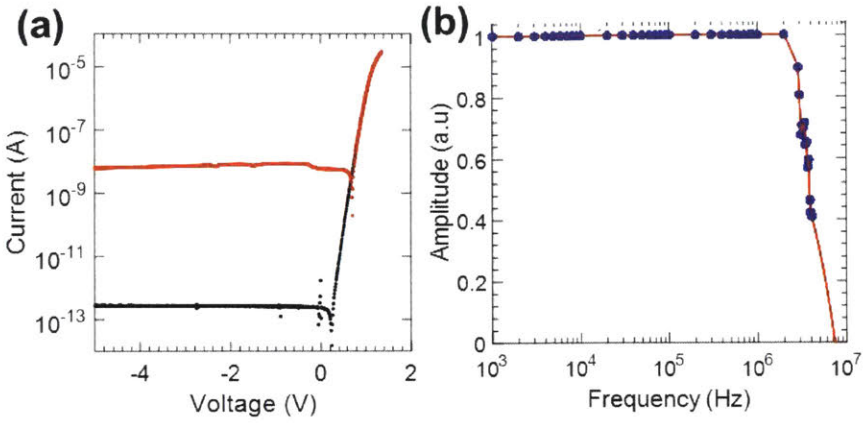

Figure 3-10: **Characterization of the photodetecting fibers**. (a) Current vs. voltage curve (IV) of a fiber containing one GaAs device showing a clear rectifying behavior. The black curve is obtained under dark, while the red curve is obtained under illumination. In the reverse bias regime (negative voltage) the current increases by a few orders of magnitude. (b) Bandwidth measurement of the photodetecting fiber - the 3dB bandwidth achieved is around 3MHz.

that was connected to a square wave function generator (Tektronix AFG3252). The fiber was connected to a transimpedance amplifier (Thorlabs TIA60) and an oscilloscope (Agilent Technologies DSO-X 3014A). The resulting amplitude was measured as the modulation frequency was increasing. The result of the fiber bandwidth measurement is shown in Figure 3-10(b), where the 3dB bandwidth, (a decrease in the amplitude to a value of 0.708), is around 3MHz. This value is a few orders of magnitude higher than any measured bandwidth of chalcogenide photodetecting fibers. The bandwidth of this system is a linear function of the desired gain set by the amplifier, and could be increased if lower gain could suffice, or alternatively a stronger or more collimated emitters used. These results present the first realization of fibers with high bandwidth photodetection, and allow to demonstrate optical transmission of a high amount of information in a given time.

It is important to note that the embedded wires have a finite resistance, which is not negligible. This limits the length of the fiber at which the light emitting diodes could be operated. The devices have a finite resistance, and these are connected in parallel to each other. The power dissipates on the resistive wires, decreasing the

effective voltage as the length of the wires increase. Consequently, the intensity of the illumination will decrease with distance until the threshold voltage is reached. Beyond that point along the fiber length, no light will be emitted. To operate as many devices as possible, a few approaches could be explored, as described here:

1. Use wires with maximal conductivity. Copper is a material with very high electrical conductivity. In this work we have demonstrated an ability to integrate 50μm diameter copper wires into fibers. The drawback of using copper wires is their low strength, which may break during the fiber draw process, additional to a more complex wire exposure procedure to make connections to the fiber.

2. Increasing the wire diameter. The resistance scales as $\propto 1/d^2$, thus increasing the diameter by a factor of 2 will decrease the resistance by a factor of 4. The drawback of this approach is blockage of the light by thicker wires.

3. Reducing the distance between the devices will allow to operate more devices, but this approach will not extend the length of operable fiber.

For the photodetecting fibers, this is less of an issue, since relatively low currents are present when operating the devices.

3.4.3 From fibers to fabric

Since all components of the fibers are internal to the fiber structure, these could easily withstand the strains and stresses of textile manufacturing techniques such as weaving, or day to day handling such as washing the fibers and fabrics in a washing machine. To demonstrate this process, both LED and photodetecting continuous fibers were weaved into a separate textile polyester fabric in a satin weave pattern, as shown in Figure 3-11(a) and (b). The weaving process was performed by Marty Ellis at Inman Mills, Inman, SC. Both fibers containing LEDs or photodetectors withstood the weaving process and were fully operable following establishing connection with each fiber, at the fabric edge. Additionally, these fibers were fully immersed into

a water tank (with the electrical connections) and were fully operable, as shown in Figure 3-11(c).

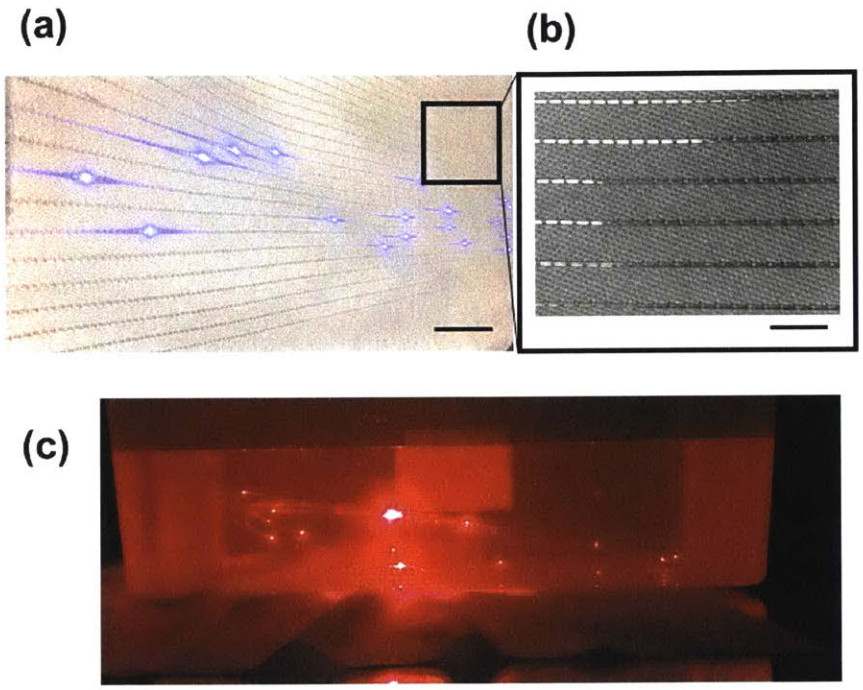

Figure 3-11: **Light emitting and photodetecting fibers embedded into a fabric**. (a) Blue color light emitting fibers are embedded into a fabric and are operated. Scale bar - 30cm (b) Closer look at the fiber / fabric interface. Scale bar - 1cm. (c) Photography of water exposure of the fibers and the connections. The fibers are operable under water.

Machine washing experiments were performed as well - the fibers were placed in a protective sack and washed 10 times in a household washing machine, as shown in Figure 3-12. The fibers had identical performance as prior to the execution of the washing cycle test.

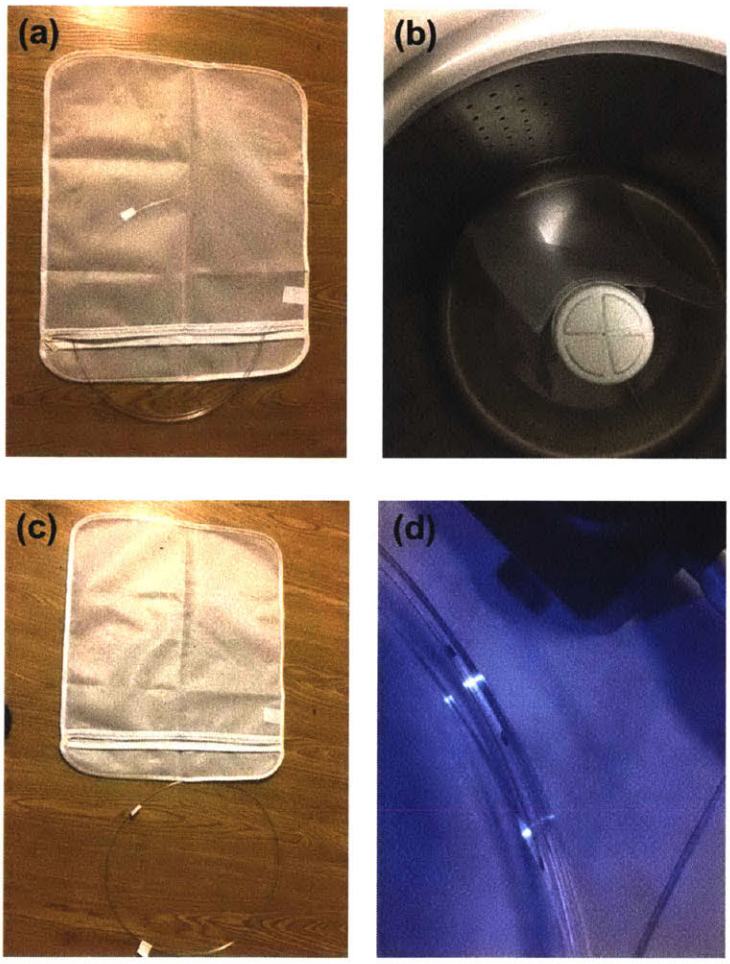

Figure 3-12: **Machine washing experiments with light emitting fibers**. (a) Light emitting fiber bunch is placed in a protective sack. (b) The protective sack with the fibers is placed in a household washing machine. (c) Fibers and sack after a washing cycle. (d) Fiber operation - light emission after the washing cycle.

3.4.4 Fiber and fabric communication system

Development of light emitting and high bandwidth photodetecting fibers allows to realize fiber and fabric communication system. A set of photodetecting fibers could be used to record illumination by a set of light emitting fibers weaved into another fabric or alternatively by an external light source, to realize fabric to fabric communication or alternatively LiFi to fabric communications setups. AFFOA engineers have realized a demonstrator of the fiber photodetection capability by integrating the photodetecting fibers into a baseball cap, as shown in Figure 3-13.

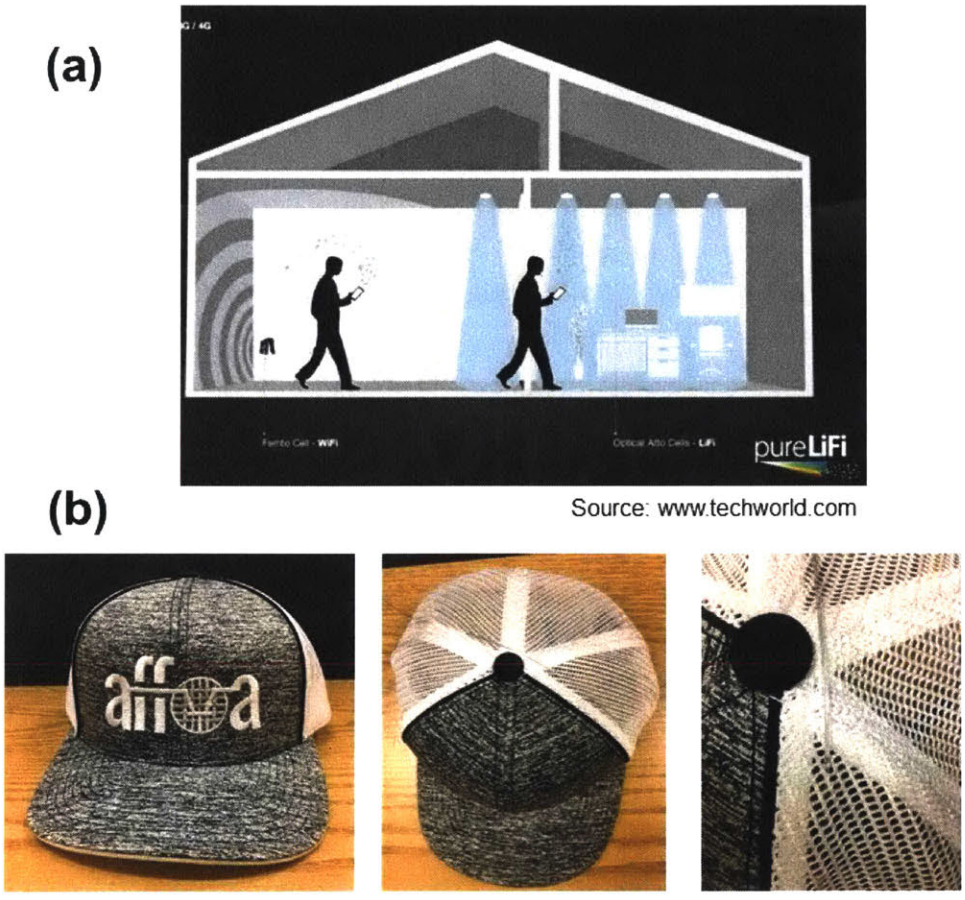

Figure 3-13: **LiFi system concept**. (a) Illustration of the traditional LiFi system. The lights are modulated to transmit data to an electronic device, in this particular example, the information is transmitted to a phone. (b) The cap designed by AFFOA team, where the photodetecting fiber was embedded in the net of the hat.

In this demonsration, an expernal LED module was modulated by an external circuit, driving the light amplitude to transmit audio signals. When the wearer of the hat was standing under the LED source, the photodetecting fiber received the optical signal and converted it to an electric current. The fiber was connected to an electronic circuit which transformed this current to a voltage and drived earphones that were connected to the circuit. This technology was demonstrated during the grand opening of AFFOA center and was featured in a few major mass media outlets [77, 78, 79, 80, 81, 82, 83].

3.4.5 Communication range and approach to increase this distance

An experiment was carried out to determine the dependence of the communication range between a light emitting fiber and a photodetecting fiber on the distance between the two fiber devices, as shown in Figure 3-14. In this experiment, the distance between a light emitting and a photodetecting fiber was increased while recording the current of the photodetecting fiber. A constant voltage of 3V and a current of 20mA was supplied to the light emitting fiber, while the photodetecting fiber was connected to a Keithley 6517A low current measurement setup. As can be seen in Figure 3-14(c), $I \propto 1/d^2$, where I is the current and d is the distance. This decay is substantial, and any signal below 0.1nA is comparable with the ambient background noise in the experiment environment. This allowed to establish a communication between the two fibers for a distances up to $\sim$1cm with the above mentioned measuring setup. To increase the range, a few approaches could be undertaken.
The communication range depends on several factors as following:

1. Distance between the emitter and the detector. The intensity is usually inversely proportional to the distance squared.

2. Emitter size, intensity and beam divergence.

3. Receiver aperture size and photoelectric responsivity.

4. The electronic circuitry used to measure the current output from the fibers.

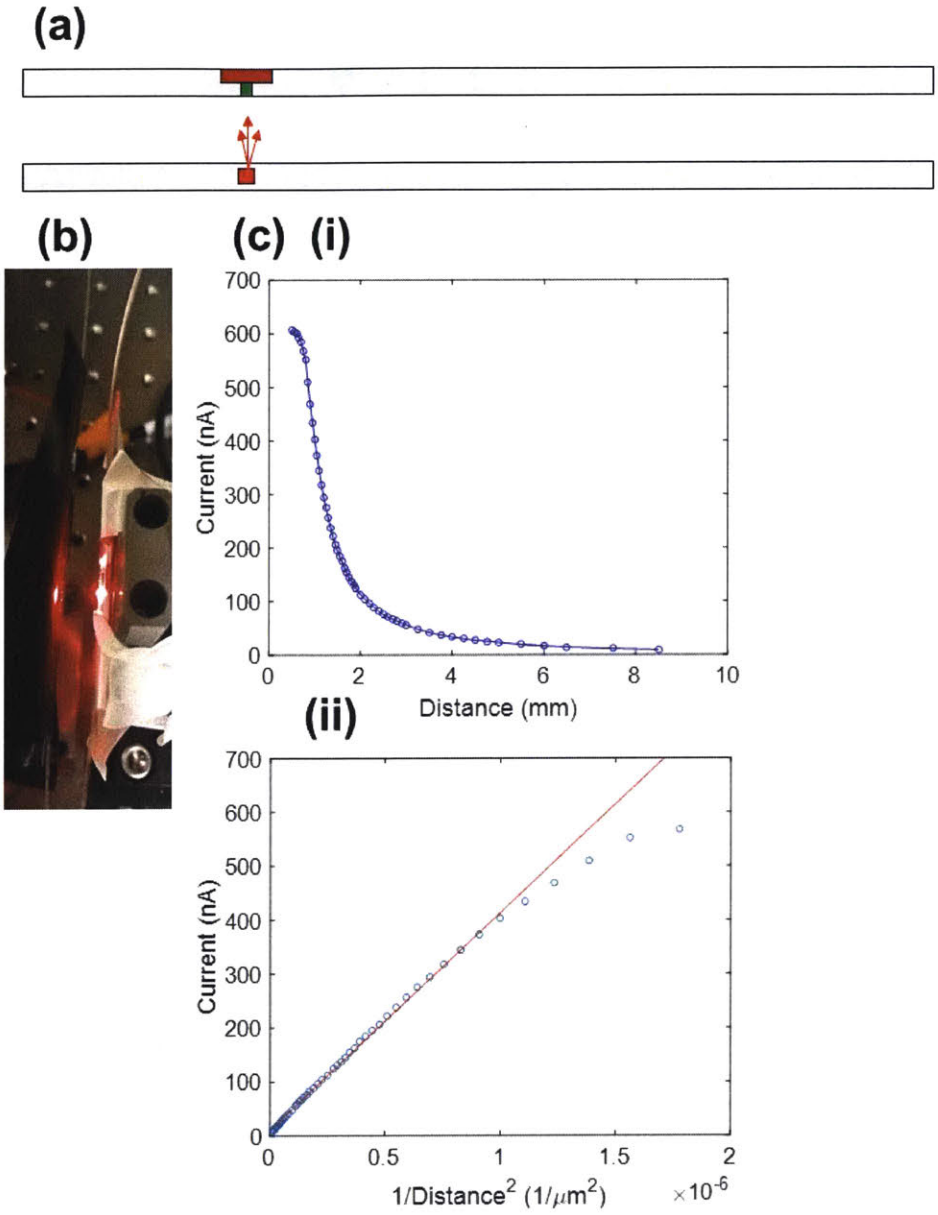

Figure 3-14: **Intensity decay of the communication system with distance.** (a) Illustration of the experimental setup, a light emitting fiber with a red LED is placed in front and aligned with a GaAs photodetecting fiber. The fibers are moved away from each other. (b) Photography of the experimental setup with the LED fiber operated. (c) (i) Registered current by the photodetecting fiber versus distance between the photodetecting fiber and the light emitting fiber. (ii) Current vs. inverse distance squared. Shows a linear dependence between the current and the inverse distance squared.

Several approaches could be undertaken to increase the communication distance. Emitter properties could be chosen to deliver higher illumination intensity or to decrease the divergence of the sources. Unfortunately larger device size, means larger fiber size, and this is much less desired, since it makes the fiber more stiff, complicating the weaving or knitting process. Increasing the intensity of the illumination introduces another drawback - the device efficiency or yield. Higher illumination intensities lead to higher heat density that the device emits, causing it to heat to elevated temperatures, and eventually melting the fiber cladding that encapsulates it. A viable approach is to embed laser diodes, which have a lower beam divergence. This route will be explored in the future. Similarly, the receiver aperture could be enlarged to increase the gain, but this will usually come on the expense of the device size and the fiber size. The electrical circuitry connected to the photodetecting fiber will also influence the communication range. Higher gain will increase the range, on the expense of noise amplification and bandwidth. To achieve high gain, we usually need to include high resistance components in the electrical circuit. The circuit response time, which depends on the resistance and the capacitance of the components, will be much higher, thus, negatively influencing the bandwidth of the system. Alternatively, to increase the range of communication, the external shape of the fiber cladding could be optimized to collimate the light emitted from the light emitting fiber and to focus the light into the photodetecting fiber. Ray optics, 2D numerical simulations were carried out to determine the optimal location of the devices in the fiber and the optimal shape of the cladding, to achieve maximal signal intensity.

Figure 3-15 shows a simulation performed for the experiments shown earlier (Figure 3-14). The fibers were assumed to be square, with a size of $500 \times 500\mu$m. One fiber contained a photodetector (red rectangle, of size 250μm) and the other fiber contains a point source which emulated the LED. This point source emits light in a hemisphere configuration. The simulation was carried out using COMSOL software, Ray tracing module. Figure 3-15 shows the simulation results where the intensity of the illumination was plotted with distance between the fibers. The simulation showed similar results to the experimentally measured current decay with distance. This simulation

was used to determine an optimal device location in the fiber and the optimal fiber shape.

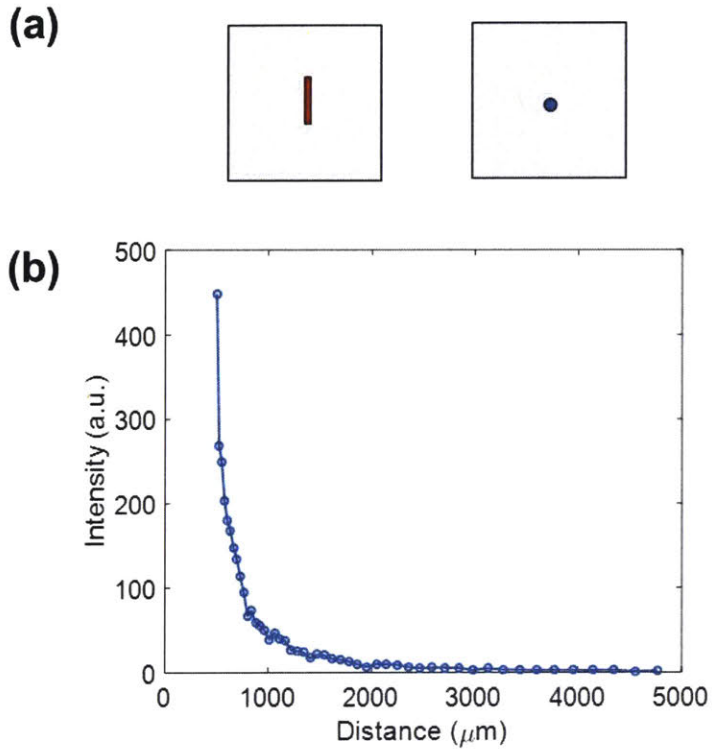

Figure 3-15: **Simulation results of intensity decay with distance - no lens.** (a) Illustration of the simulation design. Red rectangle - photodetector, blue round dot - light emitting diode - point source; gray - PC cladding. (b) Simulation results that show illumination intensity decay with distance between fibers, inversely proportional to distance squared.

Adding a curved structure to the fiber surface and placing the device in the focal point of this lens is an effective approach to collimate and focus the light between the lighht emitting and photodetecting fibers. A similar approach was demonstrated for a photo-voltaic fiber system reported here [84].

Based on lens physics, we should aim to place the devices in the focal point of the lens to both focus an external light source and to collimate the light emitted from the LEDs in the fiber. For a thick lens, the focal distance is given by the Len's maker

equation [85], which is given here by equation 3.1:

$$\frac{1}{f} = (n-1)\left(\frac{1}{R_1} - \frac{1}{R_2} + \frac{(n-1)t}{nR_1R_2}\right) \tag{3.1}$$

Here, f is the focal length of the lens, n is the refractive index of the material the lens is made of, R_1 and R_2 are the radii of curvature of the two spherical parts of the lens and t is the lens thickness. Since the devices are embedded in the cladding, we will have a curved surface only on the external side of the fiber, while the other side is flat, i.e. with infinite radius. Thus, the focal point of such a lens will be as given by equation 3.2.

$$\frac{1}{f} = \frac{n-1}{R_1} \tag{3.2}$$

The cladding of the fibers is made of PC, where its index of refraction is around $n = 1.58$ at the visible wavelength domain. This locates the focal point of the fiber at a distance of $1.72R_1$, and defines the desired fiber structure, as shown in Figure 3-16(a). Here we can see that the optimal structure is a rectangular or square fiber, with the device located approximately 190μm from the square center. The square was assumed to have a size of 500μm, and the lens diameter was equal to the square side length. We have performed a ray optics simulation to find the optimal location of the device in the fiber, and the ray tracing results are shown in Figure 3-16(b). In this figure, we can see that the some of the light is collimated by the lens, while some light is reflected or not collected by the lens and is allowed to escape the fiber without collimation. Other focusing techniques were considered, for example, by using mirrors or multiple lenses on the surface of the fiber. Unfortunately, these geometries are harder to achieve in a fiber form factor, and could be explored in the future.

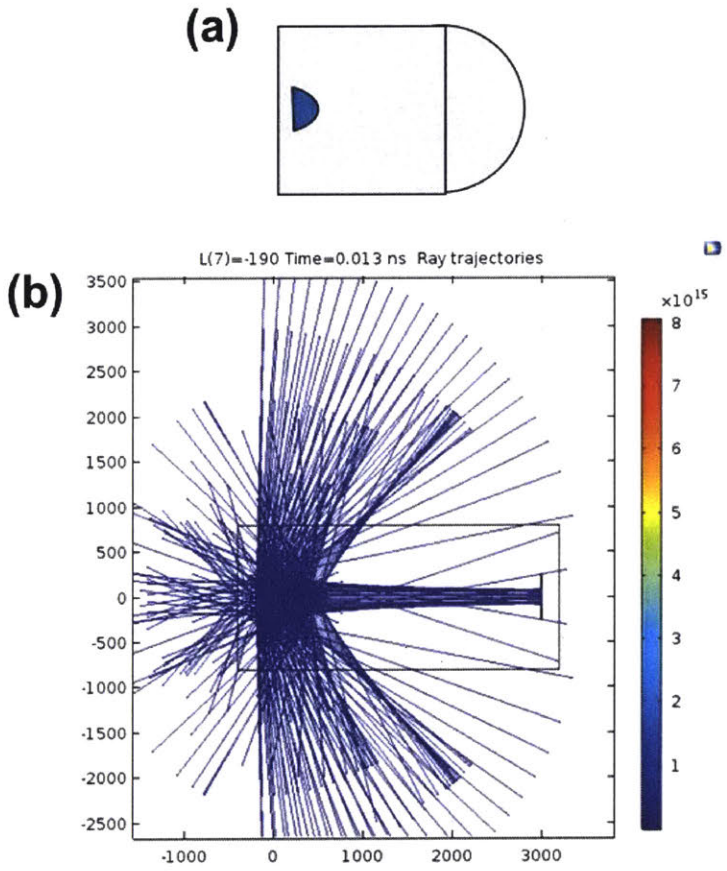

Figure 3-16: **Simulation of light emitting fibers structure - with lens.** (a) Illustration of the fiber structure. Blue hemisphere - light emitting diode; gray - PC cladding. Fiber size - 500 × 500μm. (b) Results of the ray optics simulations that shows collimation of the light at an external source, when the device is placed 190μm form the center of the origin which is the fiber main square body.

Similar approach was carried out to find the optimal device location and fiber shape for focusing a collimated beam of light to the photodetector. Figure 3-17 shows the simulation carried out to determine the optimal location of the device in the fiber to collect the light external to the fiber. Figure 3-17(a) shows the structure of the fiber, Figure 3-17(b)-(c) show the results of the ray tracing simulation and the dependence of the intensity as a function of the location of the device in the fiber. The optimum location of the device in the fiber is 190μm from the center of the origin which is located in the center of the fiber main square body.

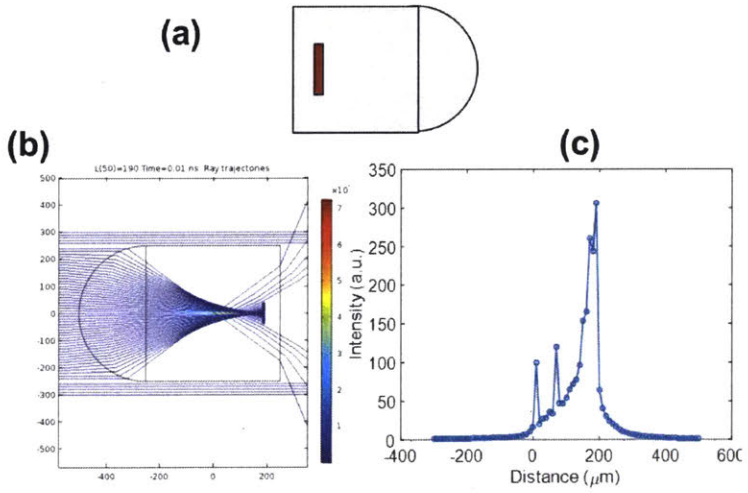

Figure 3-17: **Simulation of photodetecting fibers structure - with lens**. (a) Illustration of the fiber structure. Red square - photodetector; gray - PC cladding. Fiber size - $500 \times 500\mu$m. (b) Results of the ray optics simulations that shows focusing of the collimated external light on the photodetecting device, when the device is placed 190μm form the center of the origin which is the fiber main square body. (c) Intensity of the illumination as a function of location of the device in the fiber. The maximal intensity is at 190μm from the center of the fiber.

We have carried out a similar simulation for both fibers one in front of the other, as shown by Figure 3-18. We can see that adding the lenses on both fibers, collimates and focuses some of the light, which will potentially extended the communication distance.

We have reduced the optimized fiber structure to practice. Figure 3-19(a) shows

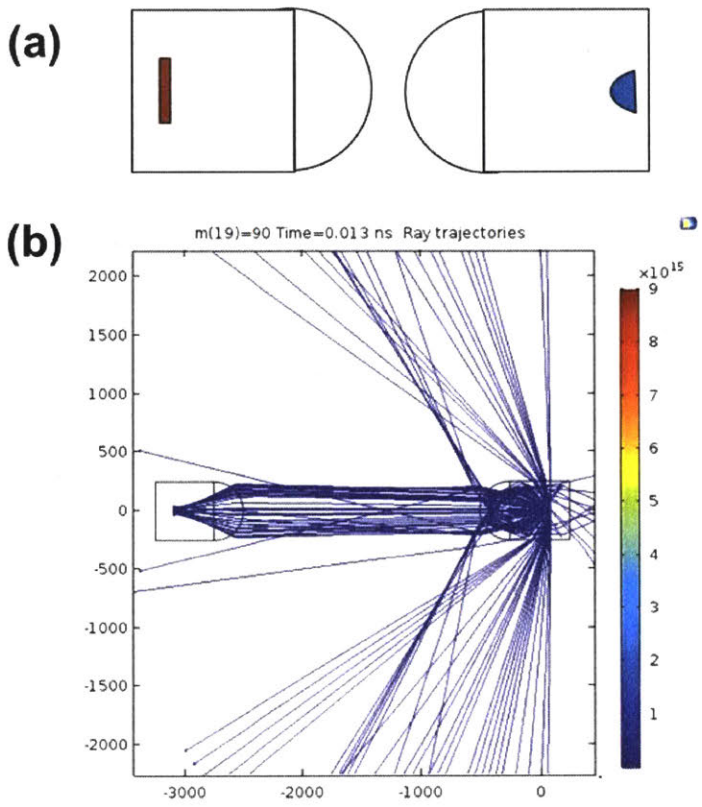

Figure 3-18: **Simulation of a lensed communication system - light emitting and photodetecting fiber structure**. (a) Illustration of the fiber structure. Red square - photodetector; Blue hemisphere - Light emitting device; gray - PC cladding. Fiber size - 500 × 500μm. (b) Results of the ray optics simulations that shows collimation of the emitted light and focusing of the light on the photodetecting device, when the devices are placed 190μm form the center of the origin which is the fiber main square body.

a photography of the preform containing LED devices and a half cylindrical lens attached to the surface of the preform, while Figure 3-19(b) shows the drawn fiber containing the lens and two wires that are connected to the embedded LEDs in the fiber. Figure 3-19(c) shows the LED operation in the fiber with the lens. An experiment was carried out to measure how the presence of the lenses on the fibers were changing the communication range. The fibers were placed in front of each other, such that the LED in the fiber was aligned with the photodetector at the other

fiber, as shown in Figure 3-19(d).

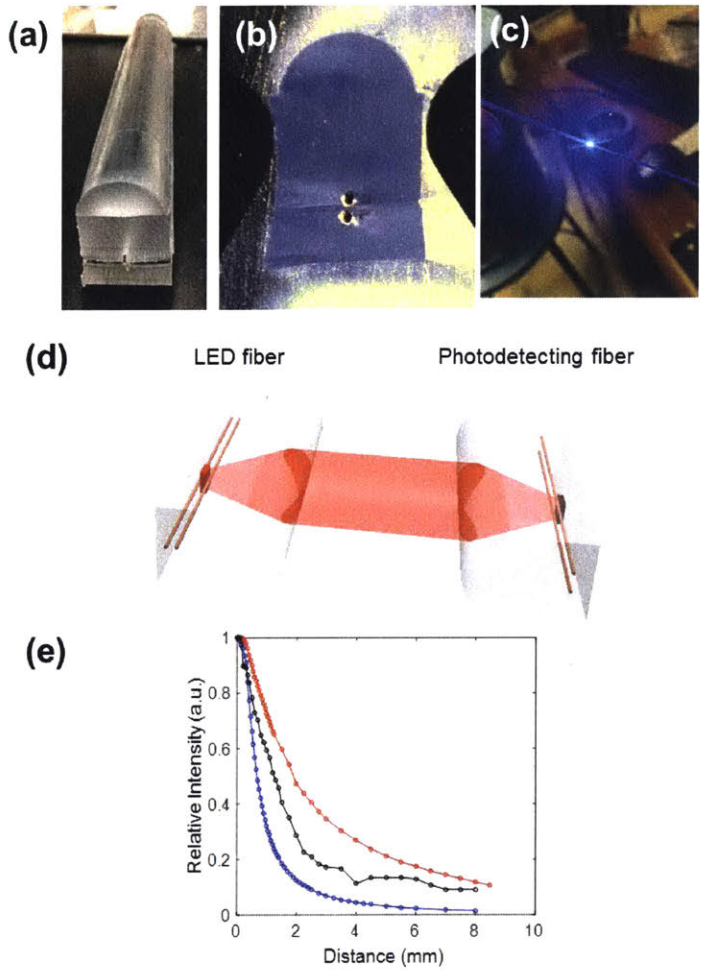

Figure 3-19: **Communication between two lensed fibers.** (a) Photography of the light emitting fiber preform, with a half cylindrical lens attached to the surface of the prefrom. (b) Optical micrograph of the drawn fiber, showing the lens and the two W wires embedded in the cladding. (c) Photography of lensed fiber operation, lens side. (d) Illustration of the fiber communication system structure. Left fiber - light emitting fiber, right fiber - photodetecting fiber. (e) Experimental results - normalized recorded current in the photodetecting fiber as a function of distance between fibers. Blue curve - no collimation nor focusing; Black curve - Light emission collimation, no light focusing on the photodiode; Red curve - Light emission collimation, light focusing on the photodiode.

The distance between the fibers, measured between the two half cylindrical lenses

was varied while the illumination intensity was measured and referenced relative to the recorded intensity at contact. The light emitting device was a red LED which was operated at a voltage of 3V and current of 20mA. The photodetecting device was GaAs p-i-n diode. Since the location of the devices is different in every case (square fibers vs. lensed fibers) the curves were offset by the corresponding distance in order to obtain the same distance between the devices for all cases. Figure 3-19(b) shows the measurement of the relative intensity vs. the distance between the fibers. The results show that the illumination emitted out of the square fibers (blue curve) decays with distance, and the decay is inversely proportional to the distance squared, as expected for a decay from a point source. Shaping the cladding with a lens, for both the emitting and detecting fibers, increases the relative measured current at a given distance, effectively extending the communication range by a factor of 10. The next step of this work will be to integrate these fibers into textiles for fabric to fabric communication setup.

3.5 Discussion and conclusions

In this work, we have demonstrated an alternative strategy for integrating active devices into fibers. Rather than addressing all the challenges of thermal drawing, we have developed a method to directly integrate commercial functional devices (LEDs, photodetectors etc.) into fibers during the thermal drawing process. We package these devices internal to the fibers in high density and integrate them with conductive buses, during the thermal draw. This approach enables to combine the benefits of several technologies - high efficiency devices integrated into kilometer long fibers, which could be weaved into highly functional fabrics. Endowing fibers with active devices will potentially establish a new generation of multifunctional fibers, with highly desired electronic properties. For example, flexible and resilient light emitting fibers could be integrated into textiles to enable covert, optical signal transmission from the soldier uniform to the external world, or high bandwidth photodetectors could be embedded into garments to allow high volume information reception via LiFi (WiFi through

light).

THIS PAGE INTENTIONALLY LEFT BLANK

Chapter 4

Semiconductor, insulator, metal, multifunctional (SIMM) fibers for multianalyte explosives sensing

This chapter was written partially by the author in collaboration with William McDaniel from FLIR corp.

4.1 Introduction and objectives

Semiconductor-insulator-metal multifunctional (SIMM) fibers represent a novel platform for explosives detection by incorporation of wave guiding, heating, and photo detection capabilities directly into the sensing element. Leveraging FLIR's advanced sensing materials in SIMM fibers [86] will enable trace-level detection of explosives and their precursors under field conditions using an extremely compact device. The bulk and expense of typical explosive detectors preclude them from being widely deployed to detect threats such as improvised explosive devices (IEDs) [12]. Reductions in instrument size, weight, and power (SWaP) facilitated by this new platform will ultimately allow every soldier to carry a pocket-size trace explosives detector, increasing troop safety without increasing the weight burden on the dismounted soldier. The objective of this effort was to develop an integrated fiber based sensor platform for

the detection of a wide range of improvised explosive device (IED) constituents including Trinitrotoluene (TNT), Cyclotrimethylenetrinitramine (RDX), Pentaerythritol tetranitrate (PETN), and triacetone triperoxide (TATP). The sensing elements of the device were to be semiconductor - insulator - metal multifunctional (SIMM) fibers coated internally with novel transduction materials that exhibit exquisite sensitivity to explosives, developed by FLIR. The fibers were to contain photodetection elements as integral parts of the fiber, eliminating the need for a separate photodetector and thereby simplifying the device design and cost. The fiber - based sensors would engender unprecedented sensitivities derived from FLIR's emissive detection materials while enabling fabrication of a more versatile, agile instrument. This effort was to ultimately yield a first-generation SIMM fiber-based prototype device offering trace detection capabilities with reduced logistical burden. We specifically aimed to:

1. Design SIMM fiber architectures incorporating waveguiding, heating, and photodetection capabilities.

2. Fabricate more robust SIMM fibers exhibiting reduced environmental and vibration sensitivity.

4.2 Results

4.2.1 Fiber design

A new SIMM fiber design was proposed. To increase the detection ability of explosive substances by the fibers, the internal core material was found to be fluorescent and had to be changed from polymer to glass to eliminate background fluorescence that could mask the signal received from the reaction between the fluorescent dye and the detected explosive. Additionally, several joule heaters were to be incorporated into the fiber structure such that the inner core of the fiber could be heated to enhance analyte transfer through the fiber and to desorb the sample after detection. Two photodetecting schemes were proposed - the first was based on distributed photodetectors made from selenium. An alternative approach was to incorporate semiconducting lo-

calized photodetectors with higher responsivities to detect small optical signals, which were reported upon in Chapter 3. Figure 4-1 summarizes the structures of the two alternative fiber architectures.

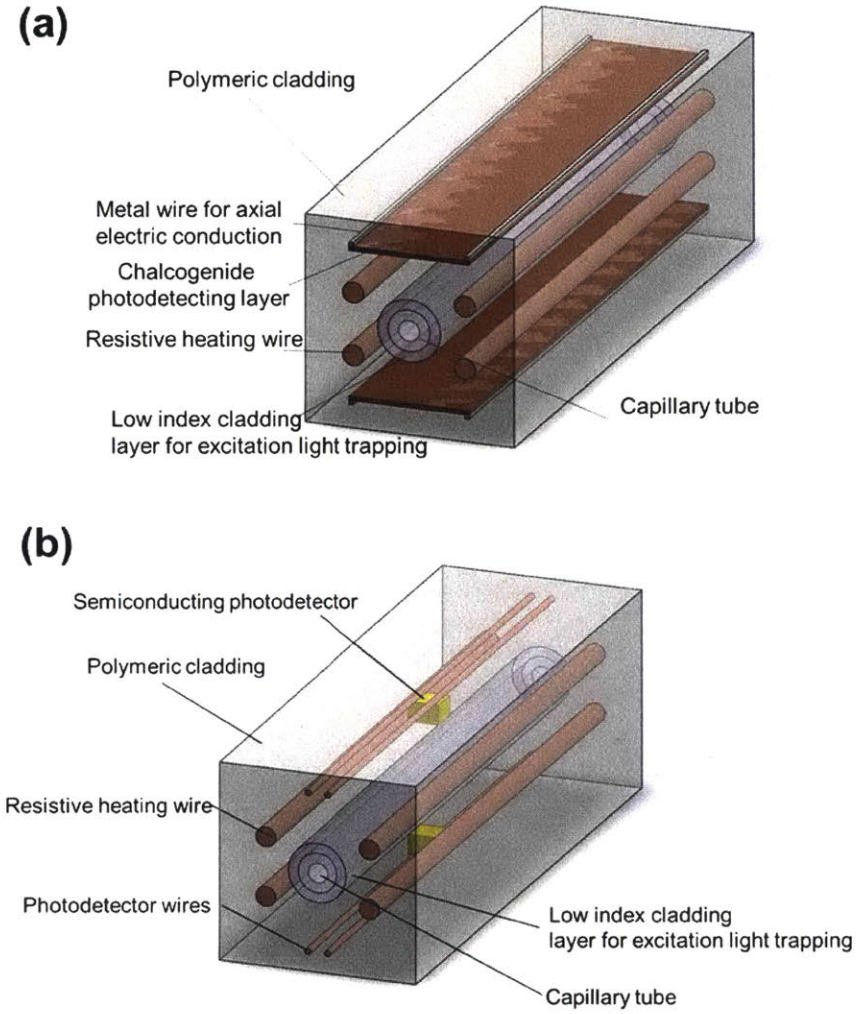

Figure 4-1: **SIMM fiber structure architecture**. (a) First alternative - hollow core capillary tube, light guiding layers, joule heaters and chalcogenide distributed photodetection layers. (b) Second alternative - similar structure to (a) but with a local, semiconducting photodetector embedded into the cladding for higher sensitivity.

It was decided for the first phase of the project to focus on the second option with commercial detectors as it could be incorporate detectors with much higher and linear sensitivity.

4.2.2 Determination of silica inner fiber core

FLIR's handheld explosive detectors utilize a single large borosilicate capillary coated with multiple sensing materials coated in 4 separate zones. It measures 54mm long, with an inner diameter of 0.6mm and an outer diameter of 5mm. The proposed SIMM fiber included a 100μm inner silica core designed to waveguide excitation light, and provide a chemically inert surface for the coating material. Experiments with silica microcapillaries produced by Polmicro Technologies showed that with a 100μm inner diameter, the air pumps used by the instruments were unable to draw a measurable airflow. Changing to a 320μm inner diameter allowed the instrument to draw the same airflow rate that has been shown to be optimal for explosive detection. The tubes produced by Polymicro are only available with a polyimide coating, which needs to be removed before incorporating the capillary tube into the SIMM fiber. A few trials were carried out to remove the coating from long sections of the tube. Removing the coating by burning it in a flame was ruled out since it requires a precise localization of the tube in the flame, to achieve complete decomposition of the coating, yet maintaining the shape of the capillary, without deforming it. Another approach was studied - removing the coating in the furnace at 600^{o}C. The tube was transferred to a steel mandrel (since the tubes are supplied on a plastic mandrel), and placed in a high-temperature furnace. Figure 4-2 shows the process of coating removal in the high - temperature furnace.

Unfortunately, after the coating was removed, the capillary glass was very fragile and was not able to withstand the bending stresses and strains that are required to remove it from the steel mandrel nor the stresses present at fiber draw. An alternative approach was chosen - incorporate a capillary tube with a coating. The coating that was chosen has both the ability to protect the tube from mechanical damage and has a low index of refraction so that the excitation light necessary to induce fluorescence in the explosive detecting layer will be confined to the high index silica glass. This is highly desirable since it prevents stray excitation light from reaching the photodetectors. This tubing was commercially available from Polymicro. However,

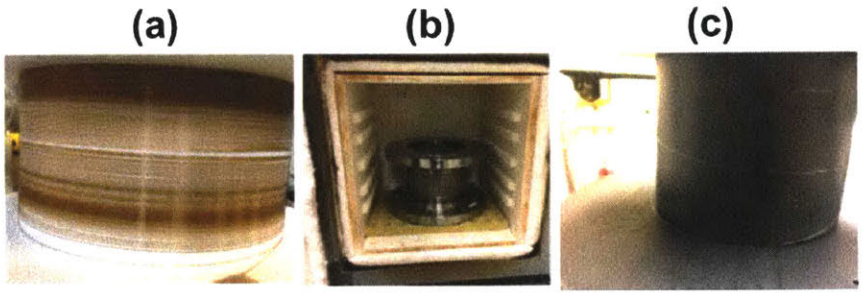

Figure 4-2: **Coating removal trials**. (a) Large inner diameter capillary tube coated with polyimide coating. (b) Capillary tube on steel mandrel in high temperature furnace. (c) Capillary tube after removal of coating in high temperature furnace.

it was only available in a 100μm inner diameter size.

4.2.3 Demonstration of light guiding in coated capillaries

The work described in this subsection was performed at FLIR by William McDaniel. It was believed that the low index cladding would provide a waveguiding function, trapping the excitation light in the silica core. With the detection material directly coated onto the silica it would be able to absorb some of the excitation light. The emission light would then be isotropically produced and not trapped by the silica's internal reflection. This assumption was examined before proceeding. Half of a Polymicro transparent capillary (part number #1068150140) was coated with TNT detection material. It was axially illuminated with an LED (wavelength of 415nm) and photographed. It was shown that the uncoated portion of the fiber had little to no excitation light detectable, as was expected and shown in Figure 4-3. Further, the coated portion away from the LED was excited by waveguided light and its emission was clearly visible. To confirm these observations, spectra were taken at the axial end opposite the LED, perpendicular to the capillary in the coated section, and in the uncoated section. While a small amount of excitation light was detected in the uncoated section of fiber, none was observed in the treated section. This adds confidence that no additional layers will be needed in the fiber to filter out excitation

light.

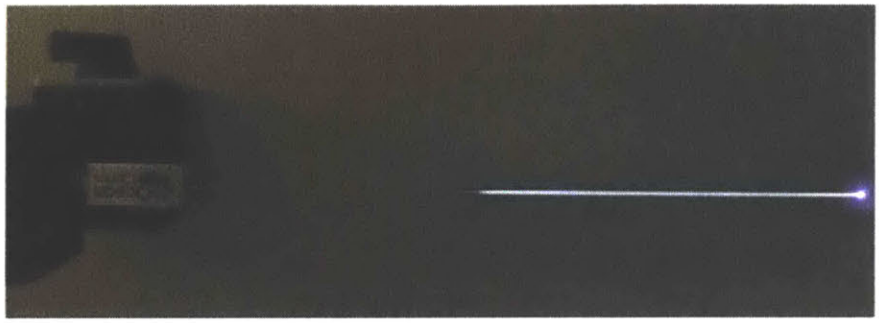

Figure 4-3: **Capillary tube light guiding experiment**. Polymicro capillary tube half treated with TNT detection chemistry and axially illuminated by a 415nm LED. No light is visible in the untreated section (left end) while the green polymer emission is clearly visible in the treated section (right end).

4.2.4 Incorporating commercially coated capillary into polymeric cladding

The convergence process to incorporate the coated glass capillary into polymeric preforms was developed using the commercial tubing. First, this tube was fed only into a plain polycarbonate preform to assess the parameters for successful converged draw. Figure 4-4 shows the structure of the polymeric preform used for the first draw. The capillary tube was fed through a hollow core preform holder to the central core of the preform. The size of the bore in the preform was chosen such that after the draw it reduces to approximately half of the diameter of the capillary, to ensure that no gaps between the preform and the capillary tube are formed. Figure 4-4 shows the resulting fiber with the capillary tube in the middle. Because of starting with a rectangular core and large tube outer diameter, the polymer couldn't effectively reflow to fill the gaps at the corners of the fiber, which left some voids in the structure. A modified structure was tested using a cylindrical core, which eliminated the empty corners in the fiber. The preform and the resulting fiber is shown in Figure 4-4(d) -

(e). With the cylindrical core, the material completely covers the capillary tube and no voids are visible in the fiber.

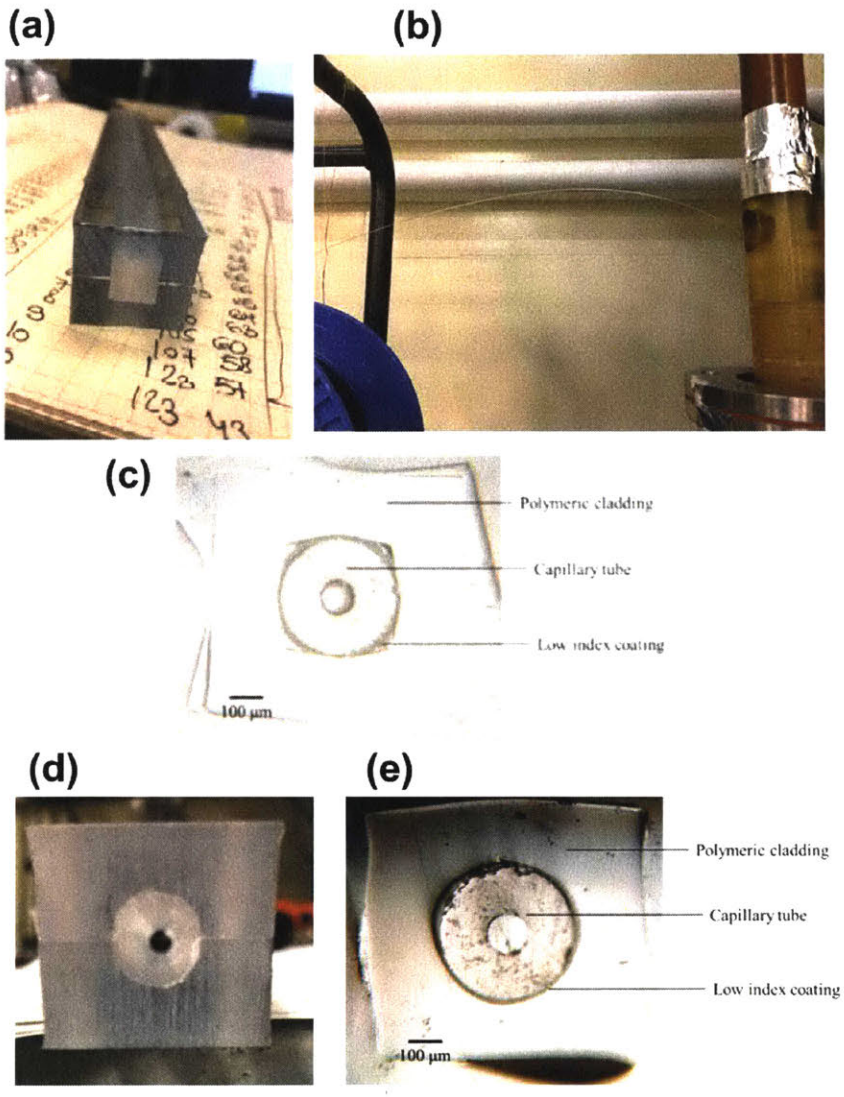

Figure 4-4: **Capillary tube convergence results**. (a) Image of polycarbonate preform with rectangular core used to draw fibers with convergence approach. (b) Image of the capillary tube fed to the preform holder during the fiber draw. (c) The resulting fiber. Voids at the corners of the fiber is clearly seen. (d) Image of the modified preform used. (e) Resulting fiber, with no voids visible.

4.2.5 Attempted draw of custom silica core

After demonstrating the proof of principal with the commercial low index coated tubing, it was desirable to produce a similar capillary with a larger inner diameter. A fluorinated polymer cladding coating material was purchased, and a custom fiber draw was attempted. A silica tube with the proper diameter was achieved, but the coating process was unsuccessful, as shown in Figure 4-5 . The final outer diameter was close to 1 millimeter when a size of 400μm was desired. Also, the cladding did not fully cure, leading to a soft, tacky surface, most probably due to the thickness of the fiber.

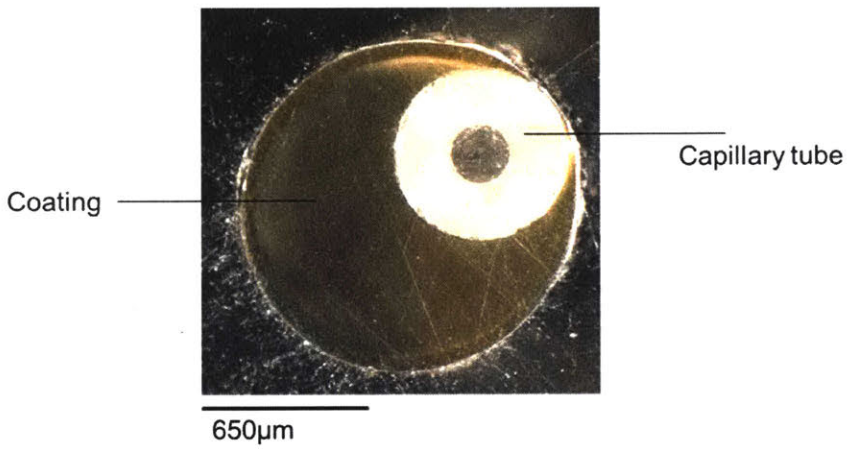

Figure 4-5: **Image of custom made silica capillary**. Inner diameter is 220μm. The outer diameter of the cladding is approximately 1mm. The silica is off-center and the cladding is tacky due to incomplete curing.

Unfortunately this project was defunded at this initial research and development stage. Future work will focus on optimization of the fiber structure - achieving desired capillary size, coated with low index of refraction fluoropolymer, embedded photodetectors and joule heaters.

Chapter 5

Conclusions and future work

This thesis described a methodology and applications of a few novel concepts in multi-material fibers. We have developed an approach to achieve selective break up in polymeric clad fibers. We have investigated and achieved a fully functional fiber system with connected discrete spherical photodetecting devices with continuous electrical buses positioned along its length. We have demonstrated self-assembly of chalcogenide semiconductors with conductive buses - achieving a functional, packaged, megapixel photodetecting fiber, and characterized the resonant behavior of these spherical photodetectors. The second part of my work was focused on developing and demonstrating of an alternative strategy for integrating active devices into fibers. Rather than addressing all the challenges of thermal drawing, we have developed a method to directly integrate commercial functional devices into fibers through thermal drawing. We have demonstrated operation of these fibers both in light emitting and photodetection mode. We have developed a technique to embed continuous low resistance wires to power high lengths of fibers. We have investigated ways to control the density of the devices in the fibers, embedding fibers into fabrics and establishing operation of the fibers in water and after machine washing cycles. Here we would like to expand on the future direction for research and development for these emerging technologies.

5.1 Harnessing fluid instability in fibers

Designing fiber structure through controlled fluid instability will enable new fiber functionality which was previously unattainable. The achievements of the current work could be applied and further developed in the following domains:

1. Inducing capillary instabilities at the fiber surface. Until now, capillary instability was induced within the inner core of the fiber. Investigating the possibility of inducing fluid instability of an electrically conductive domain at the surface of the fiber will potentially enable a very powerful capability - provide a way to connect with a particular device within the fiber. Until now, due to the translational symmetry of conductors within the fiber, connection was made to all devices present in the fiber through a common conductor, and no strategy to connection with a selected device or feature along the length of the fiber is available. Inducing a selective break up at the fiber surface, will provide a viable way to make a discrete electrical connection to devices within the fiber.

2. Inducing selective break up in silica clad fibers provides a great path to produce high density electronic devices in fibers. Inducing fluid instablity in these fibers provide a pathway to avoid substantial diffusion and mixing during the draw. Building upon recent publications [14, 24] selective break up was established in silica clad fibers. This capability may pave the way to achieve high density fiber electronic devices. Recent work [87] showed that it is possible to produce compositionally segregated SiGe Janus particles in silica clad fibers. These particles may have interesting electronic properties, specifically rectifying behavior - since a heterojunction could be formed between the Si and Ge in the particle. Drawing a fiber with SiGe core and two adjacent Pt cores, followed by induction of selective break up, could yield a self assembled, crystalline semiconducting devices in the fiber, which could be a an enabling technology for fiber based high bandwidth photodetectors, as one example to a potential application.

3. Complimentary to selective break up, coherent break up is a potential avenue

to achieve high density fiber electronics. Studying effective ways to control and guide break up of two adjacent cores to occur in concert and touch will enable another degree of freedom. Directing this process will allow to make p-n, p-i-n, transistor and other structurally complex devices in fibers.

5.2 Integration of microelectronic devices in fibers

Achievements in this domain have shown an immediate impact on enabling novel fiber functionality and unlocking highly desired fiber capabilities. This work could be further developed in the following domains:

1. Fabric to fabric communication system. Light emitting fibers and photodetecting fibers could be weaved into the same fabric to establish two way fabric to fabric communication system. Electrical circuitry will enable to extend the communication range.

2. Indoor navigation system. Photodetecting fibers could be coupled with strong directional emitters to enable local information transfer to the fibers.

3. Covert communication system could be established by directional laser system and photodetecting fibers.

4. Light emitting and photodetecting fibers could be used for body monitoring applications. Photoplethysmography (PPG) and oximetry are two technologies that could be enabled by these fibers [88, 89].

5. Integrating light emitting laser diodes in fibers could extend the operational communication range of the fibers.

5.3 Fibers for multianalyte explosives sensing

The work in this chapter could be continued in a few directions:

1. Continuing the effort to achieve the desired objectives in this project by further optimizing the convergence of coated silica capillaries in polymeric cladding, and embedding heaters and high sensitivity crystalline photodetectors in the fiber structure.

2. Employing a similar approach for magnetic field sensing by incorporating nitrogen vacancy diamonds in fibers. The fluorescence spectra of these diamonds is very sensitive to small magnetic fields [90]. Incorporating these particles in a similar fashion to the chemiluminescent materials for explosive sensing, could pave the way to enable compact and portable technique to measure magnetic fields with high precision.

Appendix A

Electrical behavior model of spherical semiconductor fibers

Our goal was to develop a model for the electric behavior of fibers that contain continuous electrodes and semiconducting spheres. We have done it in several steps.

1. Resistance of a single sphere: Since a resistance of a perfect sphere is infinite due to two singular contact points, we approximate this problem, by introducing a truncated sphere. Assuming the sphere has a homogeneous conductivity σ, an infinitesimal unit of the sphere has a resistance of: $d\Re = dz/\sigma A(z)$, where z is the axis pointed between the two truncated caps, and $A(z)$ is the area that is defined by z, which is normal to the area of the sphere. Integrating $d\Re$ with respect to z gives the resistance of a sphere - $\Re$:

$$\Re = \frac{1}{\pi R\sigma} \ln\left(\frac{R+b}{R-b}\right) = \frac{1}{\pi R\sigma} \ln\left(\frac{1+\Omega}{1-\Omega}\right) \tag{A.1}$$

   Where R is the sphere radius, σ is the conductivity of the semiconductor, b is the distance between the truncated cap and the center of the sphere, and $\Omega = b/R$ is the contact factor, which is a function of the contact between the electrodes and the sphere.

2. The next step is to consider a fiber system which contains only one sphere that

is connected to continuous electrodes. Here we assume that conductors have much smaller resistance than the semiconducting sphere, as it is in our case, and that there is no junction resistance between the electrodes and the sphere, at the contact. The carrier generation rate [91] is given by equation A.2:

$$\frac{n - n_{dark}}{\tau} = \frac{\eta\Phi}{\text{Volume}} = \frac{3\eta\Phi}{4\pi R^3} \tag{A.2}$$

Where n is the carrier density in the semiconductor, n_{dark} is the carrier density in the semiconductor without illumination, τ is the carrier lifetime, Φ is the photon flux and η is the quantum efficiency. For the case of As_2Se_5, which is an amorphous arsenic selenium semiconductor, the electric transport is governed by holes [92]. Quantum efficiency of photo-generation and collection η for a spherical particle is given by equation A.3:

$$\eta = \zeta \cdot Q_{abs} \tag{A.3}$$

where $\zeta = \frac{\tau}{\tau + \tau_{\text{transit}}}$ is the carrier collection efficiency that depends on the carrier lifetime and the transit time of the carrier from the location of formation to the collecting electrode; Q_{abs} is the normalized absorption cross section of a sphere, which is derived by Mie theory [53]. This value describes the interaction of the electromagnetic radiation with the sphere and is the ratio between the absorbed photo-energy versus the incident energy, when the sphere is illuminated. Substituting equation A.3 into equation A.2 we can obtain the conductivity of a semiconducting sphere σ which is given by equation A.4:

$$\sigma = en\mu = \frac{3e\mu\zeta Q_{abs}\Phi\tau}{4\pi R^3} + en\mu_{dark} \tag{A.4}$$

Where e is the electron charge, and μ is the hole mobility. The illuminated sphere resistance is given by substituting equation A.4 into equation A.1:

$$\Re = \frac{1}{\pi R\sigma} \ln\left(\frac{1+\Omega}{1-\Omega}\right) = \frac{4R^2 \ln\left(\frac{1+\Omega}{1-\Omega}\right)}{e\mu(4R^3\pi n_{dark} + 3\zeta\tau\Phi Q_{abs})} \tag{A.5}$$

3. In this step we look at a fiber that contains continuous electrodes, and a series of spheres all connected to these electrodes. At this step, only one sphere is being illuminated while other are in the dark. In this case only the dark current should change. We now have $N = L/\lambda$ spheres in the system where L is the length of the active fiber region that is defined by the distance between the connections to the fiber electrodes by the external measurement setup and λ is the wavelength of periodicity which evolves during break up. Conductivity of the illuminated sphere is given by equation A.4 while the conductivity of the spheres that are not illuminated is:

$$\sigma_{dark} = e\mu n_{dark} \tag{A.6}$$

The resistance of the illuminated sphere is given by equation A.5 and the resistance of the spheres in the dark is:

$$\Re_{dark} = \frac{\ln\left(\frac{1+\Omega}{1-\Omega}\right)}{Re\pi\mu n_{dark}} \tag{A.7}$$

Since these spheres are all connected in parallel, the total resistance $\Re_{tot}$ of the system is:

$$\frac{1}{\Re_{tot}} = \frac{1}{\Re} + \frac{\frac{L}{\lambda} - 1}{\Re_{dark}} = \frac{e\mu(4R^3 L\pi n_{dark} + 3\zeta\tau\Phi Q_{abs}\lambda)}{4R^2 \ln\left(\frac{1+\Omega}{1-\Omega}\right)\lambda} \tag{A.8}$$

The current in the system, I is thus:

$$I = \frac{V}{\Re_{tot}} = \frac{Ve\mu(4R^3 L\pi n_{dark} + 3\zeta\tau\Phi Q_{abs}\lambda)}{4R^2 \ln\left(\frac{1+\Omega}{1-\Omega}\right)\lambda} \tag{A.9}$$

Where V is the applied voltage. The dark current which is present when the fiber is not illuminated ($\Phi = 0$) is given by the following equation:

$$I_{dark} = \frac{ReL\pi\mu n_{dark}}{\ln\left(\frac{1+\Omega}{1-\Omega}\right)\lambda} V \tag{A.10}$$

As can be seen in Figure 2-14(b) the dark current is not linear with voltage. The reason for this nonlinear behavior is the dependence of the mobility of holes on the field, which is described by the Poole Frenkel effect [55, 92]. The dependence of the mobility on the field is exponential as shown in the following equation:

$$\mu = \frac{N_v}{N_t}\mu_0 \exp\left(-\frac{U_0}{kT}\right)\exp\left(\frac{\beta E^{1/2}}{kT}\right) \tag{A.11}$$

where N_v is the the density of states in the valence band, N_t is the density of the trapping centers, μ_0 is the carriers' microscopic mobility, U_0 is the thermal activation energy at zero field, and β is the Poole Frenkel constant. There are no exact values in the literature of As_2Se_5 for N_v, N_t, μ_0, U_0, and β, but for a very similar and commonly used material As_2Se_3: $\frac{N_v}{N_t}\mu_0 \approx 3 \cdot 10^{-3} m^2 V^{-1} s^{-1}$; $U_0 = 0.43$eV and $\beta = 1.85 \cdot 10^{-}5$ eV $m^{1/2}V^{-1/2}$ as reported in [92]. The dark current has thus the following form:

$$I_{dark} = \frac{ReL\pi V n_{dark}}{\ln\left(\frac{1+\Omega}{1-\Omega}\right)}\left(\frac{N_v}{N_t}\right)\mu_0 \exp\left(-\frac{U_0}{kT}\right)\exp\left(\frac{\beta V^{1/2}}{kT(2R)^{1/2}}\right) = A{\cdot}V \exp B\left(\frac{V}{2R}\right)^{1/2} \tag{A.12}$$

Where A and B are constants which were used as parameters to fit the expression in equation A.12 to the experimental data. The fit results are summarized in Table A.1.

Table A.1: **Summary of fit results**

Sphere Radius R (μm)	A ($A\ V^{-1}$)	B ($[m/V]^{1/2}$)
5	$2 \cdot 10^{-15} \pm 1 \cdot 10^{-15}$	$9.2 \cdot 10^{-4} \pm 1.2 \cdot 10^{-4}$
11	$8 \cdot 10^{-13} \pm 4 \cdot 10^{-13}$	$6.9 \cdot 10^{-4} \pm 1.2 \cdot 10^{-4}$

According to the values of B in Table A.1 we find that the Poole Frenkel constant - β remains constant regardless of the sphere radius, ($\beta_{11\mu m} = 17 \pm 3\mu eV(m/V)^{1/2}$; $\beta_{5\mu m} = 23{\pm}3\mu eV(m/V)^{1/2}$; previously reported values of β [92] - $\beta = 18{\pm}2\mu eV(m/V)^{1/2}$), assuming that the temperature of the semiconductor didn't change during laser illumination. On the other hand, the values of the pre-factor A change considerably between the experiments; this could not be explained just by the difference in sphere

radius. These differences are most probably affected by the contact area between the sphere and the electrodes (mathematically described by the Ω factor), which has a significant influence on the pre-factor A.

The responsivity ρ of the fiber, when only one sphere is illuminated is given by equation A.13:

$$\rho = \frac{I - I_{dark}}{P} = \frac{3eV\zeta\lambda_{illum}\mu\tau Q_{abs}}{4hcR^2 \ln\left(\frac{1+\Omega}{1-\Omega}\right)} \tag{A.13}$$

Where P is the power of the illumination that is incident on the sphere/s, and $\Phi = \frac{P\lambda_{illum}}{hc}$, h is Planck's constant; c is the speed of light, λ_{illum} is the wavelength of the incident light. This relation could further be simplified, by substituting equation A.16 into equation A.13:

$$\rho = \frac{3\zeta\lambda_{illum}\tau Q_{abs} I_{dark}\lambda}{4hcR^3 L\pi n_{dark}} \tag{A.14}$$

In order to compare the responsivities between various experiments, we have normalized it by the applied voltage:

$$\rho_m = \frac{\rho}{V} = \frac{3\zeta\lambda_{illum}\tau Q_{abs} I_{dark}\lambda}{4hcR^3 L\pi n_{dark} V} \tag{A.15}$$

This theoretical value was compared with the experimental values obtained for the different sphere sizes (radii of 5μm and 11μm) and for single and multiple sphere excitation. The experimental normalized responsivity ($\rho_{m_{ex}}$) was calculated by using the following equation:

$$\rho_{m_{ex}} = \frac{I_{meas} - I_{dark}}{P_{meas}} \alpha_{geom} \tag{A.16}$$

Where I_{meas} is the measured current, P_{meas} is the total power supplied by the laser, and α_{geom} is a geometrical factor that takes into account the relative power that was incident on the spheres. Assuming that the laser beam flux is a two dimensional Gaussian, it is possible to calculate the factor α_{geom} by the following equation:

$$I_{meas} = \rho_{m_{ex}} P_{meas} \int_S G(x,y)dS \tag{A.17}$$

Where $G(x,y)$ is the Gaussian beam, experimentally measured, with FWHM s_x, s_y

in the direction of the fiber axis and perpendicularly to the fiber axis, respectively. Comparing equation A.16 and equation A.17 gives us the value of α_{geom}:

$$\alpha_{geom} = \frac{1}{\int_S G(x,y)dS} \tag{A.18}$$

The expression given in equation A.18 gives us α_{geom} for a single sphere excitation regime. Multi-sphere excitation factor is calculated by integration on all the spheres in the fiber, taking into account their position relative to the Gaussian beam center, as given in the following equation:

$$\alpha_{geom_{multi}} = \frac{1}{\int_{S_0} G(x,y)dS \sum_i \exp\left(-\frac{x_i^2}{2\sigma_x^2}\right)} \tag{A.19}$$

Here S_0 is the area of the sphere that coincides with the Gaussian center, and $\sigma_x = \frac{s_x}{2\sqrt{2\log 2}}$. The geometric factor α_{geom} was calculated for every experiment conducted using the following experimental data: The FWHM of the beam in single sphere excitation (spherical lens) - $s_x = s_y = 22\mu m$. The FWHM of the beam in multiple sphere excitation (cylindrical lens) $s_x = 462\mu m$; $s_y = 180\mu m$. The geometric corrections are summarized in Table A.2.

Table A.2: **Summary of geometric correction factors.**

Sphere Radius R (μm)	α_{geom}, Single Sphere	α_{geom}, Multiple Sphere
5	7.5	85.9
11	2	34.4

The values of the measured responsivity such as shown in Figure 2-19 were calculated by equation A.16 taking into account the different values of the geometric correction factors given in Table A.2. The theoretical values of the responsivity were calculated by equation A.15 using material parameters summarized in Table A.3.

As a comparison between the experiments and theory, an average of the responsivity was taken in an illumination wavelength range of 825-850nm. Table A.4 sum-

Table A.3: **Properties used for theoretical responsivity calculation.**

Property	Symbol	$R = 5\mu$m	$R = 11\mu$m
Carrier lifetime (s)	τ	$2 \cdot 10^{-5}$	
Voltage (V)	V	100	
Carrier mobility ($m^2 s^{-1}$)	μ	$1.58 \cdot 10^{-9}$	
Transit time (s)	$\tau_{transit}$	$6.3 \cdot 10^{-4}$	$6.1 \cdot 10^{-3}$
Carrier collection efficiency	ζ	0.031	$3.25 \cdot 10^{-3}$
Dark Current (A)	I_{dark}	$1.3 \cdot 10^{-11}$	$1.88 \cdot 10^{-10}$
Sphere periodicity wavelength (μm)	λ	68	35
Concentration of intrinsic carriers [93] (m^{-3})	n_{dark}	$1.3 \cdot 10^{17}$	
Specimen length (m)	L	0.05	

marizes the measured responsivities and expected responsivity from theory, for one measurement from each type.

Table A.4: **Summary of the measured normalized responsivity and the calculated responsivity from theory.**

Sphere Radius R (μm)	ρ_m, Single Sphere ($nAW^{-1}V^{-1}$)	ρ_m, Multiple Sphere ($nAW^{-1}V^{-1}$)	Calculated ρ_m ($nAW^{-1}V^{-1}$)
5	19.3	12.5	20.5
11	14.4	14.1	19.1

In Table A.4 we notice that the measured responsivity is very similar to the theoretical prediction, taking into to account the fact that the calculation of the theoretical responsivity was a first order model. The variance between the responsivity of the results obtained for multiple - sphere and single - sphere excitations could be attributed to the number of connected spheres. From these values it is most probable that in the multiple sphere experiment the majority of the spheres were connected in specimens with spheres of 11μm radius, and $\sim$ 35% of the spheres were disconnected in specimens with 5μm radius. It is reasonable that as the sphere radius decreases, the effect of electrode fluctuations and sphere size dispersion will adversely affect the contact between the electrodes and the spheres, increasing the number of misconnections, as supported by the electrical measurements.

THIS PAGE INTENTIONALLY LEFT BLANK

Bibliography

[1] E. Kvavadze, O. Bar-Yosef, A. Belfer-Cohen, E. Boaretto, N. Jakeli, Z. Matskevich, and T. Meshveliani, "30,000-Year-Old Wild Flax Fibers," *Science*, vol. 325, p. 1359, 2009.

[2] J. C. Splitstoser, T. D. Dillehay, J. Wouters, and A. Claro, "Early pre-Hispanic use of indigo blue in Peru," *Science Advances*, vol. 2, p. e1501623, 2016.

[3] G. de Wyss, "The Ripening of Viscose," *Industrial and Engineering Chemistry*, vol. 17, no. 10, pp. 1043–1045, 1925.

[4] M. I. Kohan, *Nylon plastics handbook*. Hanser Publishers, New York, 1995.

[5] K. Perepelkin, "Poly (Ethylene Terephthalate) and Polyester Fibres 60th Anniversary of the first patent," *Fibre Chemistry*, vol. 33, no. 5, pp. 333–339, 2001.

[6] D. E. Brown, *Inventing Modern America*. The MIT Press, 2003.

[7] J. Gorss, "American Chemical Society National Historic Chemical Landmarks. High Performance Carbon Fibers," 2003.

[8] S. M. Kurtz, *The UHMWPE Handbook: Ultra-High Molecular Weight Polyethylene in Total Joint Replacement*. Academic Press, 2004.

[9] J. Hecht, *City of Light: The Story of Fiber Optics*. Oxford University Press, 2004.

[10] P. Russell, "Photonic crystal fibers," *Science*, vol. 299, pp. 358–362, 2003.

[11] A. F. Abouraddy, M. Bayindir, G. Benoit, S. D. Hart, K. Kuriki, N. Orf, O. Shapira, F. Sorin, B. Temelkuran, and Y. Fink, "Towards multimaterial multifunctional fibres that see, hear, sense and communicate," *Nature materials*, vol. 6, no. 5, pp. 336–347, 2007.

[12] A. Gumennik, A. M. Stolyarov, B. R. Schell, C. Hou, G. Lestoquoy, F. Sorin, W. McDaniel, A. Rose, J. D. Joannopoulos, and Y. Fink, "All-in-fiber chemical sensing," *Advanced materials*, pp. 1–5, 2012.

[13] C. Hou, X. Jia, L. Wei, S.-C. Tan, X. Zhao, J. D. Joannopoulos, and Y. Fink, "Crystalline silicon core fibres from aluminium core preforms," *Nature Communications*, vol. 6, p. 6248, 2015.

[14] L. Wei, C. Hou, E. Levy, G. Lestoquoy, A. Gumennik, A. F. Abouraddy, J. D. Joannopoulos, and Y. Fink, "Optoelectronic Fibers via Selective Amplification of In-Fiber Capillary Instabilities," *Advanced Materials*, vol. 29, pp. 1–6, 2017.

[15] P. J. Toal, L. J. Holmes, R. X. Rodriguez, and E. D. Wetzel, "Microstructured monofilament via thermal drawing of additively manufactured preforms," *Additive Manufacturing*, vol. 16, pp. 12–23, 2017.

[16] J. Klein, M. Stern, G. Franchin, M. Kayser, C. Inamura, S. Dave, J. C. Weaver, P. Houk, P. Colombo, M. Yang, and N. Oxman, "Additive Manufacturing of Optically Transparent Glass," *3D Printing and Additive Manufacturing*, vol. 2, no. 3, pp. 92–105, 2015.

[17] B. Temelkuran, S. D. Hart, G. Benoit, J. D. Joannopoulos, and Y. Fink, "Wavelength-scalable hollow optical fibres with large photonic bandgaps for CO2 laser transmission.," *Nature*, vol. 420, pp. 650–653, 2002.

[18] S. D. Hart, G. R. Maskaly, B. Temelkuran, P. H. Prideaux, J. D. Joannopoulos, and Y. Fink, "External reflection from omnidirectional dielectric mirror fibers.," *Science*, vol. 296, pp. 510–513, 2002.

[19] M. Bayindir, F. Sorin, A. Abouraddy, and J. Viens, "Metal - insulator - semiconductor optoelectronic fibres," *Nature*, vol. 431, 2004.

[20] M. Bayindir, A. F. Abouraddy, O. Shapira, J. Viens, D. Saygin-Hinczewski, F. Sorin, J. Arnold, J. D. Joannopoulos, and Y. Fink, "Kilometer-Long Ordered Nanophotonic Devices by Preform-to-Fiber Fabrication," *IEEE Journal of Selected Topics in Quantum Electronics*, vol. 12, pp. 1202–1213, nov 2006.

[21] S. Egusa, Z. Wang, N. Chocat, Z. M. Ruff, a. M. Stolyarov, D. Shemuly, F. Sorin, P. T. Rakich, J. D. Joannopoulos, and Y. Fink, "Multimaterial piezoelectric fibres," *Nature Materials*, vol. 9, pp. 643–648, 2010.

[22] N. Chocat, G. Lestoquoy, Z. Wang, D. M. Rodgers, J. D. Joannopoulos, and Y. Fink, "Piezoelectric fibers for conformal acoustics.," *Advanced Materials*, vol. 24, pp. 5327–32, 2012.

[23] S. Danto, F. Sorin, N. D. Orf, Z. Wang, S. A. Speakman, J. D. Joannopoulos, and Y. Fink, "Fiber field-effect device via in situ channel crystallization," *Advanced Materials*, vol. 22, pp. 4162–4166, 2010.

[24] A. Gumennik, L. Wei, G. Lestoquoy, A. M. Stolyarov, X. Jia, P. H. Rekemeyer, M. J. Smith, X. Liang, B. J.-B. Grena, S. G. Johnson, S. Gradecak, A. F. Abouraddy, J. D. Joannopoulos, and Y. Fink, "Silicon-in-silica spheres via axial thermal gradient in-fibre capillary instabilities," *Nature communications*, vol. 4, p. 2216, 2013.

[25] J. Ballato, T. Hawkins, P. Foy, R. Stolen, B. Kokuoz, M. Ellison, C. McMillen, J. Reppert, a. M. Rao, M. Daw, S. R. Sharma, R. Shori, O. Stafsudd, R. R. Rice, and D. R. Powers, "Silicon optical Fiber," *Optics Express*, vol. 16, no. 23, p. 18675, 2008.

[26] A. M. Stolyarov, L. Wei, O. Shapira, F. Sorin, S. L. Chua, J. D. Joannopoulos, and Y. Fink, "Microfluidic directional emission control of an azimuthally polarized radial fibre laser," *Nature Photonics*, vol. 6, no. 4, pp. 229–233, 2012.

[27] T. Khudiyev, C. Hou, A. M. Stolyarov, and Y. Fink, "Sub-Micrometer Surface-Patterned Ribbon Fibers and Textiles," *Advanced Materials*, vol. 29, pp. 1–6, 2017.

[28] A. Canales, X. Jia, U. P. Froriep, R. a. Koppes, C. M. Tringides, J. Selvidge, C. Lu, C. Hou, L. Wei, Y. Fink, and P. Anikeeva, "Multifunctional fibers for simultaneous optical, electrical and chemical interrogation of neural circuits in vivo," *Nat Biotech*, vol. 33, no. 3, pp. 277–284, 2015.

[29] G. Tao, A. F. Abouraddy, A. M. Stolyarov, and Y. Fink, *Lab-on-Fiber Technology*. Springer International Publishing Switzerland, 2015.

[30] J. Plateau, *Statique expérimentale et théorique des liquides soumis aux seules forces moléculaires*. Paris: Gauthier-Villars, 1873.

[31] Lord Rayleigh, "On the Capillary Phenomena of Jets," *Proceedings of the Royal Society of London*, vol. 29, pp. 71–97, 1879.

[32] Lord Rayleigh, "On the instability of a cylinder of viscous liquid under capillary force," *Philosophical magazine and Journal of Science*, vol. 34, no. 207, 1892.

[33] N. D. Orf, O. Shapira, F. Sorin, S. Danto, M. A. Baldo, J. D. Joannopoulos, and Y. Fink, "Fiber draw synthesis," *Proceedings of the National Academy of Sciences*, vol. 108, no. 12, pp. 4743–4747, 2011.

[34] C. Hou, X. Jia, L. Wei, A. M. Stolyarov, O. Shapira, J. D. Joannopoulos, and Y. Fink, "Direct atomic-level observation and chemical analysis of ZnSe synthesized by in situ high-throughput reactive fiber drawing," *Nano letters*, vol. 13, no. 3, pp. 975–9, 2013.

[35] D. S. Deng, N. D. Orf, a. F. Abouraddy, a. M. Stolyarov, J. D. Joannopoulos, H. a. Stone, and Y. Fink, "In-fiber semiconductor filament arrays," *Nano Letters*, vol. 8, no. 12, pp. 4265–9, 2008.

[36] D. S. Deng, J. C. Nave, X. Liang, S. G. Johnson, and Y. Fink, "Exploration of in-fiber nanostructures from capillary instability," *Optics Express*, vol. 19, no. 17, pp. 219–222, 2011.

[37] J. J. Kaufman, G. Tao, S. Shabahang, D. S. Deng, Y. Fink, and A. F. Abouraddy, "Thermal drawing of high-density macroscopic arrays of well-ordered sub-5-nm-diameter nanowires," *Nano Letters*, vol. 11, no. 11, pp. 4768–4773, 2011.

[38] J. Kaufman, G. Tao, S. Shabahang, E.-H. Banaei, D. S. Deng, X. Liang, S. G. Johnson, Y. Fink, and A. F. Abouraddy, "Structured spheres generated by an in-fibre fluid instability," *Nature*, vol. 487, no. 7408, pp. 463–7, 2012.

[39] B. Grena, *Phase separation in thermally-drawn fibers: From porous domains to structured Si-Ge spheres.* PhD thesis, Massachusetts Institute of Technology, 2017.

[40] F. Sorin, G. Lestoquoy, S. Danto, J. D. Joannopoulos, and Y. Fink, "Resolving optical illumination distributions along an axially symmetric photodetecting fiber," *Optics express*, vol. 18, no. 23, pp. 24264–75, 2010.

[41] M. Rein, E. Levy, A. Gumennik, A. Abouraddy, J. Joannopolous, and Y. Fink, "Self-assembled fibre optoelectronics with discrete translational symmetry," *Nature Communications*, 2016.

[42] S. Tomotika, "On the Instability of a Cylindrical Thread of a Viscous Liquid Surrounded by Another Viscous Fluid," *Proceedings of the Royal Society A: Mathematical, Physical and Engineering Sciences*, vol. 150, no. 870, pp. 322–337, 1935.

[43] S. D. Hart and Y. Fink, "Interfacial Energy and Materials Selection Criteria in Composite Microstructured Optical Fiber Fabrication," in *Materials Research Society Symposium Proceedings*, vol. 797, pp. 1–7, 2004.

[44] J. Dann, "Forces involved in the adhesive process," *Journal of Colloid and Interface Science*, vol. 32, no. 2, pp. 302–320, 1970.

[45] M. Bayindir, O. Shapira, D. Saygin-Hinczewski, J. Viens, A. F. Abouraddy, J. D. Joannopoulos, and Y. Fink, "Integrated fibres for self-monitored optical transport," *Nature Materials*, vol. 4, no. 11, pp. 820–825, 2005.

[46] A. F. Abouraddy, O. Shapira, M. Bayindir, J. Arnold, F. Sorin, D. S. Hinczewski, J. D. Joannopoulos, and Y. Fink, "Large-scale optical-field measurements with geometric fibre constructs.," *Nature materials*, vol. 5, no. 7, pp. 532–6, 2006.

[47] A. B. Matsko and V. S. Ilchenko, "Optical resonators with whispering-gallery modes-part I: basics," *IEEE Journal of Selected Topics in Quantum Electronics*, vol. 12, no. 1, pp. 3–14, 2006.

[48] A. Yariv and P. Yeh, *Photonics.* New York, NY: Oxford University Press, 6th ed., 2007.

[49] G. Elliott and D. Hewak, "Chalcogenide glass microspheres; their production, characterization and potential," *Optics express*, vol. 15, no. 26, pp. 321–322, 2007.

[50] P. Wang, T. Lee, M. Ding, A. Dhar, T. Hawkins, P. Foy, Y. Semenova, Q. Wu, J. Sahu, G. Farrell, J. Ballato, and G. Brambilla, "Germanium microsphere high-Q resonator.," *Optics letters*, vol. 37, no. 4, pp. 728–30, 2012.

[51] O. Aktas, E. Ozgur, O. Tobail, M. Kanik, E. Huseyinoglu, and M. Bayindir, "A New Route for Fabricating On-Chip Chalcogenide Microcavity Resonator Arrays," *Advanced Optical Materials*, vol. 2, no. 7, pp. 618–625, 2014.

[52] M. Garin, R. Fenollosa, R. Alcubilla, L. Shi, L. F. Marsal, and F. Meseguer, "All-silicon spherical-Mie-resonator photodiode with spectral response in the infrared region," *Nature communications*, vol. 5, p. 3440, 2014.

[53] C. Bohren and D. Huffman, *Absorption and scattering of light by small particles.* Weinheim, Germany: Wiley, 2004.

[54] J. Ward and O. Benson, "WGM microresonators: sensing, lasing and fundamental optics with microspheres," *Laser & Photonics Reviews*, vol. 5, no. 4, pp. 553–570, 2011.

[55] D. Lamb, *Electrical conduction mechanisms in thin insulating films.* London, UK: Methuen Monographs, 1967.

[56] R. Swanepoel, "Determination of the thickness and optical constants of amorphous silicon," *Journal of Physics E: Scientific Instruments*, vol. 16, no. 12, pp. 1214–1222, 1983.

[57] P. D. Garcia, R. Sapienza, J. Bertolotti, M. D. Martin, A. Blanco, A. Altube, L. Vina, D. S. Wiersma, and C. Lopez, "Resonant light transport through Mie modes in photonic glasses," *Physical Review A*, vol. 78, pp. 1–11, 2008.

[58] B. Mascaro, T. Brunet, O. Poncelet, C. Aristegui, S. Raffy, O. Mondain-Monval, and J. Leng, "Impact of polydispersity on multipolar resonant scattering in emulsions," *Journal of Acoustical Society of America*, vol. 133, no. 4, pp. 1996–2003, 2013.

[59] P. Chylek, "Resonance structure of Mie scattering : distance between resonances," *Journal of Optical Society of America A*, vol. 7, no. 9, pp. 1609–1613, 1990.

[60] L. G. Kazovsky, *Optical fiber communication systems.* Boston, MA: Artech House, 1996.

[61] M. Stoppa and A. Chiolerio, "Wearable Electronics and Smart Textiles: A Critical Review," *Sensors*, vol. 14, pp. 11957–11992, 2014.

[62] W. Weng, P. Chen, S. He, X. Sun, and H. Peng, "Smart Electronic Textiles," *Angewandte Chemie*, vol. 55, pp. 6140–6169, 2016.

[63] M. Daniel, "Light emitting fabric. United States Patent 4,234,907," 1980.

[64] J. Berzowska and A.-m. Laflamme, "PLEET : Light-emitting Electronic Garment," *Fashion Practice*, vol. 3, no. 1, pp. 11–28, 2011.

[65] B. Selm, M. Rothmaier, M. Camenzind, T. Khan, and H. Walt, "Novel flexible light diffuser and irradiation properties for photodynamic therapy," *Journal of Biomedical Optics*, vol. 12, no. 3, pp. 1–7, 2007.

[66] M. N. Zervas and C. A. Codemard, "High Power Fiber Lasers : A Review," *IEEE Journal of Selected Topics in Quantum Electronics*, vol. 20, no. 5, 2014.

[67] S. Kwon, W. Kim, H. Kim, S. Choi, B.-C. Park, S.-H. Kang, and K. C. Choi, "High Luminance Fiber-Based Polymer Light-Emitting Devices by a Dip-Coating Method," *Advanced Electronic Materials*, p. 1500103, 2015.

[68] Z. Zhang, K. Guo, Y. Li, X. Li, G. Guan, H. Li, Y. Luo, F. Zhao, Q. Zhang, B. Wei, Q. Pei, and H. Peng, "A colour-tunable, weavable fibre-shaped polymer light-emitting electrochemical cell," *Nature Photonics*, vol. 9, no. 4, pp. 233–238, 2015.

[69] B. O'Connor, K. H. An, Y. Zhao, K. P. Pipe, and M. Shtein, "Fiber Shaped Light Emitting Device," *Advanced Materials*, vol. 19, no. 22, pp. 3897–3900, 2007.

[70] B. O'Connor, K. P. Pipe, and M. Shtein, "Fiber based organic photovoltaic devices," *Applied Physics Letters*, vol. 92, no. 19, pp. 2006–2009, 2008.

[71] W. Kim, S. Kwon, S.-m. Lee, J. Y. Kim, Y. Han, E. Kim, K. C. Choi, S. Park, and B.-c. Park, "Soft fabric-based flexible organic light-emitting diodes." 2013.

[72] K. H. Cherenack, T. Kinkeldei, C. Zysset, and G. Troster, "Woven Thin-Film metal interconnects," *IEEE Electron Device Letters*, vol. 31, no. 7, pp. 740–742, 2010.

[73] K. Cherenack, C. Zysset, T. Kinkeldei, N. Münzenrieder, and G. Tröster, "Woven electronic fibers with sensing and display functions for smart textiles," *Advanced Materials*, vol. 22, no. 45, pp. 5178–5182, 2010.

[74] T. Dias and A. Ratnayake, *Integration of micro-electronics with yarns for smart textiles.* Elsevier Ltd., 2015.

[75] S. Nakamura, T. Mukai, and M. Senoh, "Candela class high brightness InGaN / AlGaN double heterostructure blue light emitting diodes," *Applied Physics Letters*, vol. 64, pp. 1687–1689, 1996.

[76] "Cree UT170, 50-um, Gen 3 LED Chips. http://www.cree.com/led-chips/products/ut-leds/ut170."

[77] L. Drori, "AFFOA Opens $10 Million HQ and Unveils Two Advanced Fabric Product Platforms. http://go.affoa.org/affoa-opens-10-million-hq/#section01," 2017.

[78] K. Toussaint, "AFFOA opens Cambridge headquarters by unveiling hat that transmits audio. http://www.metro.us/news/local-news/boston/affoa-cambridge-headquarters-hat-transmits-audio," 2017.

[79] P. Brown, "New Facility Opens for the Development of Smart Fabrics and e-Textiles. http://electronics360.globalspec.com/article/9010/new-facility-opens-for-the-development-of-smart-fabrics-and-e-textiles," 2017.

[80] T. Hinchcliffe, "National Fabric Innovation Centre opens. https://www.tevonews.com/functional-apparel-news/950-national-fabric-innovation-centre-opens," 2017.

[81] Z. Enwemeka, "National Fabric Innovation Center Opens In Cambridge With A Hat That Streams Audio. http://www.wbur.org/bostonomix/2017/06/19/cambridge-fabric-innovation-center-opens," 2017.

[82] D. L. Chandler, "AFFOA launches state-of-the-art facility for prototyping advanced fabrics. http://news.mit.edu/2017/affoa-launches-state-art-facility-protoyping-advanced-fabrics-0619," 2017.

[83] H. Bray, "MIT lab shows off smart threads that can send messages, change color. https://www.bostonglobe.com/business/2017/06/19/mit-lab-shows-off-smart-threads-that-can-send-messages-change-color/Kf8S15GtAWuZEc7TXprVkM/story.html," 2017.

[84] E.-H. Banaei and A. F. Abouraddy, "Design of a polymer optical fiber luminescent solar concentrator," *Progress in Photovoltaics: Research and Applications*, vol. 23, pp. 403–416, 2015.

[85] E. Hecht, *Optics*. Essex, UK: Pearson Education Limited, 2014.

[86] R. Deans, A. Rose, K. M. Bardon, L. F. Hancock, and T. M. Swager, "Detection of explosives and other species," 2010.

[87] A. Gumennik, E. C. Levy, B. Grena, C. Hou, M. Rein, A. F. Abouraddy, J. D. Joannopoulos, and Y. Fink, "Confined in-fiber solidification and structural control of silicon and silicon - germanium microparticles," *Proceedings of the National Academy of Sciences*, vol. 114, no. 28, pp. 7240–7245, 2017.

[88] B. M. Quandt, F. Braun, D. Ferrario, R. Rossi, A. Scheel-Sailer, M. Wolf, G.-L. Bona, R. Hufenus, L. J. Scherer, and L. F. Boesel, "Body-monitoring with photonic textiles: a reflective heartbeat sensor based on polymer optical fibres," *Journal of the Royal Society Interface*, vol. 14, no. 20170060, pp. 1–10, 2017.

[89] J. Allen, "Photoplethysmography and its application in clinical physiological measurement," *Physiological Measurement*, vol. 28, pp. R1–R39, 2007.

[90] H. Clevenson, M. E. Trusheim, C. Teale, T. Schröder, D. Braje, and D. Englund, "Broadband magnetometry and temperature sensing with a light-trapping diamond waveguide," *Nature Physics*, vol. 11, pp. 393–398, 2015.

[91] B. Saleh and M. Teich, *Fundamentals of Photonics.* Hoboken, NJ: Wiley Interscience, 2007.

[92] J. M. Marshall and A. E. Owen, "Drift mobility studies in vitreous arsenic triselenide," *Philosophical Magazine*, vol. 24, no. 192, pp. 1281–1305, 1971.

[93] Z. Borisova, *Glassy Semiconductors.* New York, NY: Plenum Press, 1981.